uOttawa

L'Université canadienne
Canada's university

FACULTÉ DES ÉTUDES SUPÉRIEURES ET POSTOCTORALES

uOttawa

L'Université canadienne
Canada's university

FACULTY OF GRADUATE AND POSDOCTORAL STUDIES

Simon Frédérick

AUTEUR DE LA THÈSE / AUTHOR OF THESIS

Ph.D. (Physics)

GRADE / DEGREE

Department of Physics

FACULTÉ, ÉCOLE, DÉPARTEMENT / FACULTY, SCHOOL, DEPARTMENT

Microcavity Designs for an InAs/InP Quantum Dot Fibre-Compatible Single Photon Source

TITRE DE LA THÈSE / TITLE OF THESIS

Robert Williams

DIRECTEUR (DIRECTRICE) DE LA THÈSE / THESIS SUPERVISOR

CO-DIRECTEUR (CO-DIRECTRICE) DE LA THÈSE / THESIS CO-SUPERVISOR

EXAMINATEURS (EXAMINATRICES) DE LA THÈSE / THESIS EXAMINERS

John Armitage

Peter Herman

Javier Giorgi

Lora Ramunno

Gary W. Slater

Le Doyen de la Faculté des études supérieures et postdoctorales / Dean of the Faculty of Graduate and Postdoctoral Studies

Microcavity Designs for an InAs/InP Quantum Dot Fibre-Compatible Single Photon Source

Simon Frédérick

Thesis Submitted to the
Faculty of Graduate and Postdoctoral Studies
In partial fulfillment of requirements
For the Doctor of Philosophy degree in Physics

Department of Physics
Faculty of Sciences
University of Ottawa

Your file Votre référence
ISBN: 978-0-494-50730-8
Our file Notre référence
ISBN: 978-0-494-50730-8

À mes parents et mon frère.

"To believe is very dull. To doubt is intensely engrossing. To be on the alert is to live, to be lulled into security is to die."

– Oscar Wild

Table of Contents

List of Tables

List of Figures

Abstract

A source of on-demand single photons for fibre-based quantum information processing applications is highly desirable. To generate single photons at 1.55 μm we use an InAs/InP single quantum dot. Initial measurements to demonstrate the anti-bunched emission from the quantum dot are presented. In order to enhance the emission properties of the quantum dot, it is embedded in a microcavity. A broad variety of micropillar and photonic crystal microcavities are explored in order to find an optimized design to enhance the emission through the Purcell factor. Also, the microcavity output mode has to be suitable to funnel the emitted photons to a communication channel. The microcavity design properties are evaluated by measuring the escaping photons from the embedded high density layer of quantum dots or through complete three-dimensional finite-difference time-domain simulations. A "champion" design using a photonic crystal microcavity is shown to fulfill all the requirements. Record breaking microcavity quality factor (28 000) for an InP-based microcavity is demonstrated. A digital etching technique to tune the photonic crystal microcavity after fabrication is demonstrated. Repetitive removal of an oxide layer formed on the InP with wet chemistry enlarges the photonic crystal holes and reduces the InP layer thickness. Silica nanowire evanescent field coupling is used to probe the mode structure of a microcavity, allowing the extraction of single photons and tuning of the microcavity mode wavelength.

Statement of Originality

The experimental results presented in this thesis build on the pioneering work done at the Institute for Microstructural Sciences (IMS) within the National Research Council of Canada to produce excellent InAs/InP quantum dots emitting at 1.55μm as well as their ability to generate InAs/InP single quantum dots at a pre-determined positions (*i.e.* a site-selected dot). The main goal of this thesis is the construction of a source of 1.55μm single photons using such single site-selected InAs/InP quantum dot embedded within a microcavity. Numerous novel experimental observations are presented here since, to the best of our knowledge, they were first published by us in peer-reviewed scientific journals or published only within this thesis.

The thesis project is an ambitious one and is the result of a collaboration within many researcher at the IMS and the University of Ottawa. The University of Sydney and University of British Columbia collaboration were also important. In order to distinguish my contributions from the work of the group and our collaborators I will review the major achievements accomplished within the scope of our work. The superscript numbers refer to papers within the publication list presented in the following section.

I performed the first anti-bunching measurement on site-selected InAs/InP quantum dots and while the results generated are not conclusive enough to prove without a doubt the anti-bunched nature of the dot single exciton emission line, I believe the results are still interesting in that they hint towards an answer.

The first type of microcavity explored was the micropillar. The results obtained were the first to show the coupling between a micropillar based on dielectric mirrors and InAs/InP quantum dots. I came in late in the project as I was starting my

doctorate. I contributed in the characterization of the micropillars emission spectrum. I contributed to the creation and characterization of our highest Purcell factor micropillar[1] and also performed low temperature measurements on the micropillar systems to test the influence of temperature on the distributed Bragg reflector.

The major part of my work was to construct a photonic crystal microcavity with ideal properties to complement the quantum dot emission and create an efficient single photon source. Photonic crystal microcavities require a more extensive study because there is no exact recipe, no analytical solution to generate the desired microcavity properties. While there has been numerous publications on the subject of photonic crystal microcavities, their designs had to be adapted to our material system and we were the first one to explore InAs/InP quantum dots in an InP photonic crystal microcavity[1,2,4–7]. The Purcell factor reached by our microcavity now even surpasses that of the competition. I was involved in the microcavity design with the finite-difference time-domain simulations through discussions with Dr. Williams and Dr. Aers who were in charge of inputting the simulation runs on the computer cluster.

The photonic crystal microcavity fabrication can be separated in two steps. First is the inscription, with an electron beam, of the photonic crystal pattern. The computer file used by the electron beam system was mainly edited by Dr. Dalacu. He, Dr. Williams and I discussed the various modifications to the microcavity design to be inserted in each sample run. I also contributed to the second fabrication step, the chemical procedure to create the microcavity from the pattern.

Each created sample was tested through measurement of the photoluminescence of an embedded ensemble of quantum dots in order to examine its mode structure. I was heavily involved in the sample characterization both at room temperature and at 4K. I also performed polarization dependent measurements to further investigate the mode structure.

I heavily contributed to a novel post-fabrication tuning technique using the repetitive removal of a native oxide layer[3]. We were the first to apply it to the InP material. I performed most of the experiments required to demonstrate the technique.

We constructed the first microcavity coupled to embedded site-selected quantum

dots. I contributed to the design of a mask with appropriate alignment marks for the electron beam machine to be able to overlap the microcavity and the quantum dot. Photoluminescence measurements show a successful overlap between the quantum dots and the microcavity mode positions.

Initial experiments with silica-nanowire evanescent field coupling measurements were done in Sydney by our collaborators using a sample I pre-characterized before to sending it to them[8]. After they demonstrated their setup could work with InP sample, Dr. Williams and I went there to measure higher Q-factor microcavity and push the technique further (only published in this thesis). It was the first demonstration that the nanowire proximity to an InP-based photonic crystal microcavity can serve as a mean to: 1- probe the microcavity mode structure, 2- tune the microcavity emission energy and 3- extract the photons and direct them to a communication channel.

The second harmonic generation and resonant scattering experimental results were obtained using the experimental setup at the University of British Columbia[10–12]. Those results were obtained with samples we fabricated and I was not directly involved those measurements I was involved in the sample design and the sample pre-characterization.

Publications

The following articles were published during the course of this work.

Directly Related to Thesis

1. S. Frédérick, D. Dalacu, D. Poitras, G.C Aers, P.J. Poole, J. Lefbvre, D. Chitriani, and R.L. Williams. Near-infrared Single Photon Sources Employing Site-Selected InAs/InP Quantum Dots Microcavities. *Microelect. Jour.*, 36:197, 2005.

2. D. Dalacu, S. Frédérick, A. Bodganov, P.J. Poole, G.C. Aers, R.L. Williams, M.W. McCutcheon, and J.F. Young. Fabrication and Optical Characterization of Hexagonal Photonic Crystal Microcavities in InAs/InP Quantum Dot Membranes. *J. Applied Phys.*, 98:023101, 2005.

3. D. Dalacu, S. Frédérick, P.J. Poole, G.C. Aers, and R.L. Williams. Post-Fabrication Fine-Tuning of Photonic Crystal Microcavities in InAs/InP Quantum Dot Membranes. *Appl. Phys. Lett.*, 87:151107, 2005.

4. D. Dalacu, S. Frédérick, J. Lapointe, P.J. Poole, G.C. Aers, and R.L. Williams. Modified Single Missing Air-Hole Defects in InAs/InP Quantum Dot Membrane Photonic Crystal Microcavities. *J. Vac. Scie. and Technol. A*, 24(3):791, 2006.

5. S. Frédérick, D. Dalacu, G.C. Aers, P.J. Poole, J. Lapointe, and R.L. Williams. Optical Characterisation of InAs/InP Quantum Dot Photonic Cavity Membranes. *Physica E*, 32:504, 2006.

6. S. Frédérick, D. Dalacu, P.J. Poole, J. Lapointe, G.C. Aers, and R.L. Williams. InAs/InP Quantum Dot Photonic Crystal Microcavities. *Phys. Stat. Solidi c*, 3:3685, 2006.

7. S. Frédérick, D. Dalacu, J. Lapointe, P.J. Poole, G.C. Aers, and R.L. Williams. Experimental Demonstration of High Quality Factor, x -Dipole Modes in InAs/InP Quantum Dot Photonic Crystal Microcavity Membranes. *Appl. Phys. Lett.*, 89:091115, 2006.

8. C. Grillet, C. Smith, D. Moss, B. Eggleton, S. Frédérick, D. Dalacu, P.J. Poole, J. Lapointe, G.C. Aers, and R.L. Williams. Coupling via Tapered Nanowire Micro-Loops to Photonic Crystal Nanocavities for Single-Photon Source Applications. *Opt. Express*, 15:1267, 2007.

9. S. Frédérick, D. Dalacu, D. Kim, P.J. Poole, G.C. Aers, and R.L. Williams. Single Photon Sources for Quantum Cryptography and Quantum Computing. *Physics in Canada*, 63:207, 2007

Contributions not Directly Related to Thesis

10. M.W. McCutcheon, G.W. Rieger, I.W. Cheung, J.F. Young, D. Dalacu, S. Frédérick, A. Bodganov, P.J. Poole, G.C. Aers, and R.L. Williams. Resonant Scattering and Second Harmonic Generation Spectroscopy of a Photonic Crystal Microcavity. *Appl. Phys. Lett.*, 87:221110, 2005.

11. M.W. McCutcheon, J.F. Young, G.W. Rieger, D. Dalacu, S. Frédérick, P.J. Poole, G.C. Aers, and R.L. Williams. Second-Order Nonlinear Mixing of Two modes in a Planar Photonic Crystal Microcavity. In A. Abidi, Shown-Yu Lin, and A. Sherer, editors, *Photonic Crystal Materials and Devices IV*, volume 6128 of Proc. of SPIE, page 612812, 2006.

12. M.W. McCutcheon, J.F. Young, G.W. Rieger, D. Dalacu, S. Frédérick, P.J. Poole, and R.L. Williams. Experimental demonstration of second-order processes in photonic crystal microcavities at submilliwatt excitation powers, *Phys. Rev. B*, 76:245104(2007)

Acknowledgements

I would like to extend my most profound gratitude to Prof. Robin Williams who has guided me through my doctoral work like a maestro. You took a chance by accepting me as a graduate student, coming from Québec city with minimal knowledge of the language of Shakespeare, and no scholarship and you have my greatest appreciation. You were always available, your office door always open, be it for scientific discussion or talks about the experiments. Thank you.

Working at the National Research Council as literally been a blessing. The scientific knowledge of the staff is incredible and the world leading equipment is the icing on the cake. Dr. Dan Dalacu has been a source of inspiration. Your undeviating happiness made work fun and given your extraordinary capacity to generate samples the laughs were welcomed. Je veux aussi remercier Dr. Jacques Lefebvre pour ces nombreux conseils et son assitance dans le laboratoire. Dr. Geoff Aers advices and input proved essential and Dr. Philip Poole extensive knowledge of epitaxial processes was indispensable to the success of this work. The assistance and friendship of Joe McKee and William Render was invaluable.

I also have to thank Prof. David Moss, Dr. Christian Grillet and Camerson Smith, our collaborators at the University of Sydney, for precious measurement using their experimental setup as well as Jeff F. Young and Murray McCutcheon at the University of British Columbia.

I consider myself very lucky to have shared lab time with fellow students Michael Reimer and Danny Kim. Our exchanges were quite stimulating and I value their scientific input as well as their help with experimental challenges. My thanks to both of you dudes, I consider you more than colleagues and count you as my friends. I

sincerely hope we can stay in touch long after this. I also have to thank the "lunch-bunch" without whom I would have had to eat lunch quickly while working in front of the computer. The long lunch break not only eased my digestion but enable me to make friends.

Merci à Frédérique pour tout ce qu'elle a fait pour moi. Merci d'être toi-meême en tout temps. Ton honnêteté et ton support ont fait de moi un homme différent et meilleur. Sans toi je ne sais pas si j'aurais vu la fin de ce long parcours. Finalement, mais pas le moindre, j'aimerais remercier mes parents, Carole et Michel, et mon frère, Vincent, pour leur support inconditionnel à travers ce long trajet qu'est une thèse de doctorat. Bien qu'ils étaient physiquement loin de moi, chacun de mes retours à la maison m'a permis de recharger mes batteries et de retrouver la motivation. Votre soutien m'est indispensable et je vous aime.

Legend

List of Acronyms

1D one dimension

2D two dimensions

3D three dimensions

AFM atomic force microscopy

APD avalanche photodiode

BB84 Bennett-Brassard protocol invented in 1984

BBO β-BaB_2O_4

BOE buffered oxide etch

CBE chemical beam epitaxy

CCD charge coupled device

CL cathodoluminescence

CQED cavity quantum electro-dynamics

DBR distributed Bragg reflector

DOS density of state

E6 mixture of phosphoric, acetic and nitric acids

EL electro-luminescence

EH one of the two solution a circular waveguide (orthogonal to the HE modes)

FDTD finite-difference time-domain

FFT fast-Fourier transform

FP Fabry-Pérot

FWHM full width at half maximum

FTIR Fourier transform infrared spectrometre

GFT Green function tensor

HE one of the two solution a circular waveguide (orthogonal to the EH modes)

ICP inductively coupled plasma

IMS Institute for Microstructural Sciences

IR infrared

KD*P deuterated potassium dihydrogen phosphate

KTP $KTiOPO_4$

LOQC linear optics quantum computing

MBE molecular beam epitaxy

MIT Massachusetts Institute for Technologies

ML monolayer

μPL micro-photoluminescence

MOCVD metal organic chemical vapor deposition

MOVPE metal organic vapor phase epitaxy

NIR near infrared

NMP N-Methylpyrolidone

NSOM near-field scanning optical microscopy

N-V nitrogen-vacancy

OPO optical parametric oscillator

PhC photonic crystal

PL photoluminescence

PLE photoluminescence excitation

PolPL polarization dependant photoluminescence

PPLN periodically-poled lithium niobate

QCpu quantum computing

QD quantum dot

QKD quantum key distribution

QW quantum well

RS resonant scattering

SAQD self-assembled quantum dot

SE spontaneous emission

SEM scanning electron micrograph

SHG second harmonic generation

SP single photon

SPAD single-photon avalanche photodiode

SPDC spontaneous parametric down conversion

SRL stress relieving layer

SQD single quantum dot

TE transverse electric field

TEGa triethylgallium

TM transverse magnetic field

TMI trimethyl-indium

TCSPC time-correlated single photon counting

UV ultraviolet

VCSEL vertical-cavity surface-emitting laser

ZEP positive tone electron beam resist from Nippon Zeon

List of Symbols

c : Speed of light $= 2.998\times10^{8}\,\mathrm{m/s}$

h : Planck constant $= 6.626\times10^{-34}\,\mathrm{Js}$

$\hbar$: Planck constant divided by 2π

ε_0 : Permittivity of the vacuum $\approx \frac{1}{36\pi} \times 10^{-9}\,\mathrm{C^2/N.m^2}$

μ_0 : Permeability of the vacuum $\approx 4\pi \times 10^{(-7)}\,\mathrm{m.kg/C^2}$

e : Electron charge magnitude $= 1.602 \times 10^{-19}\,\mathrm{C}$

$G_{12}(\tau)$: Coincidence signal for a delay τ between the detectors

$g^{(2)}(\tau)$: Normalized second order correlation function

λ : Wavelength

ω : Frequency

k : Wavevector

$\vec{A}$: Magnetic potential

$\vec{E}$: Electric field intensity

$\vec{D}$: Electric field displacement

$\vec{H}$: Magnetic field intensity

$\vec{B}$: Magnetic flux density

$\varepsilon_r^*(\omega)$: Complex relative dielectric constant

$\chi^{(j)}$: j^{th} order susceptibility

n : Material refractive index

m : Particle mass

q : Particle charge

p : Particle momentum

α_R : Relaxation rate from higher-order excited state to $|e\rangle$

α_p : Relaxation rate of $|e\rangle$

$a_{\vec{k}s}^{\dagger}$: Creation operator of the quantum electric field in mode $(\vec{k}, s)$

$a_{\vec{k}s}$: Annihilation operator of the quantum electric field in mode $(\vec{k}, s)$

s : Polarization index of the quantum electric field

$\vec{d}_{qd}$: Quantum dot dipole moment

ω_a : Frequency of quantum dot excitonic level a

Γ_a : Linewidth of quantum dot excitonic level a

τ_a : Recombination lifetime of the quantum dot excitonic level a

$\gamma_{a\to j}^{(0)}$: Emission rate in vacuum

$\gamma_{a\to j}^{(cav)}$: Emission rate for the transition of energy level a to level j of the quantum dot in the cavity

$\gamma^{(\mu)}$: Emission rate of the quantum dot in the cavity mode μ

λ_μ : Wavelength of the cavity mode μ

ω_μ : Frequency of the cavity mode μ

Γ_μ : Linewidth of the cavity mode μ

$\delta_{\Gamma_\mu}(\omega - \omega_\mu)$: Normalized Lorentz function centered around ω_μ with width Γ_μ

$\vec{E}_\mu(\vec{r})$: Electric field of the mode μ at the position $\vec{r}$

$\vec{\alpha}_\mu(\vec{r})$: Normalized spatial function of mode μ

Ω_μ : Interaction frequency between an atom and a cavity mode.

F_p : Purcell factor

Q_μ: Mode μ Cavity quality factor

V_μ: Mode μ Effective mode volume

$\Phi_T(\lambda_0)$: Total phase delay for a one-half cavity cycle

$\phi_r(\lambda_0)$: Phase delay associated with a PhC mirror reflection.

$n_{eff}(\lambda_0)$: Cavity mode effective refractive index

$|r(\lambda_0)|^2$: Mode reflectivity at the PhC mirror

$v_g(\lambda_0)$: Mode group velocity at λ_0

H : Hamiltonian

r_p : Micropillar radii

ϵ : Extraction efficiency

η : Collection efficiency

β_{SE} : Spontaneous emission coupling factor

Microcavity Type Acronyms

H1: Single missing hole defect[1]

H1S: Symmetrically modified single missing hole defect

H1E: Elongated single missing hole defect

H1Y: Modified single missing hole defect to optimize the y-dipole mode

H1X: Modified single missing hole defect to optimize the x-dipole mode

H3: Triple missing hole defect

PhC microcavity parameters

d : Membrane thickness

a : Pitch between lattice holes

r : Host lattice hole radii

r_i : Inner ring hole radii. See Fig.8.9

δ_i : Inner ring hole shift. See Fig.8.9

δ_x : Two hole shift along x-axis. See Fig.8.14

δ_{3x} : Two hole shift along x-axis for a triple missing cavity. See Fig.8.19.

r_4 : Four corner holes radii. See Fig.8.26 and Fig.8.27

δ_4 : Four corner hole shift. See Fig.8.26 and Fig.8.27

δ_2 : Two additional hole shift. See Fig.8.27

[1]Detailed description of the different PhC microcavities design, including figures, can be found in chapter 8.

Chapter 1

Introduction

The work presented in this thesis is targeted at the development of a manufacturable source of single photons, based on the deterministic coupling of a single semiconductor quantum dot to the single electromagnetic mode of a high quality optical microcavity. We build on the world leading expertise at the National Research Council of Canada to produce site-selected InAs/InP QDs fit to produce a single photon source at 1.55 μm. I constructed an experimental setup to demonstrate the anti-bunched nature of the QD emission. The bulk of the work I did was dedicated to the fabrication of an optimal microcavity to couple to a selected single QD; optimizing the mode spatial profile, peak energy, far-field radiation pattern, quality factor, and effective volume, while developing a technique to tune the microcavity mode peak energy post-fabrication. I also explored the use of a silica nanowire evanescent field to couple to the microcavity to measure the microcavity mode structure, tune the microcavity, and potentially extract the photons.

Subsequent chapters will describe the choice of quantum dot for our particular application and will discuss in detail the design, fabrication and testing of particular

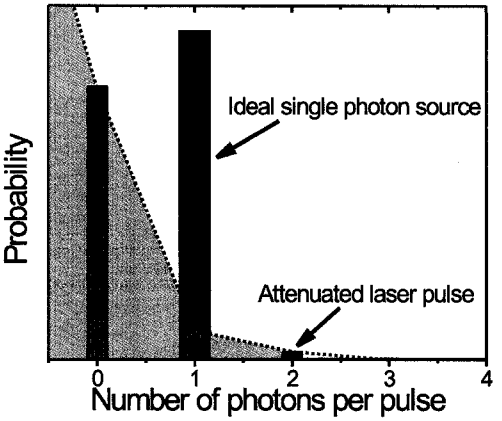

Figure 1.1: Comparison between an ideal single photon source (red bar) and a typical Poisson distribution of an attenuated laser pulse (green bars). The green shading highlights the discrete Poisson distribution.

types of optical cavity. In this chapter, I will motivate my work by describing some of the potential uses for single photon sources and the competing technologies that are being studied for single photon generation.

1.1 Electromagnetic Field Quantization

The quantization of light results in a description of the electric field as a quantum mechanical operator. Each mode of the field can be described as a quantized simple harmonic oscillator with its respective creation and annihilation operators, $a^{\dagger}_{\vec{k}s}$ and $a_{\vec{k}s}$, that describe how a single quanta, or photon, is created in or removed from the electromagnetic mode described by wavevector $\vec{k}$ and polarization index s within an

enclosure of volume V. The field operator can be written as [1,2]:

$$\vec{E}(\vec{r},t) = \vec{E}^{(+)}(\vec{r},t) + \vec{E}^{(-)}(\vec{r},t), \tag{1.1}$$

$$\vec{E}^{(+)}(\vec{r},t) = \sum_{\vec{k}s} \vec{E}^{(0)}_{\vec{k}} a_{\vec{k}s} \zeta_{\vec{k}s} \exp\{i(\vec{k}\cdot\vec{r} - \omega_{\vec{k}}t)\}, \tag{1.2}$$

$$\vec{E}^{(-)}(\vec{r},t) = \sum_{\vec{k}s} \vec{E}^{(0)}_{\vec{k}} a^{\dagger}_{\vec{k}s} \zeta_{\vec{k}s} \exp\{-i(\vec{k}\cdot\vec{r} - \omega_{\vec{k}}t)\}, \tag{1.3}$$

where $\{\zeta_{\vec{k}1}, \zeta_{\vec{k}2}\}$ describes two orthogonal polarization states and $\omega_{\vec{k}}$ is the frequency of the electromagnetic field with wavevector $\vec{k}$. The possibility of a Fock or number state arises within this formalism, *e.g.*:

$$|j\rangle_{\vec{k}s} = \frac{\left(a^{\dagger}_{\vec{k}s}\right)^j}{\sqrt{j!}} |0\rangle_{\vec{k}s}, \tag{1.4}$$

which corresponds to j quanta generated in the mode ($\vec{k}$, s) by repeated application of the appropriate creation operator to the vacuum state $|0\rangle$. No photons are present in $|0\rangle$, making it the most trivial example of a number state.

Because of the difficulties involved in producing an "on-demand" source of single photons (SPs), *i.e.* a source where a trigger is used to produce one and only one photon in a selected mode, many researchers requiring such a source have resorted to the approximation of an attenuated laser. Such sources have a Poisson distribution of photon number as illustrated in Fig.1.1, and clearly cannot guarantee a single photon in any particular mode. However, when the laser is operated at sufficiently low power, typically 0.1 photons per pulse or less for a pulsed source, there are many more pulses with one photon than with two. The vast majority of pulses are empty in this case, however and although this can typically be viewed as an "annoyance", it does severely limit the rate at which single photons can be sent.

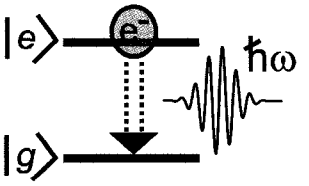

Figure 1.2: Two energy levels system. The electron relaxes to the ground state results in a single photon emission.

A simple two level atom can be viewed as the archetypal system for producing SPs (Fig.1.2), where relaxation from the excited state $|e\rangle$ to the ground state $|g\rangle$ results in the emission of a photon. Once excited, the system cannot be re-excited until relaxation to the ground state has occurred, so that multiple photon emission is precluded. Successive excitation of the system generates a SP stream with a repetition rate defined by the excitation and relaxation rate. In practice, real single photon sources can only approximate the ideal two level system and inadequacies arise that are related to higher lying energy states, finite level width, problems associated with loading $|e\rangle$ and interactions with the environment. Often, the system is excited to a higher energy state than $|e\rangle$ but only the photon resulting from the $|e\rangle$ to $|g\rangle$ transition is used. The indistinguishability, *i.e.* the degree to which successive optical pulses from the source will bunch together, of such an incoherently excited system is given by [3]:

$$I = \frac{\Gamma_{eg}}{\Gamma_{eg} + \alpha_p} \frac{\alpha_R}{2\Gamma_{eg} + \alpha_R}, \tag{1.5}$$

where Γ_{eg} is the spontaneous emission rate between $|e\rangle$ and $|g\rangle$, α_p is the dephasing rate of $|e\rangle$ and α_R is the relaxation rate from the higher-order excited state to $|e\rangle$. Both α parameters lead to a jitter in the arrival time of the SP wavepacket. Eq. 1.5 assumes that the emission linewidth is a delta function.

1.2 Quantum Information Processing

Quantum information processing can be thought of as a generic term describing protocols that seek to use fundamentally quantum principles (*i.e.* superposition, entanglement, etc.) when transmitting or processing information. The basic element in a quantum information system is referred to as a quantum bit (qubit) in analogy to the classical, two state bit found in existing computing systems. Although a qubit can be thought of as a two level system, in a similar manner to the classical "0" and "1" states of the classical bit, the qubit has one very important difference: it can exist in a superposition state between the "0" and "1", existing in both states simultaneously. The general state of a qubit, $|q\rangle$, is then: $|q\rangle = \alpha|0\rangle + \beta|1\rangle$, where α and β are generally complex coefficients such that $|\alpha|^2 + |\beta|^2 = 1$. The first section below introduces quantum key distribution, a means to transmit information in a demonstrably secure way and the second section describes some basic concepts of quantum computing (QCpu) that are relevant to our experimental system.

1.2.1 Quantum Key Distribution

Classical One-time Pad

The only completely secure way to transmit information is to use the one-time pad technique, in which an encryption key as long as the message itself is used for encoding. The encryption key is used to scramble a single message, after which it is discarded. In normal usage, a spy leaves on his mission taking the key with him, whilst his headquarters retains a copy. When headquarters wants to send a secret message

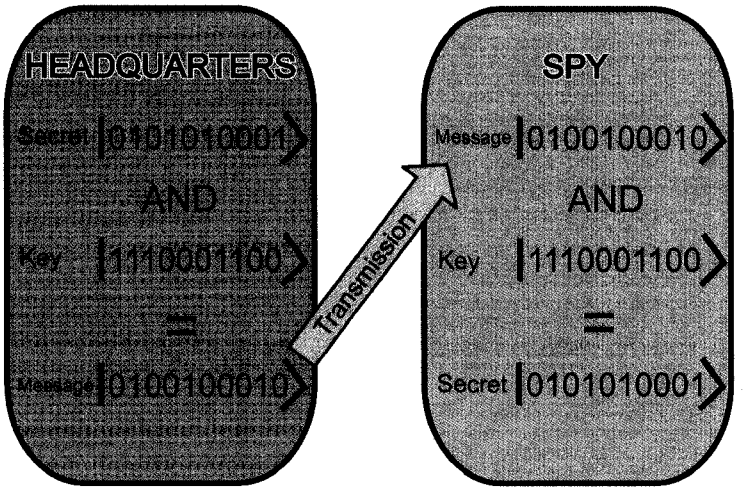

Figure 1.3: Illustration of the one-time pad cryptography technique

to the spy, they can use the AND function between the message and the key (see Fig.1.3) to produce the encrypted text. To read the message the spy performs the AND function again using his copy of the encryption key. Provided the key has not been compromised the communication is 100% secret. Note that the spy decides what length of key he takes prior to leaving. Should a message be longer than the key he took then the transmission will fail to be 100% secure. A demonstrably secure way to transmit the encryption key using a real time communication channel would provide a much better solution.

Quantum One-Time Pad

The distribution of cryptographic keys, *i.e.* the one-time pads discussed above, using provably secure optical means is arguably the prime motivational drive for the development of SP sources today. A detailed review of this field can be found in refs. [4,5]. The conceptual beginnings of optical quantum key distribution (QKD) can be found in the 1984 paper by Charles Bennet and Gilles Brassard, where a scheme for quantum

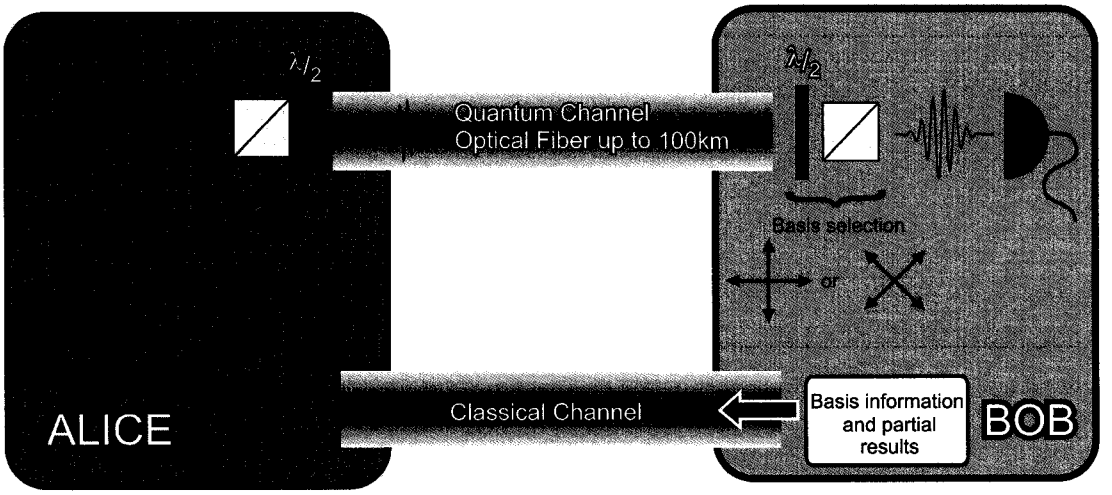

Figure 1.4: Schematical representation of the QKD protocol BB84.

key distribution that has come to be known as the "BB84 protocol" was proposed [6]. This scheme uses two orthogonal polarization states of a single photon as the qubit and relies on two fundamental tenets of quantum mechanics for its security:

1. It is not possible to clone an individual quantum state,

2. Unless in an eigenstate of the measurement operator, a measurement will inherently introduce a modification to the state that can be detected.

Fig.1.4 shows a cartoon representation of the BB84 protocol. Traditionally the sender is called Alice and the receiver Bob. Communication between the two proceeds along two different channels: a classical one and a quantum one where the key will be sent. In practice, these two channels can be implemented within the same optical fiber. Alice sends the key to Bob as a stream of single photons (qubits) with the "0s" and "1s" encoded in two different choices of basis states, namely $\{|\updownarrow\rangle, |\leftrightarrow\rangle\}$ and $\{|+45^o\rangle, |-45^o\rangle\}$. The basis is randomly changed at the sending and receiving end without correlation. After the key has been sent, Bob reveals to Alice, over the

classical channel, the sequence of basis choices he made for receiving the photons. The encryption key is the sequence of qubits that were received when Bob's basis choice matched that of Alice. It is important to note that neither Alice nor Bob individually decides the key, but both of them do through the randomness of the bases. Statistically, from the original photon string, only $\sim 50\%$ will be left after Bob makes his basis choices.

If an eavesdropper (Eve) intercepts the SPs and measures them, Bob does not receive anything and while comparing bases with Alice discards those missing bits. In the case where Eve sends replacing qubits, the randomness of the basis makes it such that at best Eve's "duplicate" is the same as Alice 50% of the time. Hence, the qubit overlap between Alice and Bob goes down to 25%. By comparing their respective results for a significant portion of the key on the classical channel, Alice and Bob can check for eavesdropping; discarding the section of the key they use to check the channel security. Of course, even in the absence of eavesdropping, the quantity of "good" qubits will never be 50% and a small shortfall is tolerable. The question of how low is too low is a complex one and is strongly correlated with the noise level of the system (how many SP are lost, detector efficiency, ...) and the classical and/or quantum error correction algorithms used. If the overlap is good enough the unshared part of the key is used to encode the secret. The encrypted data is sent, in the "open", by the classical channel. The BB84 protocol is constantly used and improved and more recent versions as well as error correction algorithms can be found in refs. [5, 7–10] and references therein.

An important point to notice is that the channel security is tested by transmitting the key and not the actual message itself. If the channel is found to be unsafe, no information has been compromised. This is equivalent to sending the encryption key in a safe briefcase and if the briefcase does not make it then only the key has been lost. If Alice sends two photons in the same polarization state simultaneously, instead of one, the whole scheme is ruined. Eve can now measure one of the photons whilst leaving the second one unperturbed. Alice and Bob are not able to detect her influence on the data and the process is no longer secure.

In order to avoid two-photon generation with an attenuated laser pulse, the pulse intensity is reduced to contain a SP less than 5% of the time. This results in a two-photon probability well below 0.5%; an acceptable value considering the aforementioned error correcting algorithms [5, 7–10]. The low SP emission rate puts considerable stress on the transmission protocol however, making it quite difficult to detect an eventual eavesdropper. Nevertheless, commercial systems based on attenuated laser pulses and error correction algorithms are available from MagiQ [11], id Quantique [12], and SmartQuantum [13]. The resulting bit rates are quite slow however and the communication distances are limited.

1.2.2 Quantum Computing

The idea to use the laws of quantum mechanics advantageously to do computation was developed in the early 80's by Feynman, Deutsch and others (see Refs. [14, 15] and references therein). In a quantum computer the state of the bits can be described

by a wavefunction such as [16]:

$$|\Phi\rangle = \alpha|0110011...\rangle + \beta|0101101...\rangle + ..., \tag{1.6}$$

where α, β, etc. are complex numbers and $|0110011...\rangle$ are possible states of the system. Each 1 and 0 refers to the state of the qubit. The system is hence in a superposition of states and the phases associated with the complex numbers contain relevant information. The different logic associated with such a system leads to the development of new algorithms like Shor's polynomial factorization algorithm [17], or Grover's search algorithm [18].

The system studied in this thesis -a single QD coupled with a microcavity- can be used to perform quantum computing (QCpu) using two different approaches. First, it can be used as a highly efficient SP source within a linear optics quantum computing (LOQC) scheme. Second, it can be used as a way to steer and/or store a "flying qubit" within a QD electron spin state and then to re-emit a photon at some later time. There exists a large variety of potential QCpu schemes and devices, some of which are discussed below. The merits and advantages of one scheme over the other will not be discussed in detail here since QCpu *per se* is not the main goal of the work presented in this thesis.

Linear Optics Quantum Computing

As the name linear optics quantum computing (LOQC) suggests, it involves QCpu using SPs, photodetectors and linear optical elements (beam splitters, phase shifters, mirrors etc.). The proposal to use simple optics and photons to perform quantum

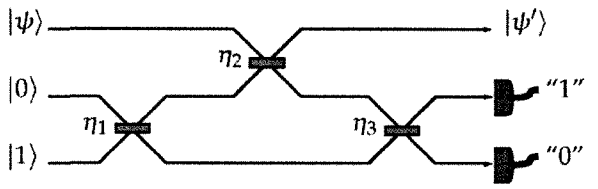

Figure 1.5: Nonlinear sign gate. From [22]

logic operation was first made by Milburn [19]. The field truly blossomed with a publication in 2001 by Knill, Laflamme and Milburn [20]. The advantage of SPs with respect to other quantum objects involves their low coupling to the environment and thus the circumvention of many decoherence effects.

Computation with SPs and linear optical elements takes full advantage of the bosonic nature of the electromagnetic field. Consider a simple 50/50 beam splitter with the two input arms labeled a and b and the two exit arms c and d. If one photon enters each of the two arms $|1,1\rangle_{a,b} = a^\dagger b^\dagger |0,0\rangle_{a,b}$, the output is $1/2(c^\dagger + d^\dagger)(c^\dagger - d^\dagger)|0,0\rangle_{c,d}$ which is equal to $1/\sqrt{2}(|2,0\rangle_{c,d} - |0,2\rangle_{c,d})$. The photons bunch together [21].

As an example of LOQC, one of the necessary gates is the nonlinear sign gate which acts on the three lowest Fock states in the following way:

$$\alpha|0\rangle + \beta|1\rangle + \gamma|2\rangle \Rightarrow \alpha|0\rangle + \beta|1\rangle - \gamma|2\rangle, \tag{1.7}$$

and its action on the higher states is irrelevant. The name "nonlinear sign gate" comes from the fact that in the original optical computing schemes, it was constructed using nonlinear material. Figure 1.5 comes from ref. [22] and shows such a nonlinear sign gate. Using only 3 beam splitters (with transmission amplitudes $\eta_1 = \eta_3 = \frac{1}{4-2\sqrt{2}}$ and $\eta_2 = 3 - 2\sqrt{2}$) the required operation can be done probabilistically using projective

measurements. The three ports, one for the function and two other ancillary modes crossing each other onto the beam splitters, perform the nonlinear sign gate operation. For a review of the technique consult [22]. For a detail theoretical description of a single quantum dot (SQD)-microcavity system used for LOQC see Ref. [23].

Considering the fact that the nonlinear sign gate is one of the simplest operations required by a quantum computer, and that it requires one on-demand SP in addition to those composing $|\psi\rangle$, it is clear that a real LOQC process will require a large number of efficient, on-demand sources of SPs.

Cavity Quantum Electro-Dynamics

The field of cavity quantum electro-dynamics (CQED) started with atoms in a cavity and while this approach is producing impressive experimental results [24, 25], it is hard to envision a QCpu based on multiple copies of such systems, given the high level of complexity involved. Nevertheless, the theory developed for these systems can be applied to a SQD-microcavity systems if the QD is at temperatures where its density of state (DOS) is atom-like. Chapter 5 will introduce the theory behind the QD-microcavity coupling and its effect on the QD emission properties.

The coupling between the QD and the microcavity modifies the QD recombination rate through the Purcell effect [26]. Moreover, the escaping photons are now in the specific microcavity optical mode that matches the QD transition energy. The result is a more efficient SP source that can be employed within a LOQC scheme.

Quantum Repeater

It was shown recently that placing electrostatic gates around a SQD allows one to isolate the spin of a single electron within the SQD [27]. Moreover, the electron spin is directly related to the polarization state of the incident photon generating an electron-hole pair (also known as a quasi-particle called exciton) in the QD. In these experiments, the hole is removed while keeping the electron thanks to a positive bias on the gates and a potential barrier region underneath the QD layer. The electron spin can be preserved for over 1 ms if a magnetic field is applied to prevent spin flips. The removal of the bias results in the re-insertion of holes and the emission of a photon with the same polarization as the excitation. This behavior is that of a quantum repeater. No matter the initial photon polarization the re-emitted photon will have this same polarization. As a photon propagates along it encounters losses and has a coherence length. Quantum repeaters are highly desirable because of those losses. The addition of a microcavity to the system would provide much higher collection and re-emission efficiency. Moreover, the quantum repeater is a building block towards QCpu [23, 25, 28–30]. The ability to impart the electron spin state to a "flying qubit" could also be used to transmit information between two separate computation sites.

1.3 Single Photon Sources in Practice

An ideal SP source would generate a SP at every request, keeping the two-photon and zero-photon probabilities zero. The resulting protocol would then be a lot more efficient with respect to using an attenuated laser source, and would enable transmission

over much greater distance and/or a greater sensitivity to eavesdropping. The effort put on error correction would be used to compensate the propagation losses instead of the Poisson distribution of the light source. In this section, I will review the various competing technologies aiming to the construction of a single photon source.

1.3.1 Nonlinear Effects in Material

The schemes presented in this section take advantage of nonlinear effects within certain materials to generate a pair of entangled photons. The electric field displacement in a material ($\vec{D}$) is given by the sum of $\varepsilon_0\vec{E}$ and the polarization vector $\vec{P}$. The later is given by:

$$\vec{P} = \varepsilon_0\chi\vec{E} = \varepsilon_0\left(\chi^{(1)}\cdot\vec{E} + \chi^{(2)} : \vec{E}\vec{E} + \chi^{(3)}\vdots\vec{E}\vec{E}\vec{E} + \cdots\right). \tag{1.8}$$

The material susceptibility χ is expanded in multiple tensorial order $\chi^{(j)}$, a tensor of the rank $j+1$. While the linear susceptibility ($\chi^{(1)}$) represents the dominant contribution to $\vec{P}$, some materials show significant effects due to the higher order susceptibilities. Spontaneous parametric down conversion (SPDC) originates from second order susceptibility effects and figure 1.6 introduces the basic concept and relevant energy diagram. A pump photon of frequency ω_{pump} excites the system to $|e\rangle$ and the $\chi^{(2)}$ effect results in the simultaneous emission of two photons with energy $\hbar\omega_{SPDC} = \frac{\hbar\omega_{pump}}{2}$. The probability of this two photon emission event is very low and proportional to the pump power. One could increase the pumping power to increase the efficiency but then other nonlinear effects start appearing. Due to energy conservation considerations, the two particles are emitted within two intersecting light

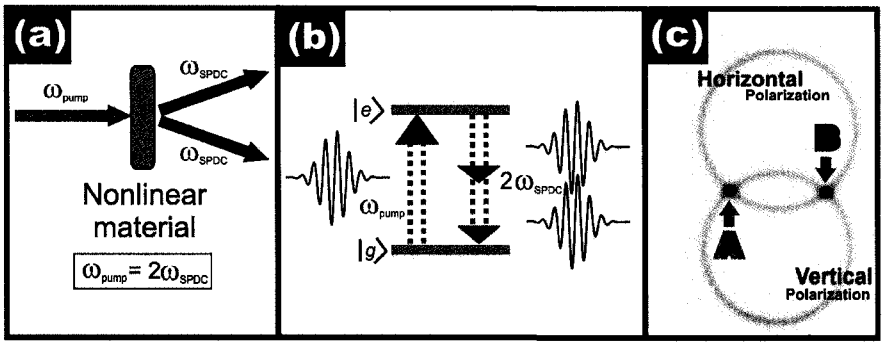

Figure 1.6: **(a)** Schematics of the SPDC process. **(b)** Energy diagram of the SPDC process. **(c)** The two light cones of the type *II* SPDC process, from [31]. By selecting photons where the two cones overlap one has a pair of entangled photons.

cones (Fig.1.6**(c)** borrowed from [31]).

By selecting only the photons from the intersection points (highlighted by arrows **A** and **B** in Fig.1.6), one overlaps the wavefunctions for the two photons and an entangled photon pair is produced. The total wavefunction can be expressed as: $|\phi_T\rangle = -1/\sqrt{2}(|\updownarrow,\leftrightarrow\rangle_{A,B} + |\leftrightarrow,\updownarrow\rangle_{A,B})$ while each path can be described as $|\phi_A\rangle = 1/\sqrt{2}\,(|\updownarrow\rangle + |\leftrightarrow\rangle)$ and the polarization state measurement of one resolves the other. If the spatial location is the only way to distinguish between the two photons, the two photons are polarization entangled. A measurement of one of the photons enables the knowledge of the presence of the other: creating a heralded-SP source. Since the emission is announced, the protocol can be adapted to result in zero probability of event with no photon.

The first demonstration of entangled-photons pair generation was achieved in a bulk crystal of deuterated potassium dihydrogen phosphate (KD*P) using spontaneous parametric down conversion (SPDC) [32]. Two spatially separate beams, each

one containing a photon with a polarization along the same axis as its complementary particle, were used to test Bell's inequality. The scheme was pushed further using a novel type of SPDC (type II) to generate not only spatially separate photons but photons with orthogonal polarization using a β-BaB_2O_4 (BBO) crystal [33]. Such an entangled-photons source was used to first demonstrate quantum teleportation of a photon state in 1997 [31]. While such a process is being extensively used nowadays [34–36], much effort is being expended to augment its efficiency by moving to different crystals such as periodically-poled lithium niobate (PPLN) [37, 38] and/or $KTiOPO_4$ (KTP) [39–41] or using concentrated electric field schemes like waveguides [40] or laser cavities [41].

Waveguides because of the higher electric field enable the use of less efficient non-crystalline materials like dispersion-shifted fiber (kept at low temperature to inhibit other nonlinear effects) [42, 43] using four-wave mixing schemes [44, 45]. While these schemes exploit the material nonlinearity they are not SPDC schemes.

Unfortunately, these nonlinear SP sources still generate a Poisson distribution, with a non-zero probability to generate two-photons (much lower than an attenuated laser pulse source), and a high probability of zero-photons. The main purpose of those schemes is the generation of entangled-photons pairs. SP production is a by-product and it is not an on-demand SP source.

1.3.2 Ion-Trap System

This system was one of the first to be used to demonstrate the anti-bunching behavior [46, 47] of SP emitters. First, a beam of atoms needs to be generated and controlled. The passing atom is excited by two laser beams that isolate the system in the atomic state $|e\rangle$ to generate SP emission. As one can imagine, the manipulation of a single trapped ion or a single trapped atom requires a complex technical effort and the yield is relatively low. Recently the output has been improved by putting the single ion in a laser cavity [48], with SP generation efficiency just below 10%. Even then the price in experimental complexity is hardly justified by the need for a SP source for quantum information processing schemes where numerous sources would be required.

1.3.3 Nitrogen-Vacancy Centers in Diamond

A promising candidate for a SP source is the nitrogen-vacancy (N-V) center in diamond, where a substitutional nitrogen atom and a vacancy on an adjacent lattice position are used as the approximate two-level system. The diamonds are man-made and the density of N-V centers can be controlled. The N-V centers can be locally excited with a green laser and the fluorescence photon is around 637 nm. Unfortunately, the collection efficiency is low (~0.1%) [49]. Nevertheless, a N-V center has been used to demonstrate quantum key distribution [50]. Recently, photonic crystal (PhC) microcavity designs in diamond were proposed to improve the collection efficiency [51]. Current papers are reporting advanced electron spin manipulations [52–56]. The main advantages of the N-V centers are the fact they can be operated at room temperature

and the relative simplicity of the experimental setup.

1.3.4 Single Quantum Dots

The details of the physics of the QD are discussed in chapter 3. A QD can be viewed as an artificial atom, where both the electrons and the holes are confined by a parabolic potential. The recombination of the electron-hole pair results in the emission of a photon. With proper excitation, the QD can be viewed as a good approximation to the two-level system, where the transition from $|e\rangle$ to $|g\rangle$ is the recombination from the electron and hole ground states.

It is possible to experimentally generate a single exciton (quasi-particle representing the electron-hole pair) in a QD at a controlled time. Thus a SQD can be viewed as an efficient source of SPs. Chapter 4 is dedicated to a detailed description of the SQD and our experimental results with InAs quantum dots in an InP matrix (InAs/InP SQD). An InAs/GaAs SQD coupled with a microcavity was used to demonstrate QKD in 2002 [57], quantum teleportation in 2004 [58], Bell's Inequality violation [59], and LOQC [60]. So this is a relatively mature technology and one of the main limitations to commercial utilization is the low temperature required for the QD to have an atom-like DOS. InAs/InP SQDs have the advantage that they emit around 1.55 μm; an ideal wavelength for fibre-based processes.

The relatively long lifetime of the single exciton level, the random emission direction, the finite emission linewidths and the influence of the environment makes the

SQD an on-demand single photon source with a relatively low efficiency, whilst the photons are distinguishable because of the large jitter in emission time. The addition of a microcavity around the SQD, coupled to the single exciton level greatly improves both the yield and the indistinguishability of those photons [3,61,62]. The physics of the microcavities will be further explained in chapter 5 while our efforts to construct microcavities around InAs/InP are presented in chapters 7 and 8.

A SQD can also be used to generate a pair of polarization entangled photons via the bi-exciton decay process [63]. Although initial experiments only showed a strong correlation between the two photons [64–66], entanglement was recently proven [67–71]. The process is illustrated in figure 1.7. The QD is loaded with two excitons ($|\uparrow\Downarrow, \downarrow\Uparrow\rangle$). Radiative decay to the vacuum state can occur via two different paths, with different intermediate single exciton states: $|\downarrow\Uparrow\rangle$ or $|\uparrow\Downarrow\rangle$. In practice, the energy level of $|\uparrow\Downarrow\rangle$ is not equal to $|\downarrow\Uparrow\rangle$, although one can make them equal by using either an electric field, magnetic field or an optimized QD fabrication process. When the intermediate exciton states are degenerate, the two recombination paths are indistinguishable and the two emitted photons are entangled in their polarization degrees of freedom because the spin of the recombined exciton is passed on to the emitted photon. The link between the electron-hole spins and the polarization state of the emitted photon comes from a simple angular momentum conservation argument: the electron angular momentum is 1/2 whilst that of the hole is 3/2. Only the QD heavy holes are considered because their energy levels are lower than those of the light holes. The recombination of a spin-up hole with a spin-down electron yields a right circular polarized photon and opposite spins yields a left circular polarized photon.

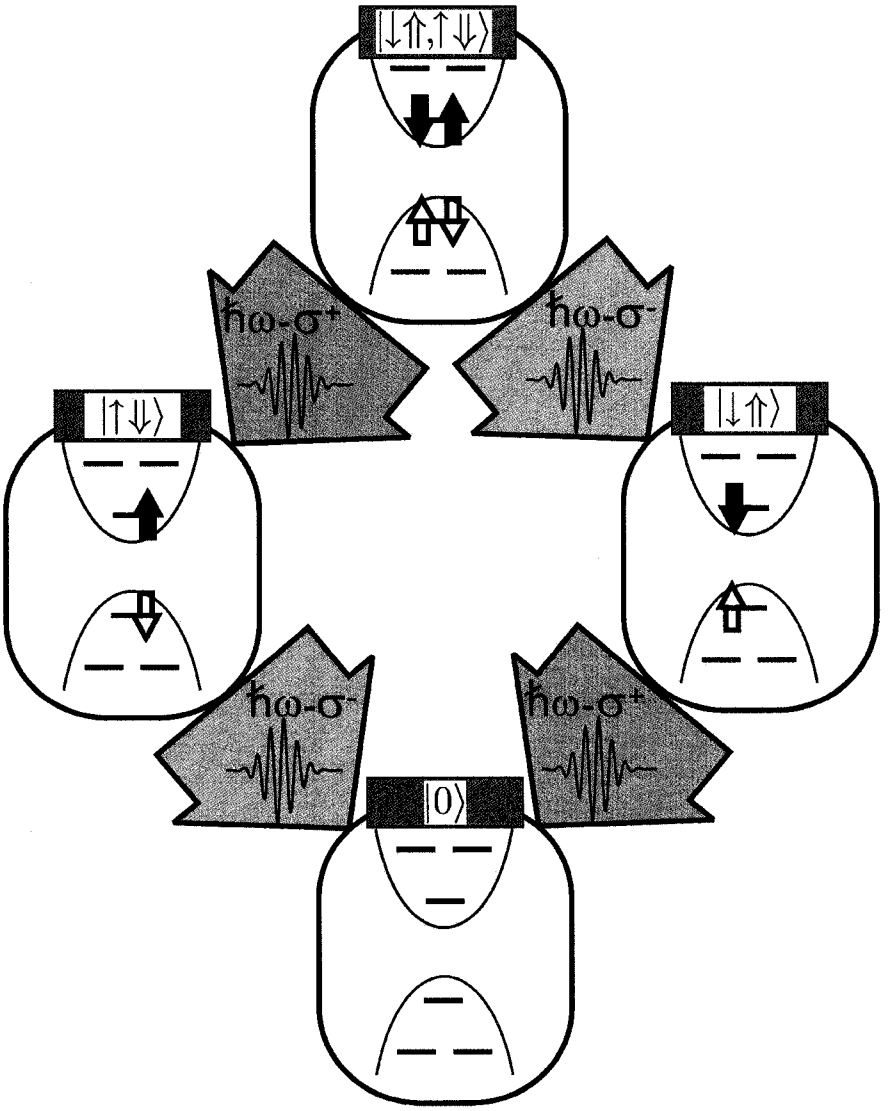

Figure 1.7: The two decay paths of the QD bi-exciton generating an entangled photon pair.

Chapter 2

Single Photon Detection

The difficulties in single photon (SP) detection are two-fold. First, very few detectors possess the sensitivity required to register a SP. The usual problems are either a detection threshold that is too high and/or too many "dark" counts - counts that appear in the absence of any input signal. Secondly, although it may be possible to detect a SP it is also necessary to prove that the detected signal came from a SP. While few detectors can discriminate the number of photons in a light pulse, advanced techniques with less precise detectors are available; the emission can be sent for example to a time-correlated single photon counting (TCSPC) setup, where two detectors are used and the anti-bunching nature of a single photon emitter can be confirmed with precise temporal information.

2.1 Hanburry-Brown and Twiss Correlation Spectroscopy

The photon detection process usually involves the annihilation of a radiation field photon and the generation of a charged particle that is counted as a mean of measurement. The probability of detecting an event between time t and $t+dt$ at a position $\vec{r}$ is proportional to $\omega_I dt$, where:

$$\omega_I(\vec{r},t) = \langle i|E^{(-)}(\vec{r},t)E^{(+)}(\vec{r},t)|i\rangle, \tag{2.1}$$

and $|i\rangle$ is the initial state of the radiation field. The physics discussed in this chapter can be found in greater detail in refs [1,72,73]. Assuming a linearly polarized electric field, the joint probability to detect an event at position $\vec{r}$ inside time t and $t+dt$ and another event at position $\vec{r}_2$ inside time t_2 and t_2+dt_2 is proportional to $\omega_{II}dtdt_2$, where:

$$\omega_{II}(\vec{r},t,\vec{r}_2.t_2) = \langle i|E^{(-)}(\vec{r}_2,t_2)E^{(-)}(\vec{r},t)E^{(+)}(\vec{r},t)E^{(+)}(\vec{r}_2,t_2)|i\rangle. \tag{2.2}$$

Only the time difference $\tau = t-t_2$ is relevant for a statistically invariant field. The normalized second order quantum mechanical correlation function is then a statistical average over all the possible initial fields:

$$g^{(2)}(\vec{r},\tau) = \frac{\langle E^{(-)}(\vec{r},t)E^{(-)}(\vec{r},t+\tau)E^{(+)}(\vec{r},t+\tau)E^{(+)}(\vec{r},t)\rangle}{\langle E^{(-)}(\vec{r},t)E^{(+)}(\vec{r},t)\rangle\langle E^{(-)}(\vec{r},t+\tau)E^{(+)}(\vec{r},t+\tau)\rangle}. \tag{2.3}$$

Classically the correlation function is given by:

$$g^{(2)}_{classical}(\tau) = \frac{\langle I(t+\tau)I(t)\rangle}{\langle I(t)\rangle^2}. \tag{2.4}$$

This means:

$$g^{(2)}_{classical}(0) \geq 1, \tag{2.5}$$

$$g^{(2)}_{classical}(0) \geq g^{(2)}_{classical}(\tau), \tag{2.6}$$

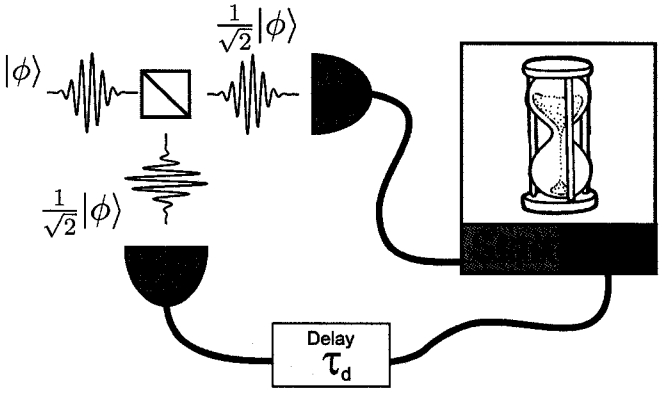

Figure 2.1: Hanbury-Brown and Twiss setup cartoon representation [74].

where the Cauchy-Schwarz inequality was used ($|\vec{x}\cdot\vec{y}|^2 \leq (\vec{x}\cdot\vec{x})(\vec{y}\cdot\vec{y})$ or in the quantum mechanic formalism $|\langle xy\rangle|^2 \leq \langle x\rangle\langle y\rangle$) was used. It can be shown that for a thermal source $g^{(2)}(0) = 2$ while for an ideal laser (δ-function linewidth) $g^{(2)}(0) = 1$ [1]. For the quantum mechanical second order correlation function it is possible to obtain values for $g^{(2)}(0)$ lying between 0 and 1 when the photons are anti-bunched. This means the detection of a photon at one time and place makes it less likely to be detected at another.

To measure the second order correlation, a Hanbury-Brown and Twiss interferometer is used [53], as is shown schematically in figure 2.1. The SP emission is sent to a 50/50 beam splitter and each emerging beam path is then sent to a detector. If the emitter launches one photon at a time only one detector can register a hit at a time, so that $g^{(2)}(0) = 0$.

The actual experiments are slightly more complex since we do not perform the measurement only at $\tau = 0$. A precise chronometer (resolution $< 100\,\text{ps}$) within a

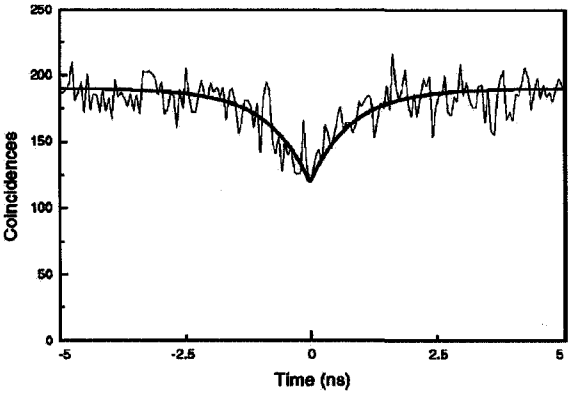

Figure 2.2: First reported TCSPC experiment with InAs/GaAs with a continuous excitation [75]

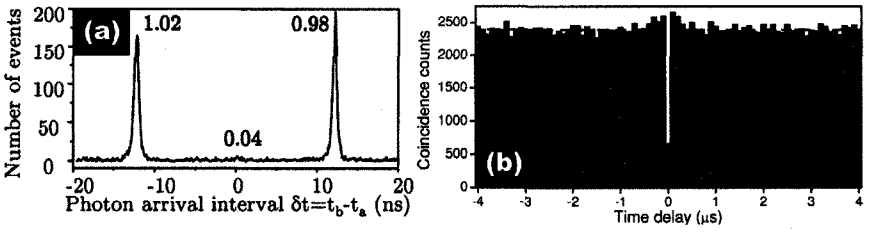

Figure 2.3: Anti-bunching measurements for pulsed excitation with InAs/GaAs SQD emitting in the visible [62] **(a)** and in the near-infrared [76] **(b)**

computer measures the time difference between a hit on detector 1 and subsequent hit on detector 2. An electronic delay τ_d is inserted in one of the arms to help the chronometer make the measurement. For clarity, τ_d is subtracted from the data before plotting it. When the emission process is random, $g^{(2)}(\tau)$ will be a flat line. For a SP source a dip at $\tau = 0$ appears. The dip width is directly related to a subsequent photon emission lifetime if continuous wave excitation is used. An example of such a result for an InAs/GaAs single quantum dot is shown in figure 2.2.

In the case of pulsed excitation $g^{(2)}(\tau)$ looks different, but the principle stays the

same. Instead of a flat line with a dip at $\tau = 0$, $g^{(2)}$ will consist of peaks, separated by the laser repetition rate, with an amplitude approximately equal to one. At $\tau = 0$ the peak will be missing and $g^{(2)}$ will approach zero, as shown in figure 2.3(**a**) for an InAs/GaAs SQD in a low Q microcavity. If the jitter within the electronics is small enough, the peak full width at half maximum (FWHM) can be related to the energy level lifetime. For detectors with high dark count levels, the detectors are only "activated" for short temporal windows when the photon arrival is expected. In such an experimental setup, the internal jitter so high that the timing information is almost irrelevant within the short window where the detector is turned on. In this situation, the $g^{(2)}(\tau)$ data becomes a bin-like graph as shown in figure 2.3(**b**). Our TCSPC experimental results with an InAs/InP SQD will be presented in chapter 4.

2.2 Detectors

To measure a SP one can use a micrometer size tungsten square on a pillar at very low temperature ($\approx$ 300-400 mK). At this temperature the tungsten is just over its superconducting threshold. A photon hitting the tungsten generates enough heat within the sample to bring it out of the superconducting regime, and produces a sudden increase in resistance [77, 78]. This type of detector is referred to as a transition edge sensor. The technique is quite remarkable since it is able to distinguish between events where there is one colliding photon, two photons and more. Plus, it works for a very broad range of the spectrum. However, it has drawbacks. Firstly, in addition to the complications involved in working at these temperatures, it is also costly to sustain such a temperature. Secondly, the detector needs a relatively long

time to recover from the event-induced temperature change. This greatly limits the achievable repetition rate. And thirdly, it is relatively difficult to redirect photons to the detector and many photons are lost in the process. Plus, doing so can generate heat lost within the cryostat.

Another type of transition edge sensor has been developed recently [79, 80]. The new type uses a superconducting nanowire of niobium nitride (NbN). The advantage of the nanowire resides in the higher temperature of operation (3.1-4 K). To improve the detector cross-section the nanowire is arranged in a meander-like fashion. This results in a low-jitter, low dark count and high bandwidth detector. Photon-number resolving detection has yet to be demonstrated, but in theory it should be possible. In current publications, the NbN nanowires are used within a Hanburry-Brown and Twiss interferometer to do TCSPC [80].

2.2.1 Avalanche Photodiodes

A good way to reach a high repetition rate while preserving a good detection efficiency is to completely discard the photon-number resolving capability. An avalanche photodiode (APD) is a commonly used type of detector in the telecommunication world. It can be viewed as an analog to the photomultiplier tube as current amplification is done through an avalanche process within it. Its internal current gain makes it suitable for low light levels. For the visible part of the spectrum silicon-based APDs are used while the 1.2 to 1.7 μm range is covered by InGaAs-based APDs.

To make it sensitive to even lower light levels (*e.g.* a SP) the APD is biased

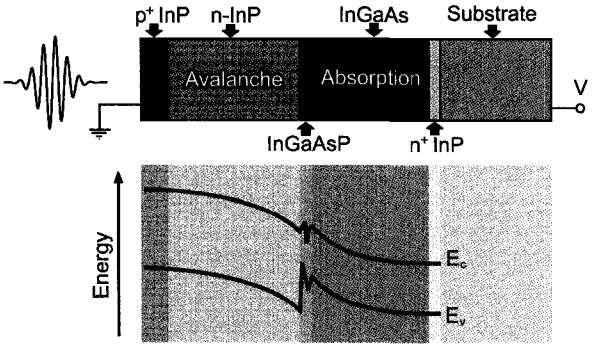

Figure 2.4: Schematics diagram of an InGaAs/InP APD. From [81]

close to or over its breakdown voltage. When a SP impinges on the detector the excited electron is enough to trigger an avalanche. Figure 2.4 illustrates a typical InGaAs-APD structure and the bottom panel shows the device band structure. The absorption and avalanche areas are separated, while the p-n junction is created at the p^+InP/n-InP interface. By increasing the bias, the depletion layer will reach the InGaAs (*i.e.* the absorption area) and the device then becomes sensitive to light. The electrons and holes created within the InGaAs can undergo a drift because of the non-zero electric field and can reach the multiplication region. The purpose of the thin InGaAsP layer is to smooth the transition with respect to bandgap between the InP (E_{gap}=1.35 eV at room temperature) and the InGaAs (E_{gap}=0.73 eV at 300 K). As a result, the holes can cross the barrier more efficiently, and the bandwidth of the device is increased. It is important to note that APDs were not primarily constructed for SP detection, although the last few years have seen companies starting to make optimized versions of their APDs for extreme low light levels which are referred to as single-photon avalanche photodiodes (SPADs). Both SPADs and APDs are limited in repetition rate by the fact that the diode must be "recharged" to be able to generate a subsequent avalanche.

The photon capture and avalanche processes are quick (< 2 ns) and reproducible but, when the APD is biased to be single photon sensitive, the avalanche process will yield an electrical pulse with a constant amplitude regardless of the amount of light hitting the detector. The timing information is good (jitter < 50 ps), but no information regarding the quantity of light can be extracted.

The higher the bias the more sensitive the detector becomes. But a higher sensitive comes with a price. Random events, also known as dark counts, are more likely to happen. Either a lost photon coming from somewhere else or an electron trapped in the material getting released can generate dark counts. The material quality is therefore a primary consideration when designing an efficient, low noise SP detector for TCSPC applications. The dark counts will pollute the signal and hide the data. It comes as no surprise that Si-based APDs have a much higher fabrication quality than the InGaAs-based ones. In fact, Si-APDs are so good (high sensitivity, low dark counts) that they can be operated in "single-photon-sensitive" mode continuously, *i.e.* a bias slightly below the breakdown voltage, and a diode temperature of -50°C. For InGaAs-APDs the dark counts are too high for them to be operated continuously and one must bias them for minimal amounts of time to limit the dark counts. This operation mode is called Geiger mode. Basically, the pulse used to trigger the source is also used to trigger the detection with some delay to synchronize the event with the detector bias pulse. The bias pulse amplitude is added to a DC bias applied to the detector (typically 1-2 Volts below the breakdown voltage) to bring the total voltage

slightly above the breakdown voltage when the pulse is applied. The operation temperature is the same as for the Si-APDs. Typically, the detector is left "ON" for only 1 ns; long enough to allow some experimental jitter but short enough to drastically reduce the dark count rate.

To prove that the light coming from a SQD is indeed a SP one typically makes an anti-bunching measurement with a Hanburry-Brown and Twiss interferometer [21,74] as shown in figure 2.1. Our initial results using such a system with an InAs/InP SQD are presented in chapter 4

Chapter 3

Self-Assembled Quantum Dots

This chapter introduces the concept of a quantum dot (QD) and a self-assembled quantum dot (SAQD) and discusses some of the characterization techniques that are available to study them. Much of the pioneering work has been done using InAs/GaAs and InGaAs/GaAs QDs simply because they were readily available and could be fabricated with higher quality than dots from competing materials systems. In addition, because they emit in the visible part of the spectrum, the detection of photons emitted from these dots is technologically simpler (using cooled charge coupled device (CCD) array, Si APDs, etc.). This thesis focuses on QDs for fibre-based applications, thus emitting in the near infrared (NIR). The second section introduces the various QD types and other nanocrystals that emit in the NIR including our specific QDs for the NIR: chemical beam epitaxy (CBE)-grown InAs/InP SAQDs. The third section focuses on the physics of the QD and its emission properties, whilst the last section presents various QD characterization techniques.

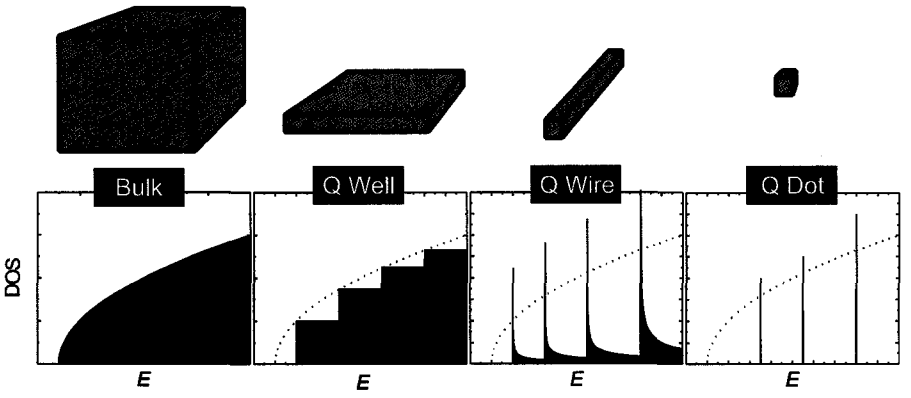

Figure 3.1: Schematic representation of the various electronic DOS for different quantum structures: quantum well, quantum wire and quantum dot compared to bulk DOS.

3.1 What is a quantum dot?

A QD is a semiconductor nanocrystal embedded within a material of higher bandgap. Because of its small size, electrons and holes contained within the dot are effectively confined within a three dimensional potential well. Figure 3.1 compares the electronic DOS for quantum wells, quantum wires and quantum dots with that of the bulk material. Three dimensional confinement results in a discrete DOS for both electrons and holes. The electron-hole (also known as a quasi-particle called exciton) recombination leads to the emission of a photon. The QD emission spectrum is discrete because of the electron and hole discrete DOS. The physics behind this will be further explained in section 3.3.

Another important consideration is ones ability to engineer the QD properties through careful choice of the nanocrystal proportions, material composition and

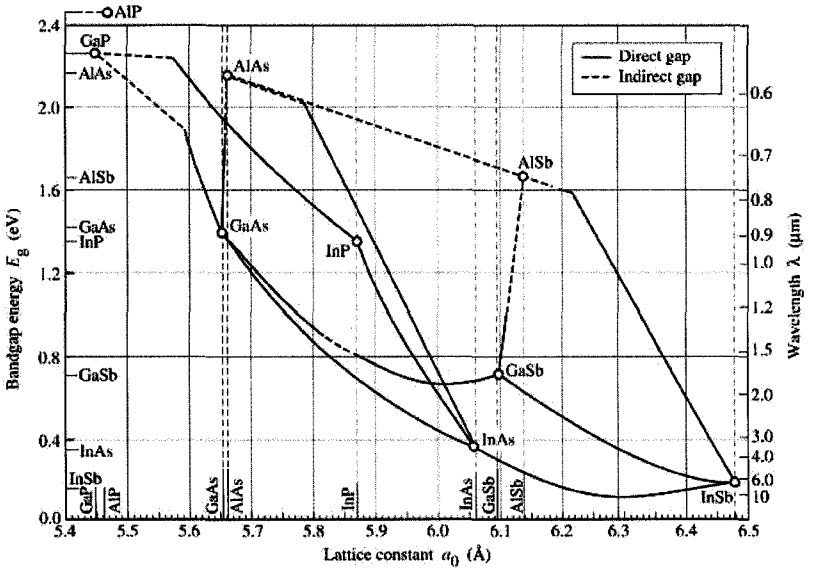

Figure 3.2: Bandgap energy as a function of the lattice constant for various III-V semiconductors at room temperature. Solid lines are direct gap material whereas the dashed lines are indirect gap ones. From [82]

cladding. Many different techniques exist to produce QDs and a large selection of different materials exist that are suitable for QD formation. It would be rather tedious to list them all here, but as an example, figure 3.2 illustrates the bandgap energy as a function of lattice constant for some relevant III-V semiconductor materials. Using advanced epitaxial techniques it is possible to isolate a nanocrystal of semiconductor material within a second material of higher bandgap, thus creating the 3D confinement required, provided that the nanocrystal size is small enough. The InAs/InP QDs used in the present work are formed using the Stranski-Krastnow growth mode in a chemical beam epitaxy system. This procedure will be discussed later in this chapter. A more detailed description of recent progress in the growth techniques for InAs/InP QDs can be found in the thesis of Danny Kim [83].

3.2 Epitaxial Growth and Quantum Dots

The QDs used here are epitaxial QDs. They are created in a growth chamber where the layers of atoms are deposited one by one, *i.e.* a monolayer (ML) at a time. Epitaxial growth techniques have found many commercial applications and have been used to produce quantum wells (QWs) for a number of decades already.

There exist three main epitaxial modes of growth, Volmer-Weber, Stranski-Krastanow and Frank-van der Merve. Each mode appears in response to certain material properties. The interface energy between epilayer and substrate, the strain energy and the surface energy of the QD material (low bandgap material) are the crucial parameters. The interface energy describes the ability of one material to grow on another, the strain energy describes the degree of lattice mismatch between the two and the surface energy describes the cost for a material to take up a specific shape. For growth where the interface energy is high, the adatoms will have a tendency to form islands on the surface to minimize this interface area. This is the Volmer-Weber type of QD growth.

When the interface energy is low, adatoms incorporate across all of the surface, forming a wetting layer a few MLs thick. If the stress induced by lattice mismatch is low, the epilayer will remain two-dimensional, corresponding to layer by layer growth; this is the Frank-van der Merve growth mode.

A higher lattice mismatch encourages the formation of stress-relieving islands on top of the wetting layer. The onset of island formation is spontaneous, corresponding

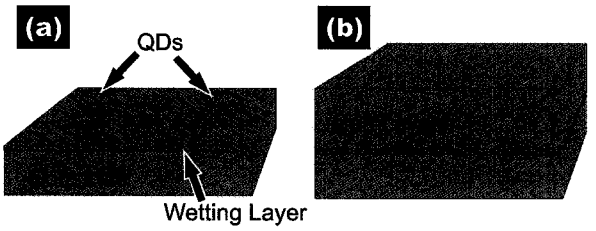

Figure 3.3: **(a)** Stranski-Krastnow type of QDs created by lattice mismatch. **(b)** Optically active QDs layer where a cap layer as been added over the nanocrystals formed in **(a)**.

to the terminology "self-assembled". This epitaxial regime is referred to as Stranski-Krastanow growth and is illustrated in figure 3.3**(a)**.

In order to obtain full, three dimensions (3D) confinement for electrons and holes within the nanocrystal, a layer above the QDs (known as the cap layer), with a bandgap larger than the QDs themselves and usually of the same material as the substrate, is grown, as shown in Fig.3.3**(b)**.

3.2.1 Near-Infrared Quantum Emitters

Several groups want to build bright light sources for the near infrared (NIR) using various growth processes and techniques. The emission wavelength of the QDs depends on their material composition and the surrounding material. Figure 3.2 shows the bandgap for various III-V semiconductors. InAs QDs in a GaAs matrix produce light around 800 nm, *i.e.* a photon energy of 1.4 eV, while InAs/InP QDs produce photons around 1550 nm. The bandgap of GaAs is similar to that of InP and the difference in emission wavelength for InAs/InP QDs with respect to InAs/GaAs QDs is a direct result of the different lattice mismatch. The lattice constant of the InP

is closer to that of InAs and the resulting QDs are under smaller strain than for dots in GaAs. It is possible to tune the strain within the QD using advanced growth techniques involving a thin stress relieving layer (SRL) and/or growth interruptions. The lattice mismatch also results in a different dot shape. While the InAs/GaAs QDs have a lens-like shape after the growth of the capping layer, InAs/InP QDs have a shape that is closer to a square based platelet, with a height about 3-4 times smaller than the lateral dimension.

There are many types of growth techniques that can produce epitaxial Stranski-Krastanow, InAs/InP SAQDs: metal organic chemical vapor deposition (MOCVD) [84,85], metal organic vapor phase epitaxy (MOVPE) [86–88], molecular beam epitaxy (MBE) [89], solid-phase MBE [90–92] and CBE [93]. Other types of low-dimensional InAs/InP-based structures also emitting at about 1.55 μm can be fabricated including quantum wires [94–98], quantum sticks [99, 100], and quantum dashes [101–105].

InAs/GaAs + Stress-Relieving-Layer

The idea here is to manipulate the self-assembly process using a SRL between the QD layer and the cap layer. This technique has been around for a few years now and has been used with high success to produce 1.3 μm-single quantum dot with MBE growth and InGaAs-SRL [76, 106–109].

It is a little bit trickier to push InAs/GaAs QDs further up in wavelength and only recently have people reported such results, using MBE and a InGaAsSb SRL [110], or MBE and $In_xGa_{1-x}As$ SRL [111]. A third group has used MOCVD and an

InGaAs SRL but their QDs overshot the desired wavelength into the 1.6 to 1.9 μm range [112, 113].

InAs/InP + Stress-Relieving-Layer

As for the InAs/GaAs QDs, a thin (few ML) layer is deposited onto the QD layer to relieve the stress before the capping layer is deposited. Three different groups are using an InGaAsP SRL layer, two using MOCVD growth [114–116] while the other group grows their samples with MOVPE [117]. Other groups are using SRLs without phosphine; InAlGaAs [118] and GaAs grown by MOCVD [119].

InAs/InP + Double-Cap

This technique is quite similar to the previous one except the SRL is in the same material as the capping layer but grown at a different rate with an optimized growth interruption period. One group uses (311)B substrates and MBE growth [120], while another group uses an MOCVD growth chamber [121–123]. They can even generate site-selected InAs/InP SQD within lithographically-fabricated, nanometer size holes [124–129].

InAs/InP (001)

This section reviews the various works on InAs/InP QD growth using InP(001) substrates, without any of the variations mentioned earlier. Groups have grown samples with MOVPE [86–88, 130–132] and also with MBE, but with limited success [133].

Our work with these QDs is presented in the next section.

3.2.2 Our InAs/InP(001) Quantum Dots

The growth technique used to produce the samples for my work is chemical beam epitaxy (CBE). Gas beams of trimethyl-indium (TMI) and arsine (AsH_3) are required to produce an InAs layer whereas TMI and phosphine (PH_3) generates InP. A mixture of arsine, triethylgallium (TEGa) and TMI is used to grow InGaAs. The principal feature of CBE growth with respect to others is the fact that the chemical reaction occurs on the surface. The different adatoms migrate for a time on the surface before being captured into crystal sites. Precise control over the gas flow rate and substrate temperature are critical to generate uniform and pure layers.

We grow our samples using a RIBER 32P CBE system. The AsH_3 and the PH_3 are cracked at 850^{o}C in a fast switching cracker cell to generate As_2 and P_2 and injected into the chamber. The TMI and TEGa are injected into the chamber through a low temperature gas injector held around 100^{o}C. We used InP(001) substrates and the growth temperature was fixed at approximately 520^{o}C.

First, an InGaAs layer was grown, the thickness of which is determined by the desired end use. If the InGaAs layer was meant to be a simple etch stop its thickness was around 400 nm. A thicker layer ($> 1\,\mu$m) is required to construct a photonic crystal membrane because the InGaAs will be replaced by air to confine the photons by total internal reflection. The InGaAs growth rate was fixed to $1\,\mu$m/hour. Subsequent steps, describing our QD growth procedure, are depicted in figure 3.4.

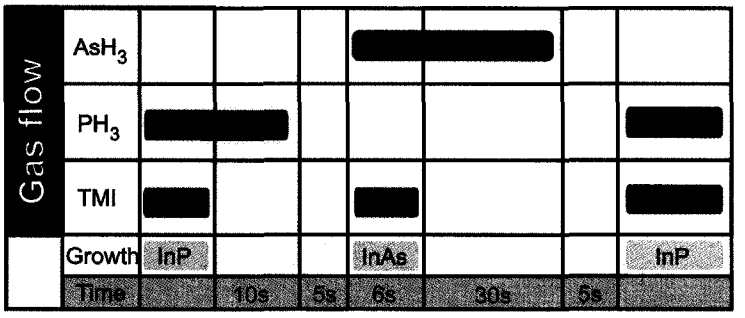

Figure 3.4: Schematic representation of the growth of a InAs/InP SAQDs layer. From [93].

Following the initial InGaAs layer, an InP buffer layer was grown using TMI and PH_3 flow at a rate of 0.51 ML per second (ML/s). When the buffer thickness reached the desired value (depending on the intended purpose) the TMI flow was stopped while the PH_3 continued for 10 seconds to smooth the InP. Before growing the InAs layer at the same rate, a 5 s pause was included to evacuate the residual gases in the chamber.

An InAs thickness of 3.1 ML was grown to ensure the formation of 3D islands (they appear at 2.5 ML in this material system [93]). This layer thickness is directly related to the resulting QDs density. A 3.1 ML layer results in $\sim$100 QDs/μm^2. As for the InP buffer layer, two growth interruptions follow. The first one lasts 30 s with an AsH_3 overpressure to allow the InAs layer to reduce strain energy by the formation of QDs. The second 5 s pause again eliminates the remaining hydrates. An InP cap layer was grown at 0.95 ML/s, a faster rate to reduce the amount of As/P exchange at the dot surface. The cap layer thickness is again dependent on the end application of the sample, but for our purposes it is almost always the same as the buffer layer in order to generate a QD layer at the center of the grown structure; preferable if one

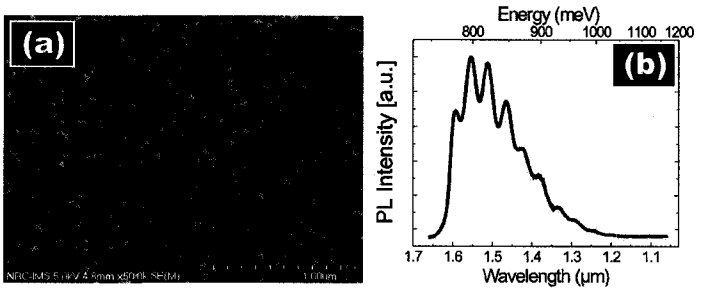

Figure 3.5: Typical CBE grown InAs/InP QDs used in this work. **(a)** SEM image of an uncapped layer. **(b)** PL spectrum of a QDs ensemble.

wants to couple to a microcavity mode.

Figure 3.5**(a)** shows an SEM image of an InAs/InP QD layer without the cap layer and **(b)** the photoluminescence (PL) spectrum of a typical InAs/InP QD ensemble. A detailed explanation of both those characterization techniques will be given later in this chapter. The key difference between InAs/InP QDs and other QDs is their emission wavelength around 1550 nm; the ideal wavelength for optical fibre-based transmission *i.e.* the telecommunication C-band. As can be seen from the wide emission spectra from the ensemble PL, the dots can even be used in the S- and L-band.

One can isolate a SQD from such a planar QD ensemble by depositing a mask with numerous nanometre sized holes or by etching similar sized mesas. One then searches for the mesa or hole that happens to have a single quantum dot by chance. It would be very useful to be able to produce a SQD at a desired location on the sample. A novel technique using selective area epitaxy [134, 135] to produce clean SQDs at a desired position was developed at the Institute for Microstructural Sciences (IMS). It will be further discussed in section 4.2.

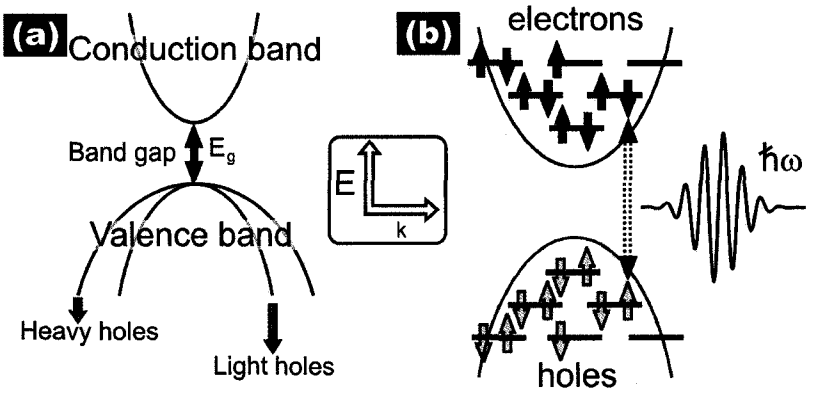

Figure 3.6: **(a)** Schematic band structure of the direct band gap semiconductor. **(b)** Cartoon representation of the QD energy level. Exciton recombination yields the emission of a single photon. From [136]

3.3 Quantum Dot Energy Structure

The Hamiltonian of a d-dimensional harmonic oscillator *i.e.* a particle in an infinite-barrier parabolic potential, is given by:

$$\hat{H} = \frac{\hat{p}^2}{2m^*} + \frac{1}{2}\sum_{i=1}^{d} m^*\omega_0^2 r_i^2, \tag{3.1}$$

where ω_0 is the oscillator frequency, $\hat{p}$ the momentum operator and m^* is the particle effective mass. Its solutions are given by:

$$E_n = \left(n + \frac{1}{2}\right)\hbar\omega_0, \tag{3.2}$$

where n is an integer. It has been shown that in lens-shaped, quasi-two-dimensional SAQDs, the bound states of both the electrons and valence-band holes can be approximated using effective mass theory and a parabolic confinement potential [136–138]. The single particle levels then correspond to the levels of a two-dimensional simple

harmonic oscillator with energies given by:

$$E_{mn} = \hbar\omega_0(m+n+1), \tag{3.3}$$

and eigenstates $|mn\rangle$. As for atoms, when $m+n=0$ the electron is in the s-shell, $m+n=1$ corresponds to the p-shell, $m+n=2$ the d-shell etc. Because we are talking about electrons and holes the m,n quantum numbers must be expanded to include the spin, σ, which can take values $\uparrow$ or $\downarrow$.

For electrons the angular momentum is given by $L^e_{mn} = m-n$ whereas for the holes it is $L^h_{mn} = n-m$. Considering eq.(3.3), the spin degeneracy, the different angular momentum values and the fact that the strain in the system removes the light hole - heavy hole degeneracy to give a heavy hole ground state, one can consider the QD energy levels to be as illustrated in Fig.3.6(**b**). The discrete nature of the QD energies is contrasted with the band structure of a bulk direct-gap semiconductor (Fig.3.6(**a**)). This simplified model ignores electron and hole Coulomb interactions. As the QD gets populated, the energy levels change in response to electron-electron, hole-hole and electron-hole interactions. These effects can only be treated numerically. Typically, the QD Hamiltonian is given by [137]:

$$H = \sum_i E^e_i c^\dagger_i c_i + \sum_i E^h_i h^\dagger_i h_i - \sum_{ijkl}\langle ij|V_{eh}|kl\rangle c^\dagger_i h^\dagger_j h_k c_l + \frac{1}{2}\langle ij|V_{ee}|kl\rangle c^\dagger_i c^\dagger_j c_k c_l + \frac{1}{2}\langle ij|V_{hh}|kl\rangle h^\dagger_i h^\dagger_j h_k h_l, \tag{3.4}$$

where $c^\dagger_i$ (c_i) and $h^\dagger_i$ (h_i) create (annihilate) an electron or valence-band hole in the state $|i\rangle$ with the single particle energy E_i while the indices $\{ijkl\}$ are each composite indices each referring to $[m,n,\sigma]$. While $\langle ij|V|kl\rangle$ are two-body Coulomb matrix

elements for electron-electron (ee), hole-hole (hh), and electron-hole (eh) scattering, respectively [137].

To determine the emission properties of the QD, one must consider the total angular momentum of the recombining electron ($\sigma_e = \pm 1/2$) and heavy hole ($\sigma_h = \pm 3/2$). The sum of both spins must be equal to ± 1 for a photon to be emitted. Cases where the total angular momentum is ± 2 are optically forbidden. That is to say the electron and hole spins must be opposite for them to recombine. An angular momentum of $+1$ (-1) means a right (left) circularly polarized photon. Moreover, for recombination to occur between an electron and a hole state it is required that their indices m and n are equal according to Fermi's Golden Rule [138, 139]. Simply put, this means that their wavefunction must overlap spatially for recombination to occur. This is illustrated in figure 3.6(**b**) by the different positions along the k-axis of the different states with the same energy. Only the electron and hole energy levels which are vertically aligned will generate the emission of photons.

3.4 Characterization Techniques

The two techniques mainly used for my work are scanning electron micrograph (SEM) imaging and photoluminescence (PL) measurements and these will be described in detail in the following sections. Other techniques include: atomic force microscopy (AFM), electro-luminescence (EL), photocurrent, cathodoluminescence (CL), photoluminescence excitation (PLE) etc. Both AFM and SEM will examine the QD

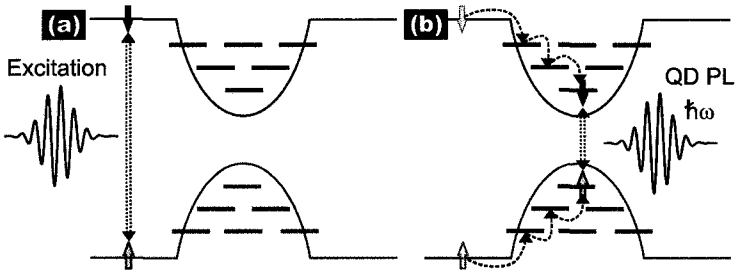

Figure 3.7: Schematical representation of standard photoluminescence (PL) measurement process. **(a)** Photon absorption creates an exciton and **(b)** Electron and hole relax to the lowest energy levels to recombine.

surface with high precision, but to perform them one cannot cap the sample. Consequently, such measurement are always a little doubtful since growth of the cap layer can change the QD height, width and composition through interdiffusion. For PL, EL, and CL, one looks at the photons emitted by the sample when excited by either photon absorption, electrical current or an electron beam respectively. The collected spectrum of the emitted photons gives us information about the QD properties. The PLE technique, as its name suggest, is similar to PL except that instead of measuring the emitted spectrum, a single emission wavelength is measured as the excitation laser wavelength is tuned. Photocurrent measurements read the generated current in the sample under laser illumination; the photocurrent as a function of the excitation wavelength and/or power provides information about the system. If the laser wavelength matches an optical level of the QD it will be more strongly absorbed and result in higher photocurrent.

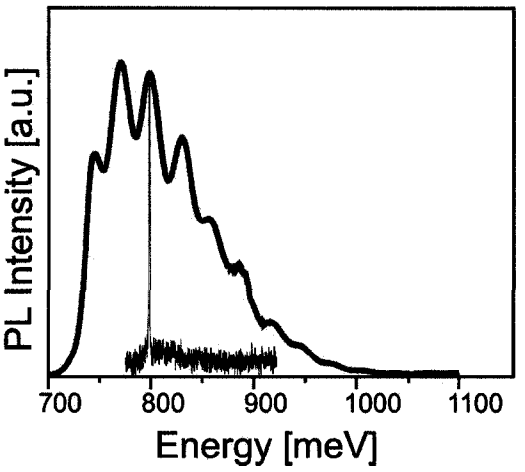

Figure 3.8: PL curve for a QDs ensemble (red curve) versus a SQD (black curve).

3.4.1 Photoluminescence

Instead of measuring directly the parameters of the QD, like size and shape, PL probes its intrinsic properties, *i.e.* its energy levels. An excitation laser illuminates the sample creating excitons in the host material and/or in the wetting layer. The electrons and holes will drift around, sometimes recombining in the cladding material and sometimes falling into a QD. Figure 3.7 shows a schematic representation of a photon absorption within the wetting layer(**a**), with the excited electron and hole dropping into the QD and then relaxing to the lowest unoccupied state(**b**). Their eventual recombination yields the emission of a photon. Consider now a situation where many electrons and holes in the QD produce emission at different energies corresponding to the QD energy levels. A good way to extract information from a PL spectrum is to measure it as a function of pumping power, *i.e.* the number of excitons generated within the dot. Figure 3.8 shows a typical PL spectra for a QD ensemble (red line) and for a SQD black line.

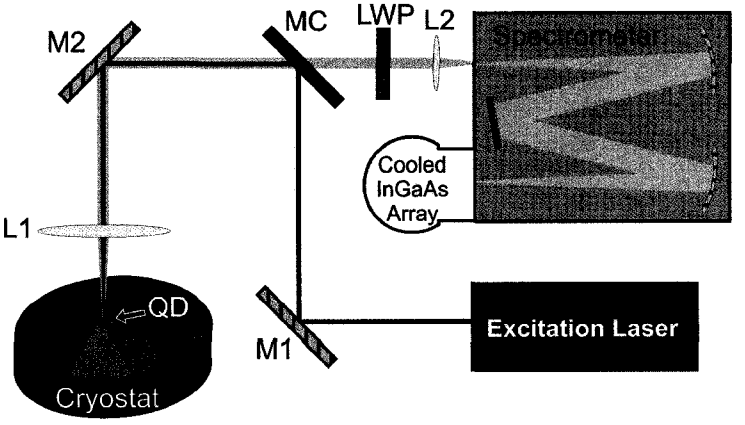

Figure 3.9: Typical photoluminescence (PL) setup. See text for a detailed description.

Figure 3.9 presents a typical PL setup. Excitation photons are brought to the sample using mirrors M1 and M2, while mirror MC reflects the laser while being transparent to photons emitted by the QDs (for our QDs we use a cold mirror which reflects visible light and allows infrared light to pass through). A microscope objective (L1) is installed in front of the sample to focus the excitation and collect the QD emission. The sample is usually mounted in a cryostat where it can be measured at temperatures as low as 4 K in order to clearly see the QD emission lines without any perturbation and broadening from phonons.

The excitation laser is usually at a wavelength such that photons are absorbed by the substrate (InP in our case) and wetting layer (InAs) as well as by the QDs (InAs). The PL photons, emitted at a longer wavelength than the excitation photons, are collected by the same microscope objective or lens and sent towards the spectrometer in front of which are placed a long wavelength pass filter (LWP) and a lens to focus the light into the spectrometer properly. The spectrometer depicted in Fig.3.9 is a single grating system. The light dispersed by the grating is sent to the detector – a

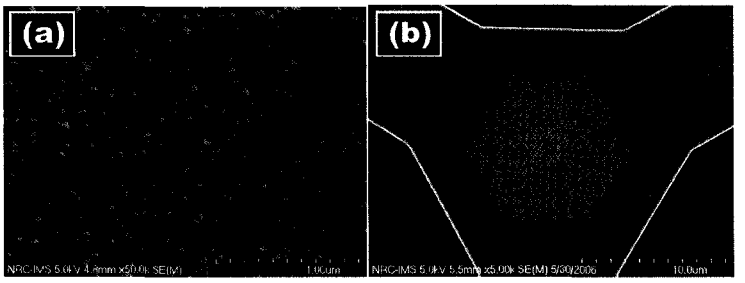

Figure 3.10: Typical SEM images. **(a)** shows the surface full of un-capped InAs/InP SAQDs as grown in our CBE system (see section 3.2.2 for a more detailed description) and **(b)** introduces the image of PhC microcavity (more information will be given in following chapters).

cooled InGaAs array from Jobin-Yvon – in order to be able to see the InAs/InP QD PL which is around 1.55 μm.

3.4.2 Micro-photoluminescence

micro-photoluminescence (μPL) is simply PL using a stronger microscope objective, resulting in a smaller excited and probed area. μPL is required or at least highly desirable if one wishes to probe a single quantum dot. Moreover, a small probed area means we now have the ability the measure a 2D map of the system PL.

3.4.3 Scanning Electron Microscope

Images from a scanning electron micrograph (SEM) are now used routinely for characterization. Scanning electron microscopy involves focusing a beam of electrons onto the surface to be studied. The focused electron beam generates an interaction volume within which the electrons lose energy by repeated scattering and absorption. The sample then re-emits electrons and electro-magnetic radiation. It is possible to

generate an image of these processes when differences in material composition and/or thickness provide different response. In Fig.3.10, two examples of samples characterized by SEM we performed are presented. Fig.3.10(**a**) shows a typical InAs/InP SAQD layer and (**b**) presents a typical PhC microcavity in InP (see chapter 8 for a detailed explanation of the PhC microcavity).

Chapter 4

Single Quantum Dots

The previous chapter described how one may produce SAQDs using the Stranski-Kratanow growth mode. This growth procedure can be optimized to produce different QD densities and varying QD properties and these QD layers are suitable for laser-sources or solar cell applications. In order to access the atom-like properties of a QD for quantum information processing however, it is vital to isolate the optical emission from a single quantum dot (SQD). Originally, the two main ways to do this involved the use of etched mesas or masks. Basically, a low dot density sample was grown and, using lithographic techniques, large portions of the sample were etched away to leave a small region of the sample that hopefully contained a SQD. An alternative approach is to deposit material onto the sample, blocking the optical emission except for transmission through a small hole underneath which a SQD hopefully lies. The isolated SQD PL is measured with a standard μPL setup to ensure collection from one structure at a time.

The first report of SQD-like PL was made in 1992 by Brunner *et al.* [140]. The SQD was isolated and created by a metallic mask. The first single SAQD PL was

reported by Marzin *et al.* [141], where the QD was removed from its neighbors by etching a mesa. The state-filling behavior observed as a function of increasing excitation power was a clear signature of a SQD but was not a proof of SP emission. After these two reports the SQD field blossomed considerably for InAs/GaAs and other visible light emitting QDs [142]. The measurement of near infrared SQD emission proved more challenging and only recently has it been reported. These results will be described in detail in section 4.1 of this chapter.

More recent techniques to isolate a SQD include two schemes for finding the location of a QD underneath the capping layer. The first involves the nucleation of subsequent layers of QDs on top of a low density QD sample [143]. Although the QDs on top are not interacting with the QD of interest, they reveal its position because QDs in the superimposed layers above nucleate aloft the original QDs due to the remanent stress. The second technique is even simpler. For a thin enough capping layer the QD position is revealed by a bump on the cap layer surface that can be located by AFM [144]. A clever "plug and play" technique was introduced by Toshiba labs. A fiber bundle is glued onto the sample, covering a large area of the sample [145]. Each fiber in the bundle probes a few square microns of the sample surface and by simply testing each fiber, a SQD can be found and studied.

One way to cut through the dot location difficulties would be to produce a SQD at a desired location on the sample. Such control can be achieved with various techniques. The group at the IMS has developed a novel technique using selective area epitaxy to produce a small, clean and isolated area where a SQD will nucleate. It

will be introduced in section 4.2. Section 4.3 shows our anti-bunching results with our site-selected InAs/InP.

4.1 Single Quantum Dot in the Near Infrared

As was mentioned in chapter 1, the race to achieve an efficient single photon source at 1.55 μm is world-wide. The isolation of a SQD requires good control of the growth and fabrication procedures. Of all the groups involved, few have managed to isolate a SQD, and even less have demonstrated the SP emission characteristics. The most success has been achieved with InAs/GaAs at 1.3 μm (another interesting window for optical fibers), grown with either MBE [76,107–109] or MOCVD [114]. Other groups, including our own, have isolated a 1.55 μm-emitting InAs/InP SQD. Vicinal substrate growth was demonstrated using MBE [91]. Growth by MOVPE has also produced InAs/InP SQDs [130]. An MOCVD growth, double-cap method yields SQDs and their PL has been shown to be anti-bunched [124, 125, 127]. Our CBE growth of *in situ* templates produces a high yield of isolated SQDs [146–148], and my efforts to make a TCSPC measurement will be discussed later.

4.2 Site-Selective Growth of Single Quantum Dots

The different site-selective growth techniques can be divided into two categories. The first one consists of modifications to the substrate resulting in preferred QD nucleation at particular spots. For one technique, an AFM tip creates an oxidized area within the substrate that is later removed with wet chemistry [126]. The resulting holes

are shallow but sufficient to direct the QD nucleation. This technique has already produced site-selected SQDs. The main problem with this technique is the immediate interaction between the modified region and the QD which can lead to impurities in the QD that suppress optical activity.

To limit the growth locations to a 1D array, one can grow the QDs on the edge of the sample [149, 150]. This technique is commonly known as cleaved-edge overgrowth. In essence, taking a normal QW sample, cleaving it, and putting it back in the growth chamber sideways. QDs nucleate only on the slim QW area. Again, the sample cleanliness is an issue here, even considering the fact that techniques to cleave the sample within the chamber have been developed [151].

The second category includes techniques which involve alterations to the substrate followed by further substrate addition that results in a clean area directing the QD nucleation. For one technique, a small mesa is etched into the substrate ($\sim$1 μm diameter) [152]. More substrate material is added to smooth the pillar top surface and then the SAQD is grown onto the restricted surface. This technique produces a SQD or many QDs depending on the mesa size. These isolated QDs would be hard to use for further experiments, for example those requiring a microcavity or electrostatic gates around the dot, because of the mesa shape. The IMS group has developed a similar technique that exploits the epitaxial growth process [134, 135]. This technique makes use of the different growth rates on the different crystallographic facets and will be described in the next section. The QDs produced with this technique can be embedded within a microcavity or gated with ease since its nucleation site is known.

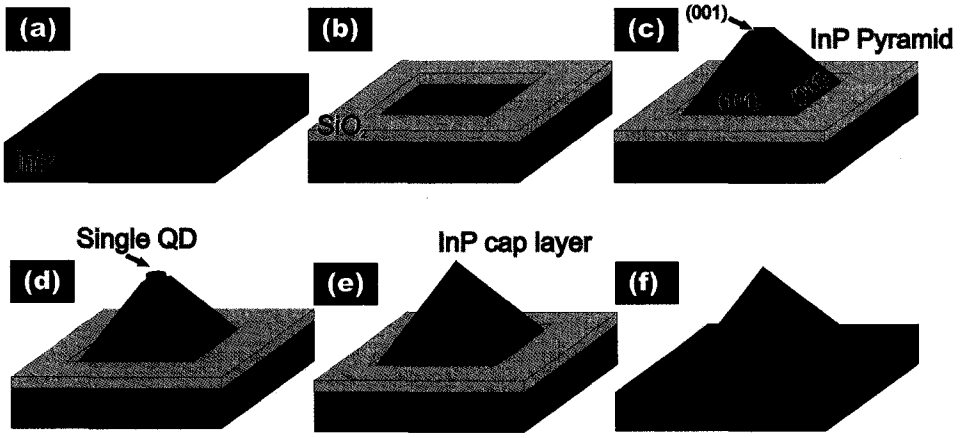

Figure 4.1: Cartoon representation of the fabrication procedure of InAs/InP site-selected SQDs. Detailed description is within the text.

The technique has subsequently been applied to InAs/GaAs QDs with good success but has not yet generated a site-selected SQD [153, 154].

4.2.1 In-situ Nanotemplate InAs/InP Single Quantum Dots

Figure 4.1 introduces the site-selective growth technique. We opened windows in a SiO_2 layer (typically 20 nm thick) deposited on an InP (001) substrate. This patterning is achieved by electron beam lithography and reactive ion etching, as shown in **(a)** and **(b)**. Contrary to MOCVD, the diffusion of deposited species from the SiO_2 layer to the exposed InP substrate is negligible. For particular directions and shapes of the windows, well-defined crystallographic facets are produced that incorporate deposited Indium at different rates. Adatoms are found to migrate away from low growth rate facets onto higher growth rate facets. A square opening with sides along the [100] and [010] axis results in InP growth only within the window. A pyramid-like shape is developed because the (100) top facet has a higher growth rate than the (111)A, (110)

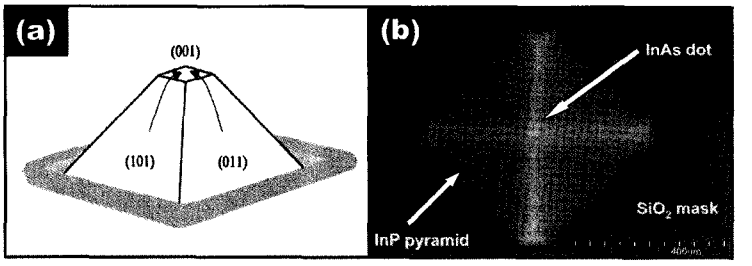

Figure 4.2: Schematics of a site-selected InP pyramid **(a)** and SEM image of an uncapped sample showing the site-selected InAs SQD on top of the InP pyramid **(b)**. From [146].

and (111)B facets under typical growth conditions. The pyramid sidewalls are (110) while the top is a (001) surface **(c)**. For growth, the sample is typically heated to 500°C and the InP growth rate is equivalent to a planar growth rate of approximately 0.5 ML/s. The actual growth rate of the nanotemplate will change depending on the size of the window opening and the degree of pyramid completion, since the flux of migrating atoms is proportional to the total area of side facets.

When the pyramid apex is roughly the size of a planar QD, we switch the growth is switched to InAs for a duration that corresponds to a sub-critical thickness for planar growth (below 2.5 ML). A 15 s growth interruption under arsenic overpressure is then used to allow the InAs to undergo the transition from 2D to 3D growth**(d)**. The migration of material to the top (001) facet leads to a thickness exceeding the critical thickness and dot nucleation occurs. Following dot growth, a cap layer of InP is grown at twice the normal, planar rate to "freeze" the QD**(e)**.

To create a sample suitable to couple with a microcavity, the pyramid needs to be planarised. To achieve this, the SiO_2 is removed **(f)** outside of the CBE system

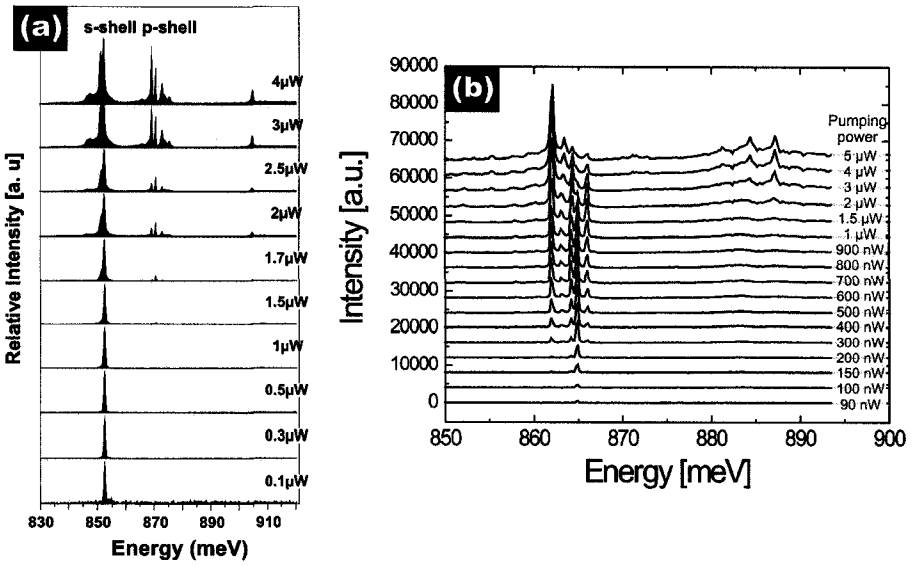

Figure 4.3: Power dependance of site-selected InAs/InP SQDs. **(a)** From [146] and **(b)** from [83]

and the sample is returned to the chamber for further InP growth. Figure 4.2**(a)** shows the various crystallographic facets of the InP pyramid and **(b)** presents an SEM image of an uncapped pyramid with a SQD at its apex.

Photoluminescence (PL) spectra as a function of pumping power for two different site-selected InAs/InP SQDs is presented in figure 4.3. As the pump power increases, more excitons populate the dot and the PL states start to fill, as expected for a SQD (artificial atom) and as observed for planar growth SQDs isolated by mesas and masks.

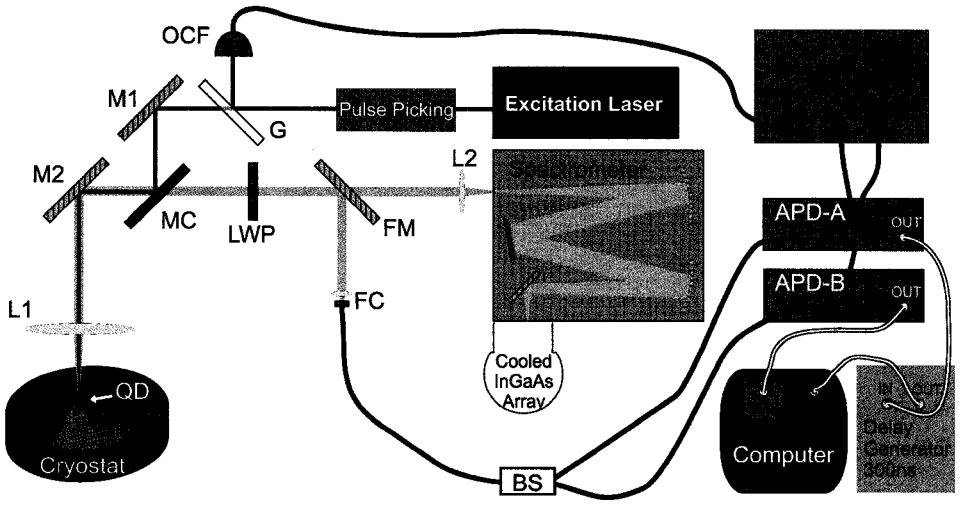

Figure 4.4: Schematics of a typical time-correlated single photon counting (TCSPC) experiment first version. See text for a detailed description of the experiment.

4.3 Single Photons from Nanotemplate InAs/InP Single Quantum Dots

Fig.4.4 shows a schematic representation of the experimental setup I used to do TCSPC measurements with our QDs using two InGaAs APDs. The first part of the setup is exactly like our PL setup (see Fig.3.9) except the excitation laser is a pulsed laser source with $\lambda \sim 830\,\text{nm}$ (Titanium Sapphire *Tsunami* from Spectra Physics) with a 82.8 MHz repetition rate pumped by a high power laser (*Millenia* from Spectra Physics, λ=532 nm). To meet the requirements of the electronics required a pulse picker (*OE360-80* from Optikon) to block 16 of very 17 pulses, reducing the repetition rate to $\approx 4.9\,\text{MHz}$. A glass slide (G) is inserted to divert a small portion of the beam to a Si fast-detector in order to provide a timing reference. We use an optical constant fraction discriminator (*OCF-401*) from Becker and Hickl which in

addition to a Si fast-diode also includes electronics to generate very precise timing information and outputs a square pulse to be used to trigger the subsequent electronics.

The undiverted part of the laser beam is reflected by a cold mirror (MC) and is focused on the sample using a microscope objective (L1). Contrary to PL measurements, we only used one type of microscope objective (Mitutoyo *100x M Plan NIR series*) because it is coated for the near infrared and has a long working distance while keeping a large collection angle. The sample PL is collected through the same objective and is transmitted through the cold mirror because of its longer wavelength whereas the sample-reflected laser light is rejected by it. To further clean the signal a long wavelength pass (LWP) filter is added. When the flip mirror (FM) is down, a lens (L2) focuses the PL into a 0.320 m spectrometer (Horiba-Jobin-Yvon *iHR320*) where it is dispersed and sent to a cooled InGaAs (Horiba-Jobin-Yvon *Symphony IGA-1024x1*). The InGaAs array provides the ability to do simple PL and when the sample is correctly characterized the flip mirror is switched.

A fiber coupler stage (FC) collects the photons into an optical fibre. The PL then crosses a 50/50 beam splitter and each half is sent to an APD. I used InGaAs APDs because our QDs emit in the NIR region of the spectrum (λ_{QD}=1.55 μm). InGaAs APDs unfortunately suffer from large dark count rates when they are biased over the break down voltage which is required to detect SP. To avoid the large dark count rate while preserving sensitivity, the detectors are operated in Geiger mode, *i.e.* they are biased over their breakdown voltage for only a short period of time ($\approx$1 ns) when the QD PL is expected to arrive. It is thus important to optimize the timing between

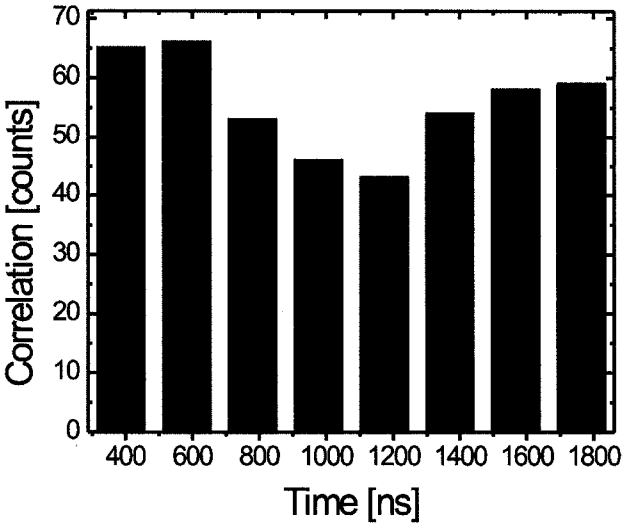

Figure 4.5: Site-selected InAs/InP SQD TCSPC curve after 6.5 hours of integration with the TCSPC setup version 1.

the PL and the detector and this is why the laser timing information from the fast detector is crucial. The synchronization is achieved using a pulse generator (Agilent Technologies *81104A*).

We used two complete APD modules from Princeton Lightwave, model *PGA-600*, that include the InGaAs APDs, the complex electronics to trigger the detector and the electronics to convert the avalanche pulse into a constant-amplitude timing pulse. The delay between the detectors is measured by a Becker and Hickl TCSPC computer board *SPC-140*. An additional delay τ_d, typically 300 ns, is added to the stop pulse for the TCSPC card to be able to measure the time difference between the two pulses.

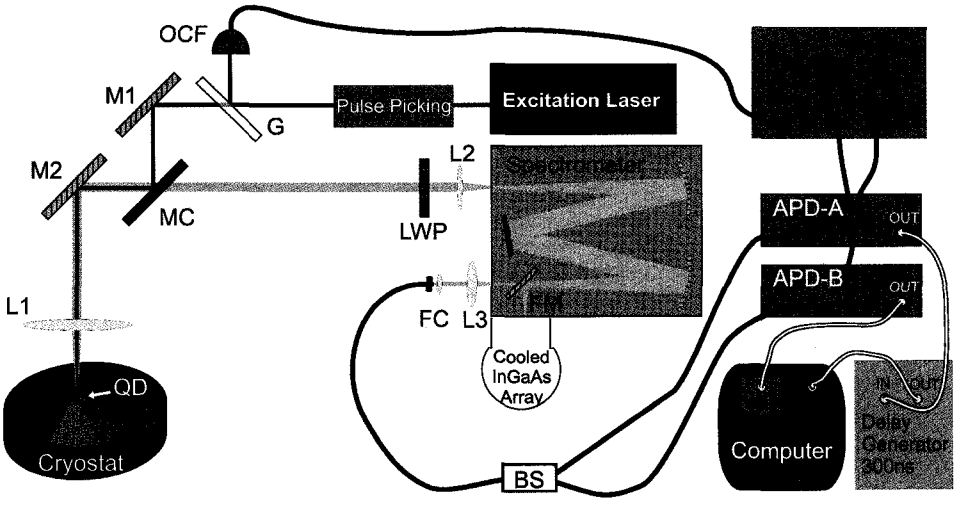

Figure 4.6: Schematics of a typical time-correlated single photon counting (TCPSC) experiment second version. See text for a detailed description of the experiment.

A typical result measured with this setup is presented in figure 4.5. In this particular experiment the PL of a site-selected InAs/InP SQD on a pyramidal template, is monitored for 6.5 hours. Unfortunately, it is not possible to conclude anything about the presence or absence of anti-bunching from this data. It is highly probable, even with the low pumping power used, that additional luminescence from the sample or even from the pump laser itself has polluted the signal. Even with the long pass filter, some small amount of pump light may reach the APDs; a single polluting photon is enough to trigger the detectors. To provide a better rejection of the unwanted photons I built a second version of the TCSPC experimental setup as shown in Fig.4.6.

This more advanced setup uses the built-in flip mirror within the spectrometer. An additional lens (L3) is inserted to collimate the center of the spectrometer output and send a narrow spectral band ($\sim$ 1 nm wide) to the fiber coupler and thus into the fiber. The spectral filtering done by the spectrometer is superior to most notch

filters in efficiency and has the added advantage that it is tunable. Unfortunately, the commercial spectrometer we purchased for this application did not exactly preserve the direction of the beam as the wavelength was tuned. The coupling within the fiber was lost even for small displacement in wavelength. Further modifications to the spectrometer were thus required but given the last year of my doctorate had been spent in trying to achieve the anti-bunching measurement, those modifications were left un-tried. Nevertheless, I believe that the modifications were definite improvements towards a successful measure.

Chapter 5

Theory: Microcavity, Micropillar and Photonic Crystal

A microcavity is a cavity like that of a laser but, because of the small cavity size, quantum effects can be observed. The recombination lifetime, τ_a, of a SQD excitonic level a will be changed when it is coupled to a microcavity mode μ. Under appropriate conditions, the linewidth can narrow and the radiative emission rate can increase. This effect is called the Purcell effect [26] and was first demonstrated by Purcell using nuclear magnetic moment transitions at radio frequencies and a resonant electric circuit as an amplification cavity. The amplitude of the effect is strongly dependant on the microcavity properties but also on the spatial and spectral overlaps between the SQD excitonic level and the microcavity mode. Moreover, the QD electric dipole orientation ($\vec{d_{qd}}$) with respect to the microcavity mode electric field $\vec{\epsilon}_\mu$ is critical. The conditions can be understood in one equation [155]:

$$\frac{{\tau_a}^{(free)}}{{\tau_a}^{(cav)}} = F_p \left[\frac{\Delta\omega_\mu}{4(\omega_a-\omega_\mu)^2+\Delta\omega_\mu}\right]\left[\frac{|\vec{\epsilon}_\mu(\vec{r_a})|^2}{|\vec{\epsilon}_\mu{}^{(max)}|^2}\right]\left[\frac{\vec{d_{qd}}\cdot\vec{\epsilon}_\mu(\vec{r_a})}{|\vec{d_{qd}}||\vec{\epsilon}_\mu(\vec{r_a})|}\right], \qquad (5.1)$$

where F_p is the Purcell factor, ω_a and ω_μ represent respectively the frequency of the QD excitonic level and the microcavity mode and $\Delta\omega_\mu = \omega_a - \omega_\mu$. The details of the physics behind the Purcell factor will be further explained in section 5.2.1. In effect,

Key Parameters	Description
(i)	Strength of the Purcell effect.
(ii)	The spatial overlap between the SQD and field antinode.
(iii)	The spectral overlap between the SQD and mode energy.
(iv)	Orientation of the QD electric dipole.
(v)	The far-field radiation pattern.

Table 5.1: Key parameters that must be considered when designing a SP source based on a coupled SQD-microcavity system.

the coupled system optical DOS becomes the product of the QD optical DOS and the microcavity optical DOS. The second factor of equation (5.1) refers to the spectral overlap of the dot and cavity, whilst the third factor refers to the spatial overlap. The last factor is linked with the QD electric dipole orientation with respect to the microcavity mode electric field. Because of the disc-like shape of most QDs used in such experiments, this term is usually close to 1.

From equation (5.1), the conditions required to create an efficient SP source based on a coupled SQD-microcavity system can determined. Five key parameters that must be considered are presented in table 5.1. The last parameter, the far field radiation pattern, is as crucial as the others, although it does not influence the radiative lifetime. The far-field needs to be coupled efficiently to an optical communication channel if one wishes to collect photons in an efficient manner. A review of the different experimental results in our laboratories and in other groups will be presented in chapters 7 and 8.

The first three sections of this chapter describe the various regimes of coupling between the QD and the microcavity, and the effects of those different regimes on the

photoluminescence (PL) of the system. Sections 5.5, 5.6 and 5.7 introduce the concepts behind the two different types of microcavities used in this thesis work, namely the micropillar and the photonic crystal (PhC) microcavity. Techniques to model theoretically the microcavity properties will also be introduced.

5.1 Cavity Coupling Regimes

The content of this section follows the discussion by Gérard in a chapter of the book by Michler *et al.* [142]. We consider the coupling between a QD at low temperature and undefined cavity modes ($\mu = 1, 2, 3...$). Let us define Ω_μ, the interaction frequency for mode μ, (also known as the Rabi frequency) as the overlap between the QD dipole moment and the electric field of the mode μ at the position $\vec{r}$, divided by $\hbar$:

$$\Omega_\mu := \frac{|\vec{d}_{qd} \cdot \vec{E}_\mu(\vec{r})|}{\hbar}. \tag{5.2}$$

Ω_μ characterizes the degree of coupling between the QD and the mode. To make this connection more obvious, we express the electric field in terms of the normalized mode spatial function ($\vec{\alpha}_\mu(\vec{r})$) and the mode frequency (ω_μ):

$$\vec{E}_\mu(\vec{r}) = \left(\frac{\hbar\omega_\mu}{2\varepsilon_r\varepsilon_0}\right)^{1/2} \vec{\alpha}_\mu(\vec{r}), \tag{5.3}$$

where ε_r (ε_0) is the material (vacuum) permittivity. $\vec{\alpha}_\mu(\vec{r})$ is a complex vector which describes the local field polarization and relative field amplitude and it is normalized so that its norm is unity at the antinode of the electric field. If we assume the polarization of the QD electric dipole is the same as that of the electric field of the mode and consider only one mode μ of the cavity with a frequency equal to that of

the QD excitonic level a ($\omega_\mu = \omega_a = \omega$), then inserting equation (5.3) in (5.2) gives:

$$\Omega_\mu = \frac{d_{qd}}{\hbar}\left(\frac{\hbar\omega}{2\varepsilon_r\varepsilon_0}\right)^{1/2}|\vec{\alpha}_\mu(\vec{r})|. \tag{5.4}$$

The effective mode volume (V_μ) is defined as:

$$V_{eff} = \frac{1}{n^2_{\mu,max}}\int\int\int_{\vec{r}} n^2_\mu(\vec{r})\vec{\alpha}_\mu(\vec{r})d^3\vec{r}, \tag{5.5}$$

where $n_{\mu,max}$ is the refractive index at the field maximum. If one considers the QD is located at the cavity electric field maxima Eq.(5.5) can be approximated to by:

$$|\vec{\alpha}_\mu(\vec{r})|^2_{max} = V_\mu^{-1}. \tag{5.6}$$

The QD oscillator strength is given by:

$$f = \frac{2m\omega d^2_{qd}}{q^2\hbar}, \tag{5.7}$$

where m is the effective mass and q the electronic charge. We can then rewrite (5.4) as:

$$\Omega_\mu = \left(\frac{q^2}{4m\varepsilon_r\varepsilon_0}\frac{f}{V_\mu}\right)^{1/2}. \tag{5.8}$$

A system composed of a QD coupled to a cavity mode can be in the weak or strong coupling regime or an intermediate regime referred to as the "bad-cavity" regime [156]. We will not discuss here the particularity of this regime. The parameter Ω_μ compared with the cavity mode linewidth (Γ_μ) and the QD excitonic level linewidth (Γ_a) determines which regime applies. Since we aim at the construction of a single photon source, the important thing is to avoid the strong coupling regime, where the emission rate is no longer improved by the presence of the microcavity. The coupled system is in the strong coupling regime when $\Omega_\mu > |\Gamma_a - \Gamma_\mu|/4$. The

derivation of this limit can be found in [142].

The following sections explore the coupled QD-microcavity system PL in the strong and weak coupling regimes. After their origins are more clearly defined, section 5.4 discusses these limits with respect to our InAs/InP QDs.

5.2 Weak Coupling Regime

The interaction between a QD at low temperature and a microcavity produces some interesting consequences. The effect is the same as that first described by Purcell in his famous 1946 paper [26] on nuclear magnetic moment transitions at radio frequencies coupled to an electronic circuit. The emitted photons of the QD that match a microcavity mode can have a shorter lifetime and a higher recombination rate, because of the coupling [155, 157, 158].

5.2.1 Purcell Effect

The ratio of the QD emission rate in the cavity mode μ ($\gamma^{(\mu)}$) over the QD emission rate in the vacuum ($\gamma^{(0)}$) is defined as the Purcell factor ($F_p^{(\mu)}$) given by [157]:

$$F_p^{(\mu)} = \frac{\gamma^{(\mu)}}{\gamma^{(0)}} = \frac{3\lambda_\mu^3}{4\pi^2}\frac{Q_\mu}{V_\mu}, \tag{5.9}$$

where Q_μ is the mode quality factor and is defined as the ratio of the mode frequency over the mode linewidth:

$$Q_\mu = \frac{\omega_\mu}{\Gamma_\mu}. \tag{5.10}$$

A smaller linewidth results in a higher Q while a smaller mode volume corresponds to a higher Purcell factor. Equation (5.9) is valid only when the system is in the weak coupling regime. Using Eq.(5.10) and Eq.(5.4) and the definitions for the different regime boundaries expressed in the previous section, we see that if $Q_\mu V_\mu^{-1/2}$ gets too high, the system is no longer in the weak coupling regime. The weak coupling regime is usually achieved when $\Omega_\mu < \Gamma_\mu$, *i.e.* $\frac{Q_\mu}{\sqrt{V_\mu}} < \frac{4\omega_\mu m\varepsilon_0}{q^2 f}$, because $\Gamma_a < \Gamma_\mu$ is the common case.

The Purcell effect can be derived from both classical and quantum mechanics. Since we will need to use the quantum mechanical approach in further sections of this thesis we will only present here the quantum mechanical derivation of the Purcell factor. The classical derivation can be found in references [26, 157].

5.2.2 Derivation of the Purcell Factor

Consider a system of many particles coupled to a laser cavity with many modes (see Fig.5.1). Because of the "artificial" atom nature of the QD the whole derivation below is still valid for QD in a microcavity. Here, the many different particles refer to the different QD energy levels. The charge, position, momentum and mass of each particle (β) are given by q_β, $\vec{r}_\beta$, p_β and m_β, respectively. The total Hamiltonian of the system is given by:

$$H = \sum_\beta m_\beta c^2 + \sum_\beta \frac{1}{2m_\beta}\left[\vec{p}_\beta - q_\beta \vec{A}(\vec{r}_\beta)\right]^2 + {}^{(L)}H^{(cav)} + {}^{(T)}H, \qquad (5.11)$$

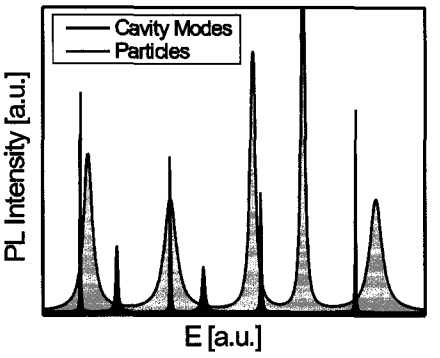

Figure 5.1: PL intensity for a cavity with many modes excited by an embedded broadband source (black line) and PL intensity for many particles recombination lines (red line).

where $\vec{A}(\vec{r}_\beta)$ is the particle β magnetic potential. The first two terms are the rest and kinetic energies of individual particles and the two others are the cavity longitudinal field energy ($^{(L)}H^{(cav)}$) and the transverse field energy ($^{(T)}H$). The field terms can be expressed as:

$$^{(L)}H^{(cav)} = \frac{\varepsilon_0}{2}\int {}^{(L)}\vec{E}^{(cav)}(\vec{r}_\beta,\vec{r})d^3\vec{r}, \tag{5.12}$$

$$^{(T)}H = \frac{\varepsilon_0}{2}\int \left([{}^{(T)}\vec{E}(\vec{r})]^2 + c^2[{}^{(T)}\vec{B}(\vec{r})]^2\right) d^3\vec{r}, \tag{5.13}$$

where $^{(L)}\vec{E}^{(cav)}$ is the longitudinal electric field of the cavity and $^{(T)}\vec{E}$ and $^{(T)}\vec{B}$ are the transverse electric and magnetic field respectively. Equation (5.13) can be re-written using the second quantization language (using a_μ and $a_\mu^\dagger$ as annihilation and creation operators for mode μ):

$$^{(T)}H = \sum_\mu \hbar\omega_\mu(a_\mu^\dagger a_\mu + 1/2). \tag{5.14}$$

In the absence of a cavity $^{(L)}H^{(cav)}$ becomes $^{(L)}H^{(0)}$ and is defined by the summation of the particles electrostatic potentials and an electrostatic re-normalization of

the particles rest masses:

$$^{(L)}H^{(0)} = V_{coul}(\vec{r}_\beta) + \sum_\beta \delta m_\beta c^2, \tag{5.15}$$

where:

$$V_{coul}(\vec{r}_\beta) = \frac{1}{4\pi\varepsilon_0}\sum_{\zeta\neq\beta}\frac{q_\zeta q_\beta}{|\vec{r}_\zeta - \vec{r}_\beta|}, \tag{5.16}$$

$$\delta m_\beta = \frac{1}{32c^2\pi^2\varepsilon_0}\int \frac{q_\beta^2}{|\vec{r} - \vec{r}_\beta|}d\vec{r}. \tag{5.17}$$

We can re-write the Hamiltonian of the system (equation (5.11)) as:

$$H = H_p + {}^{(L)}H^{(r)} + {}^{(T)}H + H_I + H_{II}. \tag{5.18}$$

If we consider the following simplifications:

$$H_p = \sum_\beta (m_\beta + \delta m_\beta)c^2 + \sum_\beta \left(\frac{p_\beta^2}{2m_\beta} + V_{coul}(\vec{r}_\beta)\right), \tag{5.19}$$

$$^{(L)}H^{(r)}(\vec{r}_\beta) = {}^{(L)}H^{(cav)}(\vec{r}_\beta) - {}^{(L)}H^{(0)}(\vec{r}_\beta), \tag{5.20}$$

$$H_I = -\sum_\beta \frac{q_\beta}{m_\beta}\vec{p}_\beta \cdot \vec{A}(\vec{r}_\beta), \tag{5.21}$$

$$H_{II} = \sum_\beta \frac{q_\beta^2}{2m_\beta}\vec{A}^2(\vec{r}_\beta). \tag{5.22}$$

The Hamiltonians H_I and H_{II} describe the coupling between the transverse cavity fields and the particles. They will vary with the cavity geometry and the particle properties. Consider now that we only have one particle and make the electric dipole approximation to substitute the dipole position by the particle center of mass position. This means: $\vec{r}_\beta \to \vec{R}$, $q_\beta \to q$, $m_\beta \to m$, and $\vec{p}_\beta \to \vec{p}$. Equation (5.19) to (5.22) are

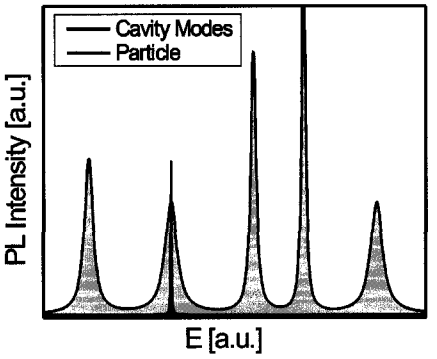

Figure 5.2: PL intensity for a cavity with many modes excited by an embedded broadband source (black line) and PL intensity for a particle recombination line (red line).

simplified and (5.18) becomes:

$$H = (m+\delta m)c^2 + \frac{p^2}{2m} + V_{coul}(\vec{r}) + \sum_{\mu} \hbar\omega_\mu (a_\mu^\dagger a_\mu + 1/2) + {}^{(L)}H^{(r)}(\vec{R}) - \frac{q}{m}\vec{p}\cdot\vec{A}(\vec{R}) + \frac{q^2}{2m}\vec{A}^2(\vec{R}), \quad (5.23)$$

where the sixth term ($H_I = \frac{q}{m}\vec{p}\cdot\vec{A}(\vec{R})$) is the term describing the spontaneous emission of the system. Figure 5.2 presents a cartoon to contrast the single particle PL with the microcavity PL. The black curve shows the typical cavity modal structure excited by an embedded broadband source whereas the red curve represents PL intensity coming from a single particle.

The basis of the particle states $|\rangle_p$ is defined as:

$$H_p|a\rangle_p = \hbar\omega_a|a\rangle_p \quad (5.24)$$

$$H_p|j\rangle_p = \hbar\omega_j|j\rangle_p \quad (5.25)$$

where $\omega_{a \text{ or } j}$ is the frequency of the particle state a (or j). Let us consider for now that $\omega_j < \omega_a$. The basis of the microcavity-particle system can be written as: $|0, 0_\mu\rangle$ where the first number in the ket refers to the state of the particle and the second to the number of photons in the mode μ. For example, the emission of a photon involves the transition of the particle from state a to state j and the photon is emitted in to the mode μ : $|a, \text{vacuum}\rangle \rightarrow |j, 1_\mu\rangle$. The density of photons at ω is given by:

$$\rho^{(cav)}(\omega) = \sum_\mu \delta_{\Gamma_\mu}(\omega - \omega_\mu), \tag{5.26}$$

where $\delta_{\Gamma_\mu}(\omega - \omega_\mu)$ is a normalized Lorentz function centered around ω_μ defined as:

$$\delta_{\Gamma_\mu}(\omega - \omega_\mu) = \frac{1}{\pi} \frac{\Gamma_\mu/2}{(\omega - \omega_\mu)^2 + (\Gamma_\mu/2)^2}. \tag{5.27}$$

If the cavity Q is moderate (*i.e.* we are in the weak coupling regime), the emission process is irreversible. This means that the decay rate of the coupled particle-cavity system is directly related to $\rho^{(cav)}(\omega_{aj})$ where $\omega_{aj} = \omega_a - \omega_j$.

Using Fermi's Golden rule, the total decay rate from level a to j is:

$$\gamma_{a \rightarrow j}^{(cav)} = \frac{2\pi}{\hbar^2} \sum_\mu |\langle a, 0|H_I|j, 1_\mu\rangle|^2 \, \delta_{\Gamma_\mu}(\omega_{aj} - \omega_\mu) \tag{5.28}$$

In the second quantization language, the cavity magnetic potential is expressed as:

$$\vec{A} = \sum_\mu A_\mu \left[a_\mu \vec{\alpha}_\mu(\vec{r}) + a_\mu^\dagger \vec{\alpha}_\mu^*(\vec{r}) \right], \tag{5.29}$$

where, $A_\mu = \left(\frac{\hbar}{2\varepsilon_0 \omega_\mu}\right)^{1/2}$, a_μ and $a_\mu^\dagger$ are the mode μ annihilation and creation operator, respectively, and $\vec{\alpha}_\mu$ is the normalized mode spatial functions.

Approximating that the ω_μ in H_I becomes ω_{aj} because of the δ-like nature of δ_{Γ_μ}, we can then rewrite (5.28) as:

$$\gamma_{a\to j}^{(cav)} = \frac{\pi}{\hbar\varepsilon_0}\frac{q^2}{m^2}\frac{1}{\omega_{aj}}\sum_\mu |\vec{p}_{aj}\cdot\vec{\alpha}_\mu(\vec{R})|^2\delta_{\Gamma_\mu}(\omega_{aj}-\omega) \tag{5.30}$$

The operator $\vec{p}$ is related to the particle Hamiltonian (H_p) and the position operator $\vec{r}$ by: $\vec{p} = -(im/\hbar)[\vec{r}, H_p]$ and the particle dipole operator is given by: $\vec{D} = q\vec{r}$, therefore $q\vec{p}_{aj} = -(im\omega_{aj})\vec{D}_{aj}$. The spontaneous emission rate becomes:

$$\gamma_{a\to j}^{(cav)} = \frac{\pi}{\hbar\varepsilon_0}\omega_{aj}\sum_\mu |\vec{D}_{aj}\cdot\vec{\alpha}_\mu(\vec{R})|^2\delta_{\Gamma_\mu}(\omega_{aj}-\omega). \tag{5.31}$$

Assuming that only one mode couples with the particle (since $\Gamma_{aj} < \Gamma_\mu$), that $\omega_{aj} = \omega_\mu$ and that the particle emission and the cavity mode have the same polarization, equation (5.31) becomes:

$$\gamma_{a\to j}^{(cav)} = \frac{2}{\hbar\varepsilon_0}\frac{\omega_\mu}{\Gamma_\mu}|\vec{D}_{aj}|^2|\vec{\alpha}_\mu(\vec{R})|^2. \tag{5.32}$$

Remembering equations (5.6) and (5.10) we can write:

$$\gamma_{a\to j}^{(cav)} = \frac{2}{\hbar\varepsilon_0}\frac{Q_\mu|\vec{D}_{aj}|^2}{V_\mu}. \tag{5.33}$$

If there is no cavity, the summation in equation (5.31) becomes an integral and simplifies to:

$$\gamma_{a\to j}^{(0)} = \frac{\omega_{aj}^3|\vec{D}_{aj}|^2}{3\pi\varepsilon_0\hbar c^3}. \tag{5.34}$$

The division of Eq.(5.33) by Eq.(5.34) gives us the Purcell factor:

$$F_p = \frac{\gamma_{a\to j}^{(cav)}}{\gamma_{a\to j}^{(0)}} = \frac{3\lambda_\mu^3}{4\pi^2}\frac{Q_\mu}{V_\mu}. \tag{5.35}$$

The particle emission rate is improved greatly by the presence of the cavity. The demonstration presented here was for a general particle inside a general cavity. It

also applies to a QD in a microcavity since, as was shown in chapter 3 and 4, a QD is an artificial atom and a microcavity is simply a "small" cavity. It is important to note that Eq.(5.35) stops being valid when we move away from the weak coupling regime, *i.e.* $\frac{3\lambda_\mu^3}{4\pi^2}\frac{Q_\mu}{V_\mu}$ is no longer equal to the ratio of the spontaneous emission rates. In the next section we will examine the situation where the cavity Q is much higher – the strong coupling regime. The microcavity-QD emission properties are quite different in such a situation.

5.3 Strong Coupling Regime

The strong coupling regime is reached not only when the cavity Q_μ is large but when the $Q_\mu V_\mu^{-1/2}$ is large enough (see section 5.1 for more details). An interesting effect of the strong coupling regime is the splitting of the PL peaks in two as the coupling becomes stronger.

5.3.1 Vacuum Rabbi Splitting

We will use the dressed atom-cavity system approach. Details of the derivation can be found in references [2, 157–159]. The atom used here is simply a two-energy level system and can be directly replaced by the single exciton level of a QD at low temperature. The dressed atom-cavity approach is illustrated in the schematic of figure 5.3. The system consists of three Hamiltonians: one for the atom (H_A), one for the cavity quantum field (H_F) and one for the interaction between the atom and the

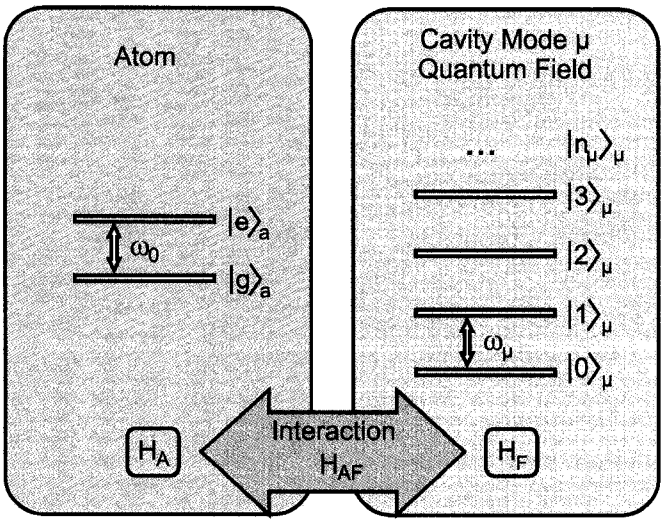

Figure 5.3: Schematics of the dressed atom-cavity system.

cavity (H_{AF}), given by:

$$H = H_A + H_{AF} + H_F, \tag{5.36}$$

Considering the atomic operator $\sigma_3 = \frac{1}{\sqrt{2}}(|e\rangle\langle e| - |g\rangle\langle g|)$ and $\sigma_+ = \sigma_-^\dagger = |e\rangle\langle g|$ plus the usual photon annihilation and creation in the cavity mode μ (a_μ and $a_\mu^\dagger$), we have:

$$H_A = \hbar\omega_0\sigma_3, \tag{5.37}$$

$$H_F = \hbar\omega_\mu[a^\dagger{}_\mu a_\mu + 1/2], \tag{5.38}$$

$$H_{AF} = i\hbar\Omega[\sigma_- a_\mu^\dagger - \sigma_+ a_\mu]. \tag{5.39}$$

As a basis to the system hamiltonian, one can use:

$$|\overline{+, n_\mu}\rangle = \cos\theta_n|e, n_\mu\rangle + \sin\theta_n|g, n_\mu + 1\rangle, \tag{5.40}$$

$$|\overline{-, n_\mu}\rangle = -\sin\theta_n|e, n_\mu\rangle + \cos\theta_n|g, n_\mu + 1\rangle, \tag{5.41}$$

where n_μ is the number of photons in mode μ and the coupling angle θ_{n_μ} is defined

by:

$$\tan(2\theta_{n_\mu}) = \frac{2\Omega_\mu\sqrt{n_\mu+1}}{\omega_0-\omega_\mu} \quad (0 \leqslant \theta_{n_\mu} < \pi/2). \tag{5.42}$$

The system Hamiltonian results in the energy levels with this basis:

$$E_{g0} = -\frac{\hbar}{2}(\omega_0-\omega_\mu), \tag{5.43}$$

$$E_{\overline{\pm,n_\mu}} = (n_\mu+1)\hbar\omega_\mu \pm \frac{\hbar}{2}\sqrt{4\Omega_\mu^2(n_\mu+1)+(\omega_0-\omega_\mu)^2}. \tag{5.44}$$

The splitting of the energy levels due to the strong coupling effect Δ_{n_μ} is given by $(E_{\overline{+,n_\mu}} - E_{\overline{-,n_\mu}})/\hbar = \Delta_{n_\mu}$. The splitting is caused by an exchange of the excitation between the atom and the quantum field. A way to test the strong coupling regime is simply by gradually tuning ω_0 with respect to ω_μ, changing the value of Δ_{n_μ}.

If we consider the case were the atom and cavity frequency are exactly the same we get $\omega_0 = \omega_\mu = \omega$, $\Omega_\mu = \Omega$, $\theta_{n_\mu} = \pi/4$ and:

$$|\overline{+,n_\mu}\rangle = 1/\sqrt{2}(|e,n_\mu\rangle + |g,n_\mu+1\rangle), \tag{5.45}$$

$$|\overline{-,n_\mu}\rangle = 1/\sqrt{2}(-|e,n_\mu\rangle + |g,n_\mu+1\rangle). \tag{5.46}$$

Hence:

$$E_{g0} = 0, \tag{5.47}$$

$$E_{\overline{\pm,n_\mu}} = (n_\mu+1)\hbar\omega \pm \hbar\Omega\sqrt{(n_\mu+1)}. \tag{5.48}$$

Figure 5.4 presents a comparison of the cavity quantum field energy levels (green) with the energy levels of the dressed atom-cavity system (black). By changing the cavity mode volume V_μ hence Ω_μ, the splitting of the $|\overline{\pm,n_\mu}\rangle$ energy levels will vary.

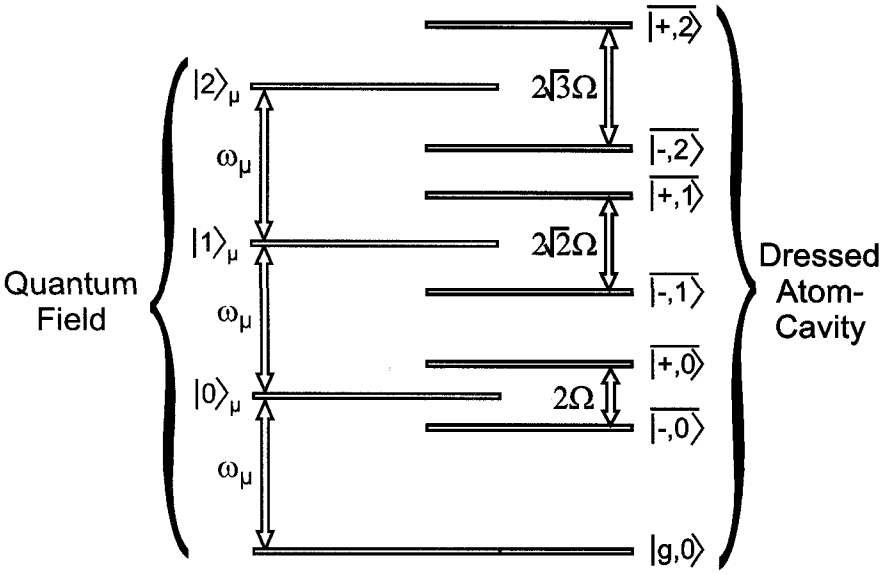

Figure 5.4: Comparison of the energy levels between the cavity quantum field (green) and the dressed atom-cavity system when $\omega_0 = \omega_\mu$ (black)

In references [158,159], the authors show that the atom-cavity system PL is given by:

$$2\pi S(\omega) = \frac{\frac{1}{2}(\Gamma_\mu + \Gamma_a)}{\frac{1}{4}(\Gamma_\mu + \Gamma_a)^2 + (\omega - \omega_0 - \Omega)^2} + \frac{\frac{1}{2}(\Gamma_\mu + \Gamma_a)}{\frac{1}{4}(\Gamma_\mu + \Gamma_a)^2 + (\omega - \omega_0 + \Omega)^2}, \quad (5.49)$$

where, Γ_a and Γ_μ are the atom and cavity linewidths of the peaks where $S(\omega)$ is the normalized spontaneous emission spectrum. A typical curve representing the Rabi splitting using equation 5.49 is shown in figure 5.5.

5.4 The Coupling Regimes with Numbers

Before we move on to the details of microcavity design and fabrication, this section examines the different coupling regime limits in greater detail. Using equation (5.10)

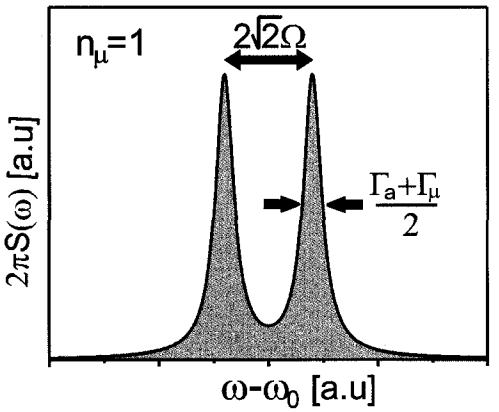

Figure 5.5: Typical Rabi splitting curve.

and rewriting (5.2) as $\Omega_\mu = \nu_{qd}\frac{\omega^{1/2}}{V_\mu^{1/2}}$, the strong coupling limit can be expressed in terms of the microcavity quality factor, mode volume, mode frequency and a constant $(\nu_{qd} = \left(\frac{d_{qd}^2}{2\hbar\varepsilon_R\varepsilon_0}\right))$ as:

$$\frac{Q_\mu}{\sqrt{V_\mu}} = \frac{\omega_\mu}{\nu_{qd}}. \tag{5.50}$$

The single exciton dipole moment for QDs (d_{qd}) is proportional to the s-shell electron and hole wavefunction overlap. Calculations carried out within the IMS predict a single exciton dipole moment of $\approx$ 105 Debye, which is somewhat higher than that found for InAs/GaAs QDs [160]. The larger transition dipole moment can be explained by the larger size of InAs/InP QDs. The relative permittivity of the InAs/InP QD is approximated as that of InAs: ε_R=12.3. For a typical InAs/InP QD the single exciton linewidth (Γ_a) is given by the PL-measured peak linewidth

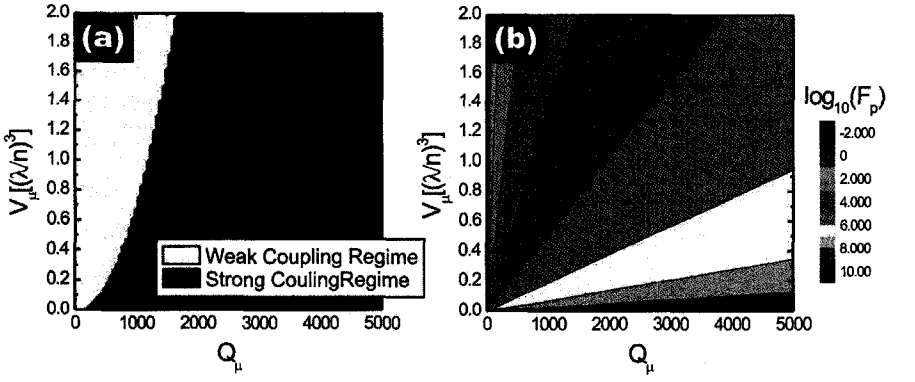

Figure 5.6: Contour plot of the microcavity-QD coupling regimes **(a)** and Purcell factor (F_p) **(b)** as a function of the microcavity Q_μ and V_μ for typical InAs/InP QD parameters.

($^{(PL)}\Gamma_a \approx 250\,\mu$eV) divided by the InP permittivity ($\varepsilon_{InP} = 12.4$) because of electrostatic effects induced by the material surrounding the QD [161]. The photon energy is ≈800 meV, *i.e.* 1550 nm wavelength. This leaves only the microcavity mode parameters (Q_μ and V_μ) to determine the coupling regime.

An important thing to keep in mind is that the derivation of the Rabi frequency equation assumed a perfect spectral and spatial overlap between the QD and the microcavity. There is no doubt that these overlaps will never be perfect and that this will affect the system behavior and resulting coupling regime. Figure 5.6 **(a)** presents the different regimes as a function of Q_μ and V_μ in a contour plot where yellow areas represents the weak coupling regime, and green the strong coupling regime. In order to fabricate an efficient single photon source, we have to avoid the strong coupling regime.

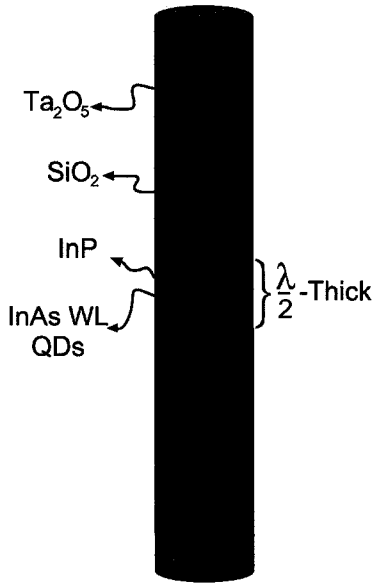

Figure 5.7: Schematical representation of a micropillar microcavity.

Again, these numbers are to be used with caution since the limit is not as clear cut as presented in the figure and ideal spectral and spatial overlaps are assumed. Figure 5.6 **(b)** shows the corresponding Purcell factor as a contour plot for the same Q_μ and V_μ values using equation (5.9).

5.5 Micropillars

A cartoon representation of a micropillar microcavity is shown in figure 5.7. It consists of a central layer containing the QDs (InAs/InP in our case). The central layer thickness (L) between two ideal mirrors is related to the mode wavelength (λ_μ) by:

$$\lambda_\mu = 2n_\mu^{eff} L, \tag{5.51}$$

where n_{μ}^{eff} is the mode μ effective refractive index of a cylinder of radii ρ surrounded by air. The subscript μ , as will be more clearly defined later, refers to indices l and m related with the modal solution to a cylinder waveguide. Each mode has its own transverse distribution of the electromagnetic field. The attraction of micropillar microcavities comes from their straightforward design and operation as opposed to photonic crystal (PhC) microcavities and microdisc microcavities. Dielectric stacks are quite commonly used in our everyday life: in fabricating holograms on dollar bills and credit cards, or anti-reflection coatings on our glasses etc. The step from a dielectric stack to a micropillar requires one to etch through the mirrors to create a circular column of a few microns diameter. As will be explained in the experimental section, this step is the critical and most difficult one.

5.5.1 Distributed Bragg Grating

For our samples, twelve pairs of SiO_2/Ta_2O_5 layers are inserted to create the top and bottom distributed Bragg reflector (DBR) [162–164]. Basically, the alternation of materials with differing index (n_{SiO_2}=1.5 and $n_{Ta_2O_5}$=2.1) and thickness of a quarter of wavelength in the material creates a good broadband mirror through interference effects, as in a Bragg grating. In our case a light source is embedded between the two DBR mirrors and, provided each mirror consists of a large number of pairs, each one can be approximated by an ideal mirror, thus validating the assumption made in Eq.5.51.

5.5.2 Solving the Micropillar Modes

The equation (5.51) will give the solution to the micropillar modes if one assumes that the mode profile is preserved from one dielectric disc to the next. The modes of a cylinder can be solved with standard techniques for a step-index circular waveguide [165]. The results are modes labeled $\mathrm{EH}_{(l,m)}$ and $\mathrm{HE}_{(l,m)}$, with a mode effective index determined by the solution of complex equations for the EH and HE modes respectively [165]:

$$\frac{J_{l+1}(\rho_a)}{\rho_a J_l(\rho_a)} = \frac{n_c^2 + n_{air}^2}{2n_c^2}\frac{K_l'(\rho_c)}{\rho_c K_l(\rho_c)} + \left(\frac{l}{\rho_a^2} - R\right), \tag{5.52}$$

$$\frac{J_{l-1}(\rho_a)}{\rho_a J_l(\rho_a)} = -\left(\frac{n_c^2 + n_{air}^2}{2n_c^2}\right)\frac{K_l'(\rho_c)}{\rho_c K_l(\rho_c)} + \left(\frac{l}{\rho_a^2} - R\right), \tag{5.53}$$

where:

$$R = \left[\left(\frac{n_c^2 - n_{air}^2}{2n_c^2}\right)\left(\frac{K_l'(\rho_c)}{\rho_c K_l(\rho_c)}\right)^2 + \left(\frac{l\beta_{(l,m)}}{n_c k_o}\right)^2\left(\frac{1}{\rho_c^2} + \frac{1}{\rho_a^2}\right)^2\right]^{1/2}, \tag{5.54}$$

$$\rho_a = \rho\sqrt{n_c^2 k_0^2 - \beta_{(l,m)}}, \tag{5.55}$$

$$\rho_c = \rho\sqrt{\beta_{(l,m)} - n_{air}^2 k_0^2}, \tag{5.56}$$

while $J_l(\rho)$ and $K_l(\rho)$ are l^{th} order first kind Bessel and second kind modified Bessel functions, respectively. The mode propagation constant is given by the product of the mode effective index and the vacuum wavenumber ($\beta_{(l,m)} = n_{(l,m)}k_0$) while n_c and n_a are the refractive index of the material composing the cylinder and the surrounding medium (air). It is obvious that $n_{(l,m)}$ is higher than n_a but lower than n_c thus avoiding problems with equations (5.55) and (5.56).

Now that we have the modal solutions of each individual disc, we can couple them with the optical DOS allowed by the DBR. The central layer can be viewed as a

"defect" in the periodic DBR. The defect results in the creation of a propagating mode within the structure's photonic bandgap with wavelength given by (5.51). The concept of a photonic bandgap will be further discussed in the next section. The output of mode (l, m) of the micropillar are given by two sets of equations [165]. One describes the electric field within the micropillar:

$$E_r = \frac{-i\beta_{(l,m)}\rho^2}{\rho_a^2}\left[C_A\frac{\rho_a}{\rho}J_l'(\rho_{ar}) + C_B\frac{i\omega\mu_0 l}{\beta_{(l,m)}r}J_l(\rho_{ar})\right]\exp(i(\omega t + l\phi - \beta_{(l,m)}z)), \quad (5.57)$$

$$E_\phi = \frac{-i\beta_{(l,m)}\rho^2}{\rho_a^2}\left[C_A\frac{il}{r}J_l'(\rho_{ar}) - C_B\frac{\rho_a\omega\mu_0}{\rho\beta_{(l,m)}}J_l(\rho_{ar})\right]\exp(i(\omega t + l\phi - \beta_{(l,m)}z)), \quad (5.58)$$

$$E_z = C_A J_l(\rho_{ar})\exp(i(\omega t + l\phi - \beta_{(l,m)}z)), \quad (5.59)$$

$$H_r = \frac{-i\beta_{(l,m)}\rho^2}{\rho_a^2}\left[C_B\frac{\rho_a}{\rho}J_l'(\rho_{ar}) - C_A\frac{i\omega\varepsilon_0 n_{(l,m)}^2 l}{\beta_{(l,m)}r}J_l(\rho_{ar})\right]\exp(i(\omega t + l\phi - \beta_{(l,m)}z)), \quad (5.60)$$

$$H_\phi = \frac{-i\beta_{(l,m)}\rho^2}{\rho_a^2}\left[C_B\frac{il}{r}J_l(\rho_{ar}) + C_A\frac{i\omega\varepsilon_0 n_{(l,m)}^2\rho_a}{\beta_{(l,m)}\rho}J_l'(\rho_{ar})\right]\exp(i(\omega t + l\phi - \beta_{(l,m)}z)), \quad (5.61)$$

$$H_z = C_B J_l(\rho_{ar})\exp(i(\omega t + l\phi - \beta_{(l,m)}z)), \quad (5.62)$$

where ρ_{ar} is defined as $\rho_{ar} = \rho_a r/\rho$. The second equation set describes the field outside the micropillar:

$$E_r = \frac{i\beta_{(l,m)}\rho^2}{\rho_c^2}\left[C_C\frac{\rho_c}{\rho}K_l'(\rho_{cr}) + C_D\frac{i\omega\mu_0 l}{\beta_{(l,m)}r}K_l(\rho_{cr})\right]\exp(i(\omega t + l\phi - \beta_{(l,m)}z)), \quad (5.63)$$

$$E_\phi = \frac{i\beta_{(l,m)}\rho^2}{\rho_c^2}\left[C_C\frac{il}{r}K_l(\rho_{cr}) + C_D\frac{\omega\mu_0\rho_c}{\beta_{(l,m)}\rho}K_l(\rho_{cr})\right]\exp(i(\omega t + l\phi - \beta_{(l,m)}z)), \quad (5.64)$$

$$E_z = C_C K_l(\rho_{cr}) \exp(i(\omega t + l\phi - \beta_{(l,m)} z)), \tag{5.65}$$

$$H_r = \frac{i\beta_{(l,m)}\rho^2}{\rho_c^2}\left[C_D \frac{\rho_c}{\rho} K_l'(\rho_{cr}) + C_C \frac{i\omega\varepsilon_0 l}{\beta_{(l,m)} r} K_l(\rho_{cr})\right] \exp(i(\omega t + l\phi - \beta_{(l,m)} z)), \tag{5.66}$$

$$H_\phi = \frac{i\beta_{(l,m)}\rho^2}{\rho_c^2}\left[C_D \frac{il}{r} K_l(\rho_{cr}) + C_C \frac{\omega\varepsilon_0\rho_c}{\beta_{(l,m)}\rho} K_l'(\rho_{cr})\right] \exp(i(\omega t + l\phi - \beta_{(l,m)} z)), \tag{5.67}$$

$$H_z = C_D K_l(\rho_{cr}) \exp(i(\omega t + l\phi - \beta_{(l,m)} z), \tag{5.68}$$

where $\rho_{cr} = \rho_c r/\rho$. The mode electric field intensity profiles are similar to the modes of an optical fibers in shape.

5.6 Photonic Band Gap Crystal

The term photonic crystal (PhC) is used to describe a periodic refractive index modulation, in a similar manner to the periodic arrangement of atoms in a crystal. In the PhC the photons are effected by the modulation. Taking the analogy further, since a certain specific wavelength band cannot propagate within the PhC there is a "photonic bandgap". This field of physics was pioneered by Yablonovitch [166] and John [167]. The DBR explained in the previous section is a good example of a 1D photonic band gap. Shown in Fig.5.8(**a**) is an example of a 1D PhC in a base material with air gaps (holes). The square function of the refractive index blocks a wide part of the spectrum [168].

Figure 5.8(**b**) shows an example of a 2D-PhC. For photons propagating along the x-axis or the y-axis of the system, the solution is exactly the same as the 1D problem. For a photon propagating in another direction ($\alpha\hat{x}+\beta\hat{y}$), the conditions become more complex, but there is still a wavelength band that is not allowed to propagate along the axis. Doing this for all the available propagation directions in 2D generates a

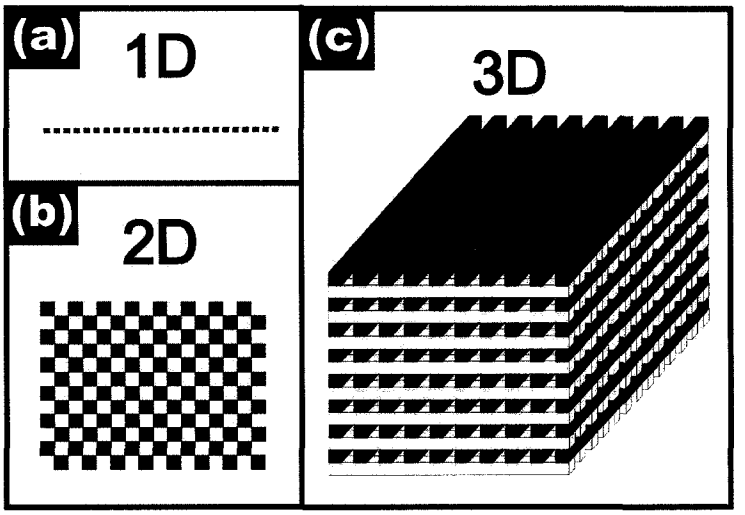

Figure 5.8: Cartoon examples of photonic crystal in **(a)** 1D, **(b)** 2D, and **(c)** 3D.

photonic band diagram, where the photonic bandgap is defined as the energy range over which photons cannot propagate in any direction.

The concept can just as easily be extended to 3D. Fig.5.8**(c)** illustrates an example of a 3D-PhC, the "woodpile" configuration [169]. Another quite common configuration for 3D-confinement is a face-centered-like configuration of spherical air holes within a solid material. This PhC type is also known as opal [170,171]. It is common because it is relatively easy to fabricate by infiltrating a stack of styrofoam spheres with a solid polymer and subsequently removing the spheres by chemistry. Consult one of the numerous books on the topic for further information about the various PhC [165,172,173].

A 2D-PhC embedded within a thin ($\sim \lambda/n$) layer of high refractive index material surrounded by air on top and bottom is used in this work. Such a structure is also

referred to as a PhC membrane. Photons are manipulated within the plane by a PhC consisting of a periodic arrangement of air holes, while the third axis confinement results from total internal reflection.

There are many different theoretical methods to determine the photonic band structure of such a membrane. These fall into two complementary categories: frequency domain methods that easily extract the band structure but say little about cavity mode emission properties and time domain methods that are very useful for cavity properties but are inefficient to uncover the band structure. In the frequency domain we have used numerous methods that provide the band structure of a PhC with or without a defect. An effective index approach yields quick and qualitative results [174]. An S-matrix approach proved accurate but difficult to extend to calculations with defects within the PhC [175]. A Green's function approach also yielded quick results thanks to fast-Fourier transform (FFT) algorithms (even in 3D) but again the effect of an added defect is hard to resolve with this technique [174]. The frequency-domain method used most extensively is a plane wave expansion method [176] and this will be discussed in the next section. The finite-difference time-domain (FDTD) method is the only time-domain method we used. The following sections describe in greater detail the two simulation techniques mainly used within the scope of my project.

5.6.1 Frequency Domain - Plane Wave Expansion

This method is the basis of the Massachusetts Institute for Technologies (MIT) Photonic Bands package available in the public domain from the Joannopoulos group

[176]. The electro-magnetic field is expanded in plane waves such that:

$$\vec{E} = \vec{E}_{\vec{k}}(\vec{x})e^{i\vec{k}\cdot\vec{x}}, \tag{5.69}$$

$$\vec{E}_{\vec{k}}(\vec{x}) = \sum_m \vec{E}_{\vec{G}_m} e^{i\vec{G}_m\cdot\vec{x}}, \tag{5.70}$$

where $\vec{G}_m$ are the reciprocal lattice vectors and $\vec{E}_{\vec{G}}$ is orthogonal to $\vec{k}+\vec{G}$. Maxwell's equations are solved through repetitive FFT and inverse FFT. This code is quite powerful, but can become quite demanding for full 3D calculations. The biggest advantage of this code is the fact that it is freely available [176].

5.6.2 Time-Domain - Finite-Difference Time-Domain Simulations

The re-normalized time-dependent Maxwell's equations are:

$$\frac{\partial \vec{D}_s}{\partial t} = \sqrt{\frac{1}{\varepsilon_0\mu_0}}\nabla \times \vec{H}, \tag{5.71}$$

$$\vec{D}_s = \varepsilon_r^* \vec{E}_s, \tag{5.72}$$

$$\frac{\partial \vec{H}}{\partial t} = -\sqrt{\frac{1}{\varepsilon_0\mu_0}}\nabla \times \vec{E}_s, \tag{5.73}$$

where $\vec{E}_s = \sqrt{\frac{\varepsilon_0}{\mu_0}}\vec{E}$ and $\vec{D}_s = \sqrt{\frac{1}{\varepsilon_0\mu_0}}\vec{D}$ are the normalized electric field intensity and normalized electric flux density, respectively. Eqs.(5.71) to (5.73) are discretized using central-difference approximations to the space and time partial derivatives as was first suggested by Yee [177]. The actual term finite-difference time-domain (FDTD) was coined later by Taflove [178].

The resulting finite-difference equations are solved in step-like fashion. The electric field vector components in a volume of space are solved at a given instant in time followed by the magnetic field vector components in the same spatial volume the next instant in time. The process is repeated over and over until the desired transient or steady-state electromagnetic field behavior is fully evolved.

We used commercial software from the company Lumerical Solutions inc. [179]. The simulations are done on a quarter of the structure using appropriate boundary conditions (*i.e.* symmetric or asymmetric boundaries to imitate the full structure). A lattice including 7 rings of holes surrounds a defect in the PhC. The grid sizes in the plane of the membrane are $0.05a$ along the x-axis and $0.043a$ along the y-axis. An appropriately polarized dipole source is used to excite the cavity modes. Perfectly matched layer boundary conditions were employed on all outer boundaries. Point time-domain monitors were used to measure the mode peak energies at various positions within the microcavity, as a Fourier transform of the time dependence. Many detectors are compared to ensure the validity of the information. While the Q-factor of a certain mode can be extracted from the ratio of the FDTD-obtained peak energy and peak linewidth, it is better to measure the radiative decay rate of the mode to extract its lifetime and thus the Q-factor. The mode field pattern is extracted using a planar detector (also known as frequency-domain profile monitors) placed just above the membrane surface. Figure 5.9(**a**) presents a typical electric field intensity mode profile obtained by FDTD. These profiles agree well with those obtained by frequency domain methods such as MIT Photonic Bands. The far-field pattern is evaluated from a far-field transformation starting from the data collected

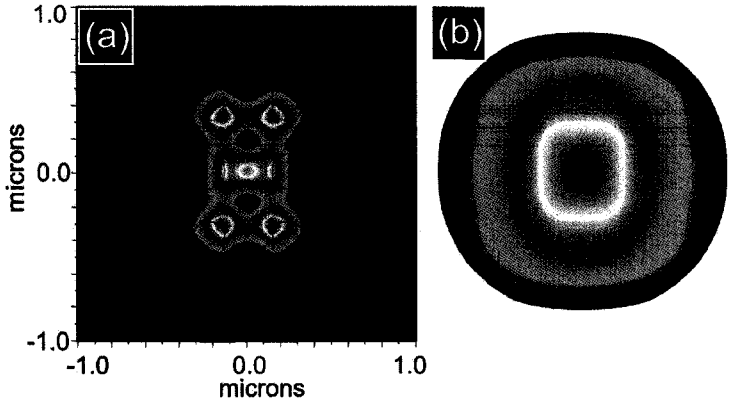

Figure 5.9: Typical FDTD results. **(a)** Mode electric field intensity profile and **(b)** far-field radiation pattern for a photonic crystal microcavity with the x-dipole-like mode optimization (see section 8.2.4).

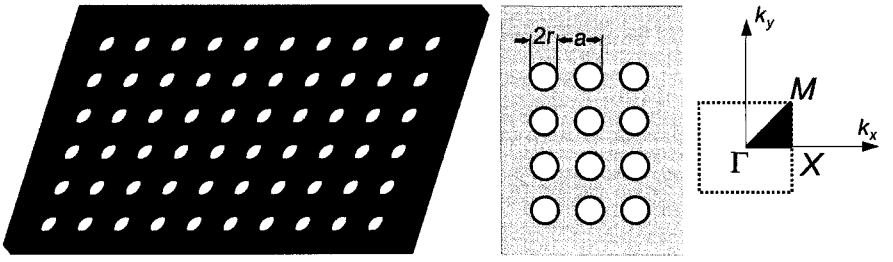

Figure 5.10: Square lattice of air holes PhC membrane 3D representation, top view, and 2D Brillouin zone.

by the frequency-domain monitor. Fig.5.9(**b**) shows a polar plot of the far-field as projected onto a hemisphere with a radius of 1 meter.

5.6.3 Membrane with a Square Lattice

Figure 5.10 shows a PhC membrane with a square lattice of air holes in 3D and from a top view angle (2D). The third panel shows the PhC 2D Brillouin zone in k-space. The 2D photonic band diagram is presented in Fig.5.11 (inset shows the variation of

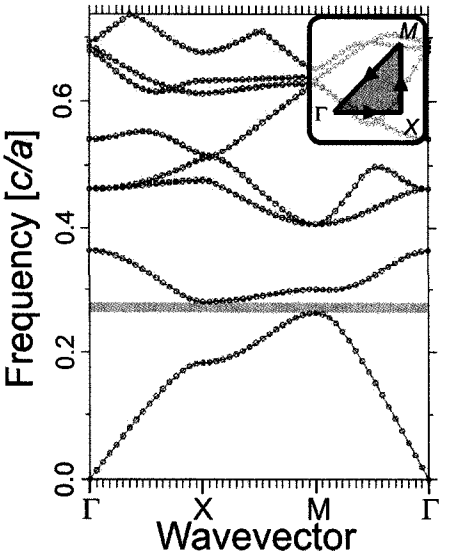

Figure 5.11: Air holes square lattice 2D-PhC TE band diagram simulations with MIT Photonic Bands code for hole radii r=0.4a and the material refractive index n_m=3.5. Inset shows the wavevector variation along the k-space for the plot.

the wavevector along the Brillouin zone) for the first 8 transverse electric field (TE) bands as calculated by the MIT Photonic Bands package. The host lattice hole radius is equal to 2/5 of the hole lattice pitch a and the material refractive index (n_m) is equal to 3.5. TM modes will in general not be well contained by this type of photonic crystal. The y-axis is the frequency in units of c/a where c is the speed of light. The highlighted band of frequency around 0.25 shows the bandgap, where photons are not allowed to propagate in any direction within the membrane plane. The bandgap is quite narrow. To create efficient microcavity modes based on a PhC, a larger bandgap is preferable. Nevertheless, some groups were able to achieve good results with such a PhC lattice [143, 180].

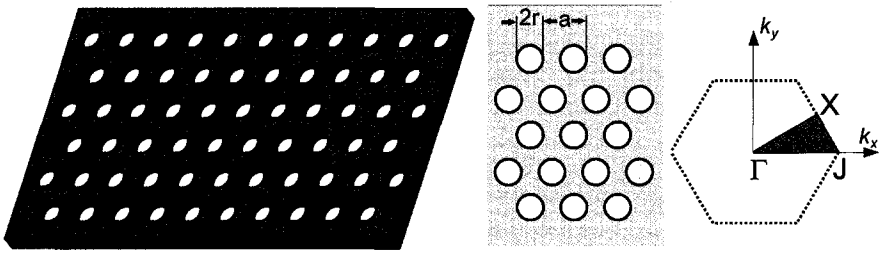

Figure 5.12: Hexagonal lattice of air holes PhC membrane 3D representation, top view, and Brillouin zone.

5.6.4 Membrane with a Hexagonal Lattice

A hexagonal lattice PhC is illustrated in figure 5.12. On the right is illustrated the corresponding 2D reciprocal lattice Brillouin zone. The photonic band diagram is shown in figure 5.13, as obtained with the MIT Photonic Bands solver for a 2D-PhC with $r = 0.4a$. The mode energy is displayed along the wavevector path highlighted by the inset in the top right corner. We use this type of photonic crystal because its photonic band gap is typically larger here than for the square lattice membrane. This feature explains why triangular (hexagonal) lattices are extensively used to fabricate 2D-PhC microcavities.

5.7 Photonic Crystal Microcavity

A microcavity can be created from a PhC membrane simply by introducing a defect into the 2D repetitive pattern [181]. For example, it is possible to generate a defect which supports modes by simply moving two neighboring holes off their lattice position away from each other [182]. More simply, a microcavity is created when a hole is removed from the lattice (see Fig.8.5).

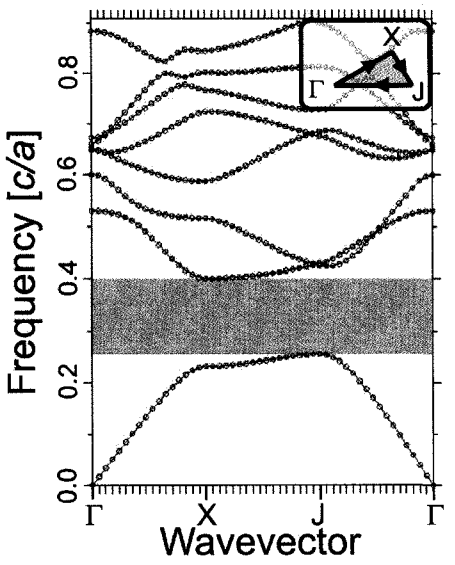

Figure 5.13: Air holes hexagonal lattice 2D-PhC TE band diagram simulations with MIT Photonic Bands for r=0.4a and n_m=3.5. Inset shows the wavevector variation along the k-space for the plot..

By adjusting the size and position of the holes surrounding the defect one can greatly change the microcavity mode structure and the mode properties. Unfortunately, there is no analytical theory to determine which modes a microcavity will support and the quantitative properties of such modes. The only way to know the consequences of a slight movement of one or many holes on the modes is a full scale simulation using FDTD methods or by fabricating a sample.

Another simulation tool for PhC microcavities uses the Green function tensor (GFT) formalism [183–187]. This very powerful tool is not only able to simulate single photon propagation within a PhC waveguide and a PhC microcavity, it is also able to simulate the coupling between a SQD and one or two microcavities. The

GFT is used to propagate the field from one point to the next and it is possible to extract the GFT for a PhC, a PhC microcavity, etc. However the degree of complexity involved to perform GFT-based simulations prevented us from utilizing this technique ourselves. The interested reader is invited to consult references [183–187] and references therein for further details about the GFT formalism.

Englund, Fushman and Vučković have developed what they call an Inverse Technique to optimize a microcavity design to get a higher cavity quality factor Q [188]. They derived a simple expression for out-of-plane losses in term of the k-space distribution of the microcavity mode. Using this they can select a field that generates a high Q. They then approximate the cavity design for each high symmetry direction (1D) with an analytical relation between the microcavity field and the dielectric constant along a particular symmetry axis. There is some debate about the usefulness and generality of this procedure and our own attempts in this direction did not prove informative. The Fabry-Pérot (FP) model is also an approximation of the microcavity to a 1D problem. The next section describes this technique in detail, since it will be used for qualitative analysis of our experimental data.

5.7.1 Fabry-Pérot Model

This approach was adapted to PhC microcavities by Sauvan, Lalanne and Hugonin [189]. It consist simply of approximating the problem as a 1D one with a small area surrounded on each side by a PhC mirror. The area has a length L and a refractive index given by n_m. Finding the mode wavelength (λ_0) of such a microcavity amounts

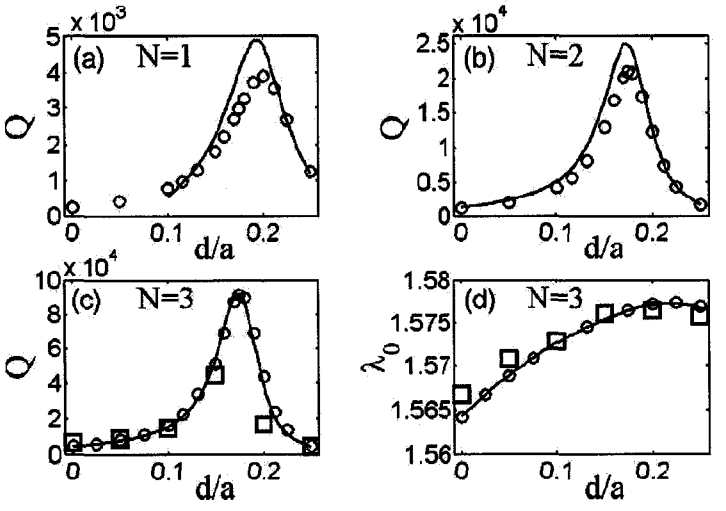

Figure 5.14: Mode peak wavelength and Q-factor as a function of defect enlargement for structures with N missing holes. Squares are experimental data points, circles are FDTD results and the plain line is obtained with the FP model. From [189]

simply to solving a Fabry-Pérot (FP), *i.e.* meeting a simple phase matching condition. The total phase delay $\Phi_T(\lambda_0)$ for a half cavity cycle has to be equal to a multiple of π [189]:

$$\Phi_T(\lambda_0) = 2\pi n_{eff}(\lambda_0)L/\lambda_0 + \phi_r(\lambda_0) = p\pi, \tag{5.74}$$

where $n_{eff}(\lambda_0)$ is the cavity mode effective index, L the cavity length, $\phi_r(\lambda_0)$ the PhC reflection associated dephasing at λ_0 and p an integer. The cavity quality factor ($Q = \lambda_0/\Delta\lambda$) is given by [189]:

$$Q = \frac{\pi}{1 - |r(\lambda_0)|^2}\left(\frac{2Lc}{\lambda_0 v_g(\lambda_0)} - \frac{\lambda_0}{\pi}\left(\frac{\partial\phi_r}{\partial\lambda}\right)_{\lambda_0}\right), \tag{5.75}$$

where $|r(\lambda_0)|^2$ is the mode reflectivity and $v_g(\lambda_0)$ the group velocity at λ_0.

This FP model was successfully used by Sauvan *et al.* to predict a rise and fall in both Q and mode peak energy as a function of the defect enlargement for both

the single missing hole and the triple missing hole defect in an hexagonal lattice, as seen in figure 5.14, where the empty squares are experimental data points, empty circles FDTD results and the plain line is obtained with the FP model. The defect enlargement here means that two holes on opposite sides of the defect along the x-axis are moved away from the defect center. We did not achieve to produce such simulations ourselves, but it can nevertheless be used to qualitatively describe out experimental results.

Chapter 6

Probing Microcavities

The properties of a fabricated microcavity are hard to predict. As was shown in section 5.6, it is possible to simulate the device but a detailed characterization of the microcavity is required to support a precise simulation. A good way to probe the mode structure is to embed a broadband light source within it. The density and spectral distribution of the photons escaping the device tell us what the microcavity properties are. Quantum wells (QWs) and quantum dots can be used as embedded emitters as will be described later. Another type of embedded emitter is the substrate itself. Results using the substrate nonlinear emission process (second harmonic generation (SHG) to be specific) will be presented.

Although the use of a broadband emitter is a useful technique, it is crucial to develop a technique to probe the microcavity mode structure that does not rely on the embedded QDs because when using a SQD or few QDs it is possible that no QD emission line will be in resonance with the microcavity modes, so that no diagnostic would be available to probe the cavity. The SHG mentioned earlier works properly to that effect. Evanescent field coupling to the microcavity and resonant

scattering (RS) also allow measurement of the microcavity properties without requiring embedded emitters.

6.1 Embedded Emitters

Four different types of embedded emitters will be discussed: QWs, a QD ensemble, a SQD and the substrate itself. All of these produce photons which are excited and collected by a normal PL setup (except for the SHG setup where slight adjustments have to be made) as extensively explained in section 3.4.1. It is worth mentioning that the microscope objective used to collect the photons and send them to a spectrometer could in theory be replaced by a near-field scanning optical microscopy (NSOM) device to provide excellent spatial resolution of the microcavity and allow direct study of the modes as was done by Louvion *et al.* [190, 191].

6.1.1 Quantum Wells

Quantum wells (QWs) were the primary candidates for emitters since they are a very well understood and characterized technology. In addition, they are easier to fabricate than QDs. Their limitation is the narrow emission range that they provide; it is probable that one or many of the microcavity modes will not lie within the QW spectral range. The way around this is to insert multiple QWs with different emission properties. Even with this trick though, the end-result is either spectrally limited or cumbersome to fabricate.

6.1.2 Quantum Dot Ensemble

The fabrication process for Stranski-Krastnow QDs inherently yields a wide distribution in QD size and shape. This means a large spectral distribution and very broadband source to probe the microcavity [192]. Since the goal of the project is to put a SQD within a microcavity, using the same material system, it seems sensible to use a dot ensemble for the cavity design process. The idea is to develop the cavity fabrication process by first constructing devices with QD ensembles and to then transfer this process to a SQD sample.

6.1.3 Single Quantum Dot

It is hard to talk about using a SQD to probe the mode structure *per se* but it is true that if a microcavity mode and a SQD emission line overlap, then a PL setup will detect the emitted photons. To fabricate an efficient single photon source, the QD single exciton line needs to couple to the desired microcavity mode, but to investigate the mode properties to a certain extent it is possible to strongly excite the SQD so that many emission lines are present. In addition, as the sample temperature is raised, the emission linewidths increase. The spectral range covered will be quite small compared to that of a QD ensemble of course and the quantity of photons will be much lower.

6.2 Substrate Second Harmonic Generation

The material composing the substrate and the cap layer is available in much larger quantity than the QD material. It is possible to use the substrate to our advantage, namely to use its second order susceptibility $\chi^{(2)}$ to produce second harmonic generation (SHG) [193, 194]. The modes provide a high intensity field to amplify the $\chi^{(2)}$ emission of the substrate. The InP of our PhC microcavities fortunately produces a large signal in the visible-NIR region of the spectrum. The experimental setup used by our colleagues at the University of British Columbia in the group of Prof. Young to measure our samples is shown in Fig.6.1. The tunable laser (Spectra-Physics optical parametric oscillator (OPO) operated around 1.5 μm at 80 MHz with 100 fs-long pulses) is power and polarization controlled by a halfwave plate ($\lambda/2$) and a Glan prism (P). A microscope objective (L1) focuses the excitation onto a single microcavity while a second objective (L2) collects the transmitted laser light and the SHG signal. A second Glan prism is used to probe various polarizations of the signal and/or reject the incident laser. A long wavelength pass filter (LWP) is also added to remove the laser photons and allow the SHG signal propagation. A third lens (L3) focuses the signal via a single grating spectrometer onto a cooled CCD array.

A typical result for one of our InAs/InP QDs PhC microcavity membranes is shown in Fig.6.2. The embedded QDs PL (dashed lines) is contrasted with the SHG data (solid line) with the x-axis shifted by a factor of 2 to better compare the two [193]. The agreement is quite good if the sum-frequency generation peak, located between the two others, is filtered out. This, of course, is a limitation to the SHG approach to probe the mode structure. An *a priori* knowledge is required to enable the labeling

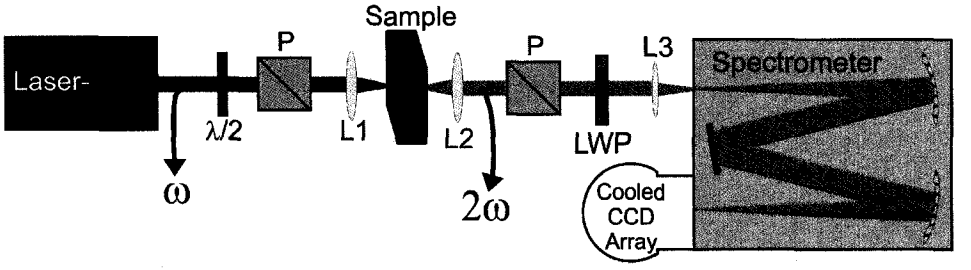

Figure 6.1: Experimental setup to measure the second harmonic generation (SHG) signal. Detail description is given in the text.

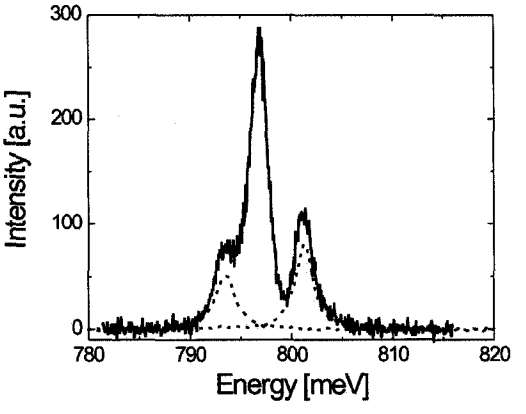

Figure 6.2: Typical SHG experimental result for a InAs/InP PhC microcavity (solid line). Dashed lines are the PL results. From [193]

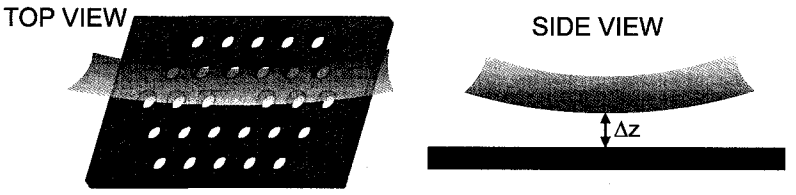

Figure 6.3: Cartoon representation of the the evanescent field probing of a PhC microcavity with a silica nanowire.

of legitimate modes with respect to the sum-frequency generated ones.

6.3 Evanescent Field Coupling

The use of the evanescent field of a silica nanowire to couple to microcavities was pioneered by Srinavasan *et al.* [195–197] where the nanowire is a fiber-taper. Prior to their work, Knight *et al.* were using a phase-matching approach to excite the microcavity modes [198]. A cartoon representation of the nanowire coupling with a PhC microcavity is presented in figure 6.3 for a top and side view. The proximity of the nanowire with respect to the microcavity causes a three-fold effect.

First, the microcavity is probed by the evanescent field of the fiber, coupling with the evanescent fields of the microcavity modes. Second, because the nanowire and the microcavity actually becomes a coupled system it provides a means to tune the microcavity resonant wavelength because of the mode coupling effect [199, 200]. The tuning in wavelength will be accompanied by a change in Q as can be explained by coupled mode theory. For situations where the microcavity energy and embedded SQD exciton line do not properly overlap one can think of using this to effectively

tune the PhC microcavity mode energy. The nanowire proximity will also lead to other parasitic effects such as re-direction of the QD PL towards transverse magnetic field (TM) slab modes as shown by Hwang *et al.* [201]. Considering those effects we can write the nanowire-influenced quality factor (Q_T) as measured by the transmission spectra as:

$$\frac{1}{Q_T} = \frac{1}{Q} + \frac{1}{Q_f} + \frac{1}{Q_p}, \tag{6.1}$$

where Q_f is the Q-factor associated with coupling with the fiber and Q_p the Q-factor associated with the parasitic effects. From coupled mode theory we can relate Q_T and Q by a simple equation [199, 202]:

$$Q_T = \sqrt{T(\lambda)}Q, \tag{6.2}$$

where T is the amplitude of the transmission dip for the mode .

Thirdly, the nanowire can also provide a means to collect the emitted photons from the sample [203]. Once the photons are in the silica nanowire, they are naturally funneled to the rest of the fiber. The end result would be a very efficient feed of the recombination photons to our fiber-based quantum information processing channel. There is an intricate balance to be reached between the ability to tune the microcavity mode while preserving the cavity Q and the ability to extract the photons efficiently [200].

The photon extraction efficiency (ϵ) is given by the product of the spontaneous emission (SE) coupling factor between the embedded emitters and the microcavity (β_{SE}) and the optical components collection efficiency of the microcavity photon (η):

$$\epsilon = \beta_{SE}\eta. \tag{6.3}$$

But β_{SE} is related to the coupled nanowire-microcavity Purcell factor ($F_p{}^{(T)}$) by:

$$\beta_{SE} = \frac{F_p^{(T)}}{F_p^{(T)} + 1}, \tag{6.4}$$

where

$$F_p^{(T)} = \frac{3Q_T(\lambda/n)^3}{4\pi^2 V}, \tag{6.5}$$

and,

$$\eta = \frac{1/Q_f + 1/Q_p}{1/Q + 1/Q_f + 1/Q_p}. \tag{6.6}$$

Considering an ideal experimental setup, Q_p goes to infinity and we can re-write (6.6) as:

$$\eta = 1 - \frac{Q_T}{Q}. \tag{6.7}$$

Inserting equations (6.4) and (6.7) in (6.3) we get an equation describing the evolution of ϵ as a function of Q_T:

$$\epsilon = \frac{\frac{3Q_T(\lambda/n)^3}{4\pi^2 V}}{\frac{3Q_T(\lambda/n)^3}{4\pi^2 V} + 1}\left(1 - \frac{Q_T}{Q}\right) \tag{6.8}$$

Using Eq.(6.8), we can plot the extraction efficiency as a function of the coupled system quality factor Q_T for different mode properties (different Q and V) as shown in figure 6.4**(a)**. There clearly is an ideal Q_T for which the situation results in an optimal extraction efficiency. One could think of a scenario where a microcavity is designed to be purposefully at a slightly lower wavelength and as the fiber is brought into proximity, the mode wavelength adjusts to match while creating a Q_T lower than Q by the appropriate amount to produce efficient capture of the emitted photons within the fiber. To provide a better understanding of the parameter space a contour plot of ϵ as a function of both Q_T and Q is provided is figure 6.4**(b)** for a fixed mode volume at half a cubic wavelength. With a Q of 10 000 and a $Q_T = Q/2$, the

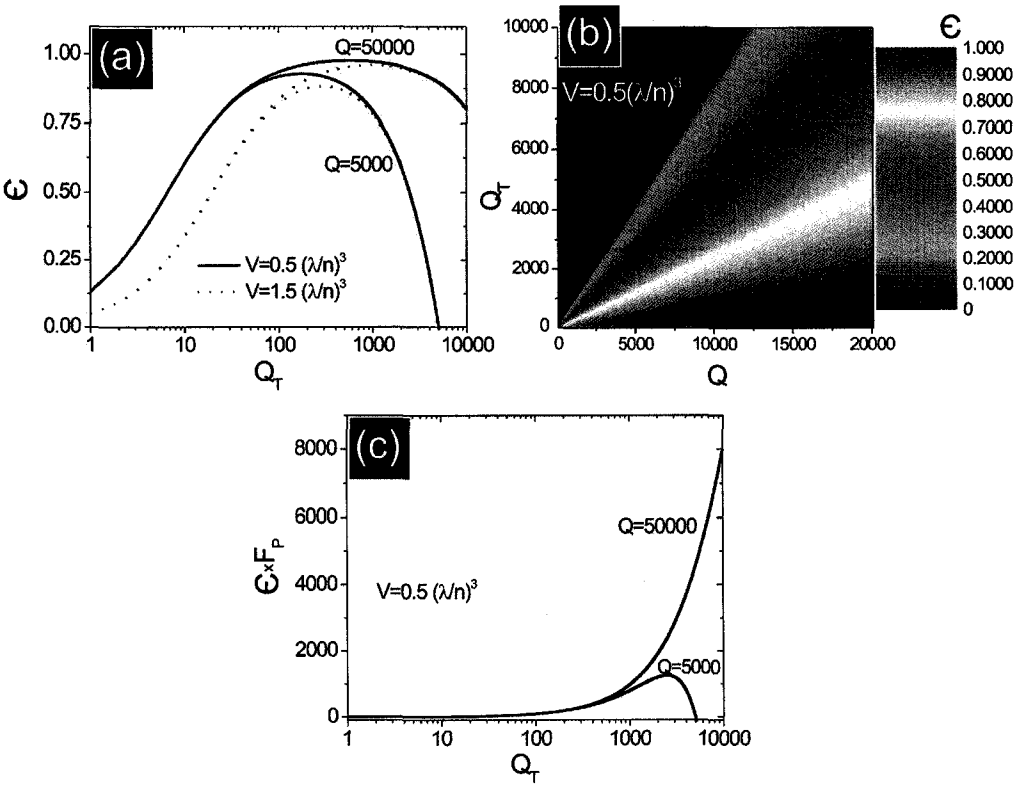

Figure 6.4: **(a)** Theoretical variation of the extraction efficiency (ϵ) as a function of Q_T for different Q and V values, from [200] **(b)** Intensity plot of calculated ϵ as a function of Q and Q_T for $V = 0.5(\lambda/n)^3$. **(c)** Product of ϵ and the Purcell factor as a function of Q_T.

extraction is still within the 50% range. Figure 6.4(**c**) presents the product of the extraction efficiency and the Purcell factor as a function of Q_T, an interesting number to consider since extraction efficiency *and* the repetition rate of the device will lead to a highly efficient single photon source. Also to be considered is the need for the coupled system to stay in the weak coupling regime. Our experimental results using this system will be presented in section 8.5.

6.4 Resonant Scattering

Cross-polarized resonant scattering (RS) allows one to probe the mode structure of a PhC microcavity without the use of an embedded source [193, 194]. The technique involves measuring the reflection or transmission intensity of a resonantly tuned laser pulse, tightly focused to only probe the microcavity structure on the sample. The detected data is analyzed with a polarization opposite to the incident laser linear polarization. All of our measurements with this technique have been performed at the University of British Columbia within the group of professor Jeff F. Young, with our samples, and hence are not a direct result of the work performed within this thesis. Their experimental setup is shown in Fig.6.5. The laser source (Spectra-Physics OPO tuned near 1.5 μm with 80 MHz repetition rate of 100 fs pulses) is power controlled with a halfwave plate ($\lambda/2$) and polarizing cube (P) combination. Light is focused onto a small area of the sample with a microscope objective (L1). The transmitted light is collected with another objective and sent to a second Glan prism and Fourier transform infrared spectrometre (FTIR).

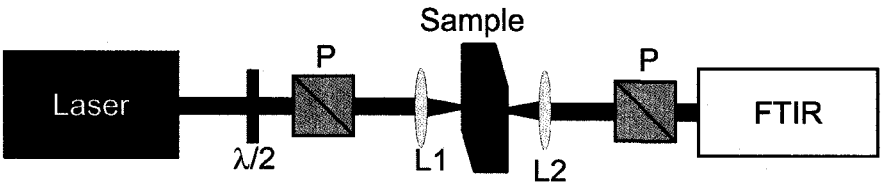

Figure 6.5: Resonant scattering (RS) experimental setup. Detailed setup description is given in the text.

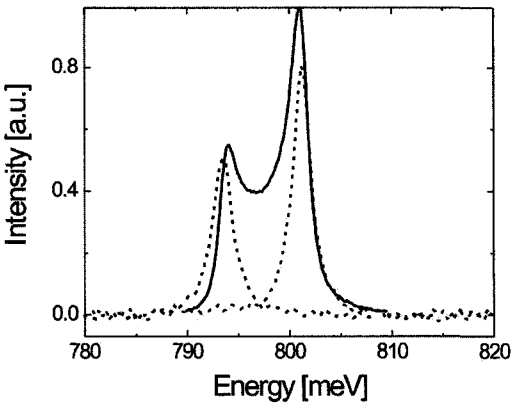

Figure 6.6: Typical experimental data for an InAs/InP PhC microcavity. Solid line is the RS data and dashed lines are the PL obtained curves for different detection polarizations. From [193].

Figure 6.6 shows a typical experimental result for one of our InP-based PhC microcavities with an embedded high density InAs QDs layer. The RS data is represented by the solid line whereas the dashed lines are two modes as observed by PL with 90^o different polarization dependance. The agreement is quite good and it is clear that the RS technique would work even for a microcavity without QDs. The small discrepancies between RS and PL can be explained by the laser background. See Refs. [193, 194, 204] for a more thorough analysis. RS clearly is a promising technique to probe the microcavity without requiring embedded emitters, the main difficulties being to properly align the experimental setup to reject the incident laser and avoid retro-reflections from the other optical components.

Chapter 7

Quantum Dots in Micropillars

Originally the micropillar microcavity was developed to create a laser source using a quantum well (QW) as the active medium. This was known as a vertical-cavity surface-emitting laser (VCSEL). In theory, a laser constructed from a quantum dot (QD) within a microcavity has a zero lasing threshold (if one considers the notion of threshold to still apply [205,206]). The scientific community did not start exploring this until a decade after its theoretical prediction however (see ref. [207] for a nice review of the first years). In 2001, Yamamoto's group was the first to demonstrate the SQD lifetime alteration due to the micropillar [208] and in the same year the anti-bunching from a single quantum dot (SQD) coupled to a micropillar was demonstrated by another group [209]. Yamamoto's group took a further step by proving the indistinguishability of the single photons (SPs) emitted by a SQD in a micropillar [61] and this was the first QD-microcavity combination to be used as a SP source for quantum key distribution (QKD) using the BB84 protocol [57]. The micropillar microcavity was one of the three "simultaneous" systems to demonstrate the attainment of the strong coupling regime [210] and recently it was used to demonstrate photon anti-bunching from a SQD-microcavity in the strong coupling regime [211].

Many papers are still being published by different groups discussing the optimization of micropillar performances [212–215].

The micropillar was the first microcavity design explored at Institute for Microstructural Sciences (IMS) and this chapter describes the experimental work published [162–164, 216]. Although the initial results were promising, the lack of an easy, post-fabrication tuning mechanism ultimately led us to reject this approach. The first section introduces the microcavity fabrication process, and the following one shows typical SEM and PL results. The last section presents the detailed analysis of the influence of the pillar diameter on the emission properties and the data is compared with the theoretical predictions from an effective index model presented in section 5.5.

7.1 Fabrication Procedure

Our full micropillar fabrication process is shown in figure 7.1. First, a sample with a relatively high density of QDs is grown using our chemical beam epitaxy (CBE) system (see section 3.2 for more details). A 12 pair $\lambda/4$ SiO_2/Ta_2O_5 distributed Bragg reflector (DBR) mirror is deposited onto the sample using a dual ion-beam sputtering system (Spector, Veeco-IonTech) from SiO_2 and Ta targets **(b)**. We used dielectric mirrors of SiO_2/Ta_2O_5 because they are already widely used by the Thin Films group of the IMS to produce very high quality DBR mirrors for wavelengths around 1.5 μm. The sample is then flipped and glued upside-down onto a microscope slide with 3 μm-thick optical adhesive to keep the sample transparent to the QD emission around 1.5 μm **(c)**. The InP wafer is removed, all the way to the InGaAs buffer layer, by

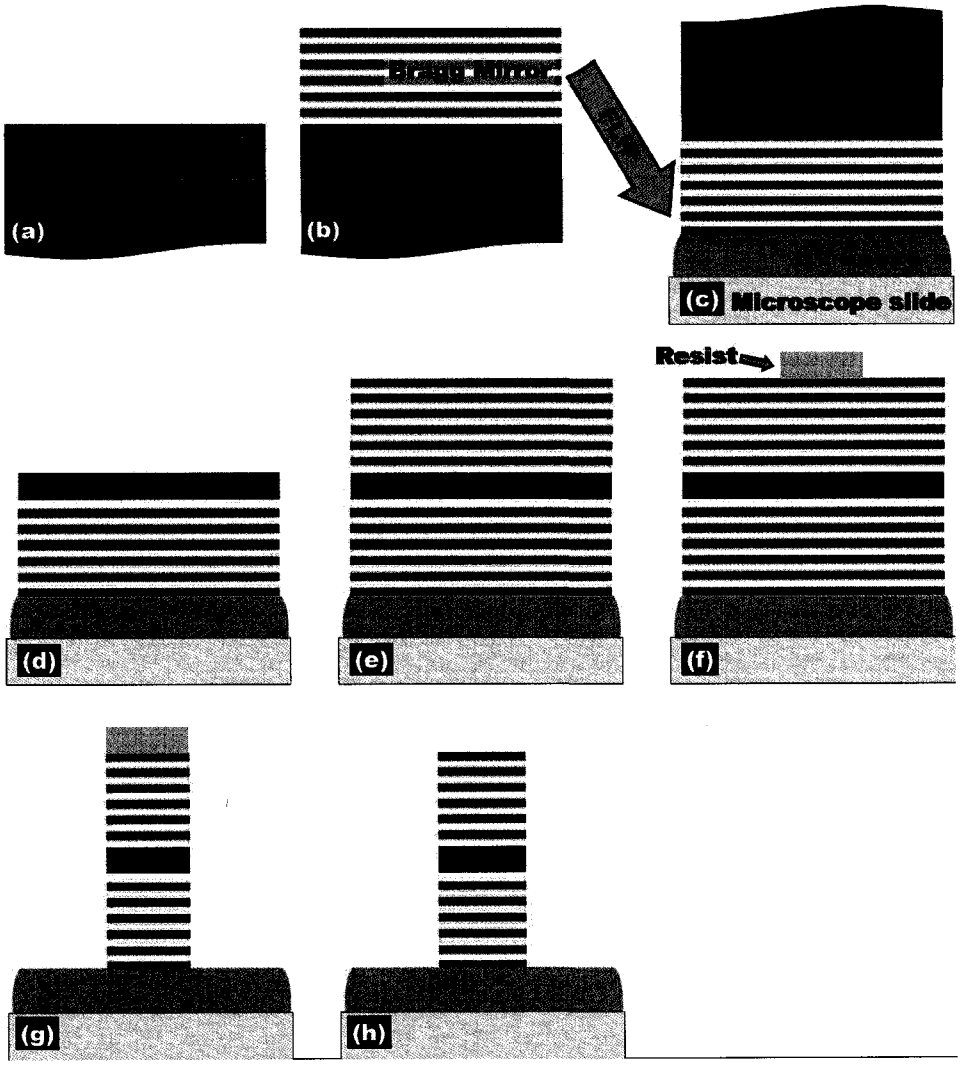

Figure 7.1: Steps involved in the first type of fabrication process of a micropillar. See text for detailed procedure description

selective wet chemistry using a 3:1 mix of HCl and H_2O. The InGaAs buffer layer is removed using a mix of H_2SO_4 and H_2O_2 **(d)**. The second DBR mirror is deposited in the same way as the first onto the remaining InAs/InP QD layer **(e)**.

We now have a high-Q planar microcavity with an infinite number of supported modes. A layer of aluminium is deposited followed by a negative electron-beam resist. The resist is patterned using electron-beam lithography and the unexposed resist removed by a bath of developer (MF321). The accessible Al is etched away with a mixture of phosphoric, acetic and nitric acids (E6)**(f)**. The first DBR is then etched using C_4F_8 in an inductively coupled plasma (ICP). The sample is switched to a second ICP with a chlorine-methane-based mixture to etch the InAs/InP layer. The second DBR is then etched in the original ICP **(g)**. The resist and underlying aluminium remaining on the sample surface are removed using N-Methylpyrolidone (NMP) and E6 etches**(h)**. For some samples the second DBR mirror was not etched, in an effort to limit the edge roughness related losses and decrease the pillar height to improve structural stability.

7.2 Typical Results

Fig.7.2 shows SEM of a typical series of micropillars fabricated in the manner described above. Different pillar diameters are constructed in order to fully test our ability to build such small structures. Each micropillar group is surrounded by a wall (as can be seen in the figure) to prevent the micropillars from falling down in the presence of the flowing liquids used to clean the sample in the final steps of sample

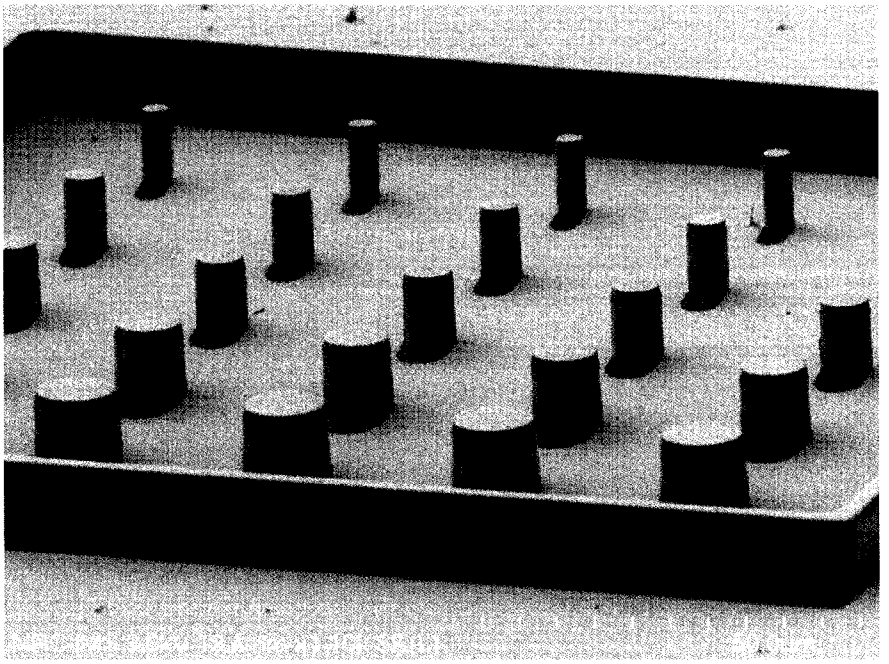

Figure 7.2: Scanning electron micrograph (SEM) of a typical group of micropillars. The wall surrounding the micropillar group is to prevent the liquid flow during the cleaning process from tipping over the micropillars.

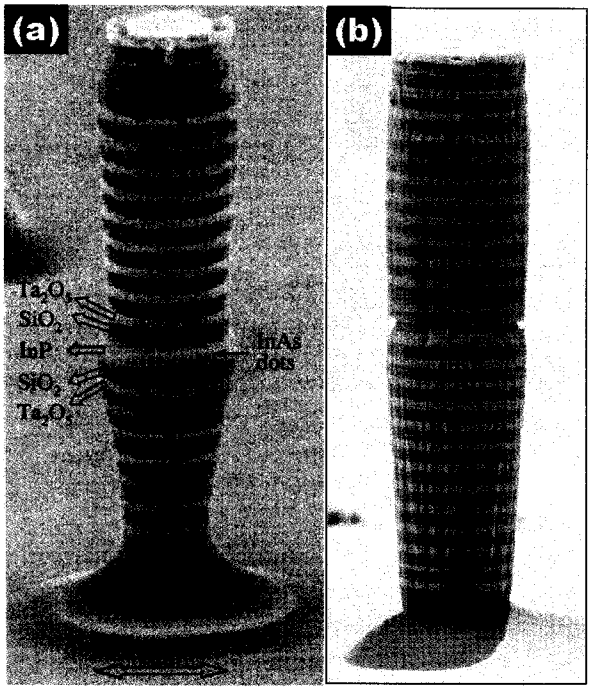

Figure 7.3: High-resolution SEM images of single micropillars with different sample run and different diameter.

processing. Individual small-radii (r_p) pillars are shown in Fig.7.3:**(a)** r_p=1 μm and **(b)** r_p=1.25 μm. Those two pillars originate from slightly different sample processing procedures. The sample temperature for the ICP etch of the bottom DBR of sample **(a)** was too high, producing a more conical shape.

Based on the micropillar shape, one would expect that the sample shown in Fig.7.3**(b)** would have a higher efficiency and Q-factor than its counterpart shown in **(a)**. Even after improvements to the pillar shape were achieved, edge roughness is still present and contributes to losses and lower Q. As the pillar diameter becomes smaller, the edges of the mode leak outside the pillar and the edge roughness creates scattering and losses ($Q^{-1} = Q^{-1}_{\text{losses}} + Q^{-1}_{\text{cavity}}$). Ultimately, we were never invested the

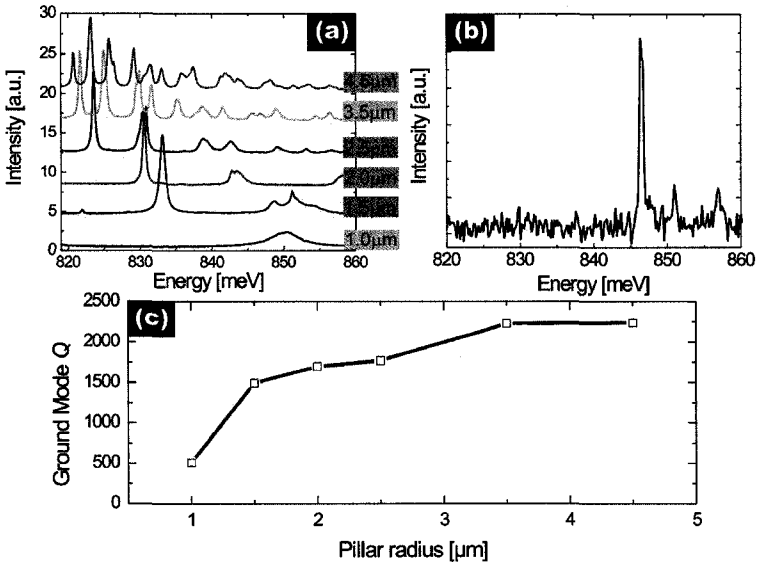

Figure 7.4: Typical micropillar μPL data. **(a)** Increasing micropillar radii PL with 12 periods DBR mirrors. The curves are offset for clarity. From [164] **(b)** Typical μPL data for a 1 μm radius micropillar with 12 layers mirrors. Q=1500 and V=3 μm^2. From [216]. **(c)** Ground state mode Q-factor as a function of the pillar radii. From [164]

time required to develop a fabrication technique to reduce the edge roughness. This is one of the reasons why we moved to 2D-PhC type microcavities.

7.3 Pillar diameter influence

In order to probe the mode structure and quality factor of a microcavity a QD ensemble is embedded within the sample. The PL of the QDs is limited and directed by the microcavity and we can characterize it by measuring the spectral distribution of the outgoing photons. The PL peak energies for pillars with varying radii is shown

in Fig.7.4(**a**) whereas the high resolution μPL of a 1-μm-radius pillar is presented in Fig.7.4(**b**). As the pillar diameter is reduced, the number of PL peaks (*i.e.* the number of modes supported by the device) decreases as is expected from a simple geometrical argument.

In theory, as the micropillar diameter becomes smaller a single high Q mode is supported. In practice this is not the case. As the diameter is reduced the mode quality factor of the fundamental mode actually decreases as can be seen immediately from figure 7.4(**a**) from the linewidth of the lowest energy peaks. The extracted fundamental mode Q as a function of the pillar radius is shown in Fig.7.4(**c**). This decrease is directly attributed to the edge roughness of the pillar. I did not quantify the amplitude of the roughness directly. However, by measuring the Q-factor of the different runs, I was able to indirectly assess the quality of the surface.

Despite these undesirable effects, the mode energies extracted from the PL and the results predicted by effective index theory (see section 5.5) agree well, especially when one considers that there are no fitting parameters involved. In Fig.7.5, the symbols are the experimental data points and the solid and dashed lines are the theoretical peak positions for the EH and HE solutions of a circular waveguide respectively.

The good predictability of the mode energies and the far-field radiation pattern that is suitable to couple to a communications channel are the two main advantages of the micropillar. Unfortunately the Q factor drop due to the edge roughness as the micropillar diameter decreases makes it unsuitable to reach high Purcell factors.

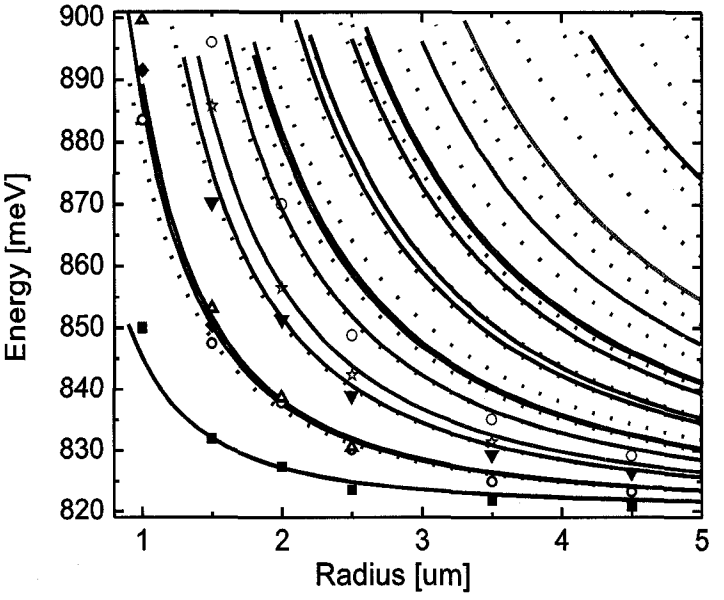

Figure 7.5: Mode peak energy as a function of the pillar radii for different modes. The symbols represent the experimental data points and the lines are theoretical values obtained with the effective index approximation. From [164].

Ultimately, the SQD-micropillar is not an ideal candidate for a SP source because the spectral overlap between the dot and cavity mode is difficult to produce. It is hard to fabricate a micropillar with exactly the right diameter to match the SQD single exciton energy and the micropillar cannot easily be tuned after its initial construction. The application of an electric field or temperature to tune the microcavity resonance are out of the question because they would affect the QD greatly. The main adjustable parameter, once the DBR are constructed, is the pillar diameter and changing it so as to preserve the round nature of the pillar and not adding more edge roughness is quite a challenge. Only recently Lohmeyer *et al.* demonstrated a technique using a focused ion beam to trim the micropillars [217]. Adding material to the micropillar sides is even more challenging and has never been demonstrated to our knowledge.

Chapter 8

Quantum Dots in Photonic Crystal Microcavities

The concept of a photonic crystal (PhC) was invented in the mid-80s, at around the same time as the QD. While the QD-photonic crystal (PhC) combination seems natural, it took some time to actually join them. The first report comes from a European collaboration in 1999 [218]. The huge versatility in microcavity design that is afforded with PhCs allows one to tailor the mode to match the SQD properties while having a very high Q factor and a small mode volume. In 5 fewer years of development than for micropillars, a SQD-PhC microcavity system was brought to the strong coupling regime [210]. The PhC microcavity approach has another advantage; as opposed to micropillars, it provides direct access to the capping layer of the sample. This enables the determination of the QD position from the surface (either with a QD stack [143] or by measuring a bump on the capping layer originating from the presence of the QD [144]).

Fig.8.1 shows a schematic of a PhC membrane with a microcavity at its center. A broadband QD source is located at the middle of the membrane layer. Confinement

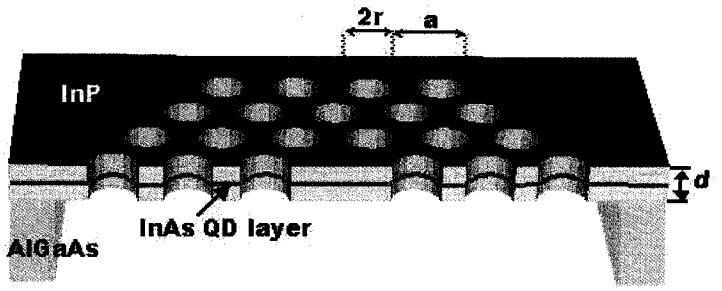

Figure 8.1: Schematic representation of a PhC membrane microcavity.

within the plane is provided by the PhC, vertical confinement comes from total internal reflection. The content of this chapter originates from our numerous publications on the topic [200, 216, 219–224]. Section 8.1 introduces the two different fabrication procedures used for our samples, while the following section presents all the different PhC microcavities we have explored. The third section discusses the results for the cavities and evaluates their compatibility with respect to creating a SP source. Section 8.4 introduces various post-fabrication tuning techniques with more details of our own technique and section 8.5 presents our results with silica nanowire evanescent field probing of PhC microcavities. In addition, microcavity tuning due to coupling to the nanowire is demonstrated. Section 8.6 shows preliminary work done with respect to coupling site-selected QDs to a PhC microcavity.

8.1 Photonic Crystal Fabrication Procedure

Two different approaches were explored to fabricate a suspended PhC membrane. The first involves a sample flipping step, as for the micropillar process, and optical

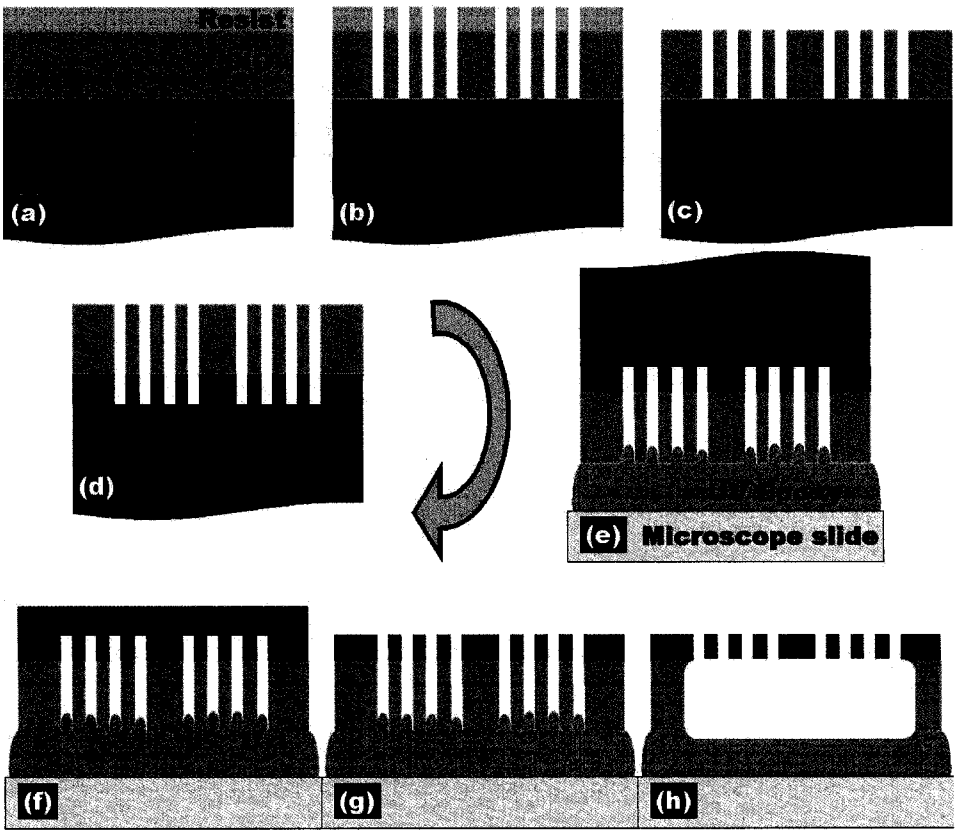

Figure 8.2: Steps involved in the first type of fabrication process of a PhC layer. See text for detailed procedure description

glue, whereas the second is simpler and takes full advantage of selective wet etching processes.

8.1.1 Glue and Flip

Figure 8.2 introduces the first type of fabrication process. This process was used only because we were using a planar QD sample where the underlying InGaAs layer was too thin to provide a sufficiently thick layer of air underneath the membrane. An

insufficiently thick air gap induces large emission losses because of coupling to the InP substrate.

Starting with a high density layer of InAs/InP QDs, we deposited a SiO_2 layer followed by a layer of positive tone electron beam resist from Nippon Zeon (ZEP) (Fig.8.2(**a**)). The PhC pattern is written in the resist and is developed with O-Xylene. The exposed SiO_2 is etched by ICP with C_4F_8 (**b**) and the unexposed resist is then removed by wet chemistry (**c**). The holes within the InAs/InP layer are created with a Chlorine Methane chemistry ICP. The SiO_2 side is glued to a microscope slide using optical glue, flipping the sample (**e**). The InP wafer is etched away with a 3:1 $HCl:H_2O$ mix to leave the InGaAs layer (**f**), which is then removed by a selective wet etching using H_2SO_4 and H_2O_2 (**g**). A buffered oxide etch (BOE) selectively etches the bottom SiO_2 layer through the holes in the InAs/InP QD layer, to provide a layer of air below the PhC membrane (**h**).

8.1.2 Sacrificial Layer

As for the first fabrication technique, layers of SiO_2 and ZEP resist are deposited onto the InAs/InP layer (Fig.8.3(**a**)) and the hole etching procedure proceeds in the same fashion (**b**) to (**d**). Instead of gluing the SiO_2, it is now removed with BOE wet chemistry and the supporting InGaAs layer underneath is removed in a bath of H_2SO_4. Figure 8.1 shows a schematic representation of the resulting device and Fig.8.4 presents three different angle SEM images of an actual device fabricated with this technique.

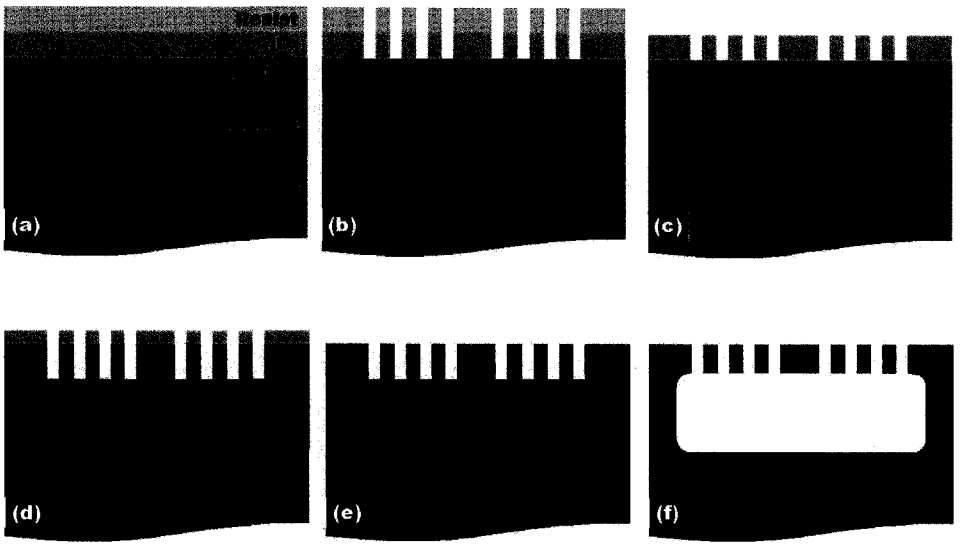

Figure 8.3: Steps involved in the second type of fabrication process of a PhC layer. See text for detailed procedure description

It is not necessary for the PhC lattice surrounding the defect to be infinite to provide a good planar confinement of the mode. While for the type of modes we use in our devices most of the the field is located within the first ring of holes around the central defect, the additional rings are necessary to avoid light leakage. Typically, 19 rings of air holes are used in our experiments to minimize light leakage, while facilitating ease of fabrication. The membrane thickness and pitch between air holes are engineered to provide the desired photonic bandgap. As a rule of thumb both the membrane thickness and pitch are approximately equal to the wavelength in the material to produce a high Q microcavity.

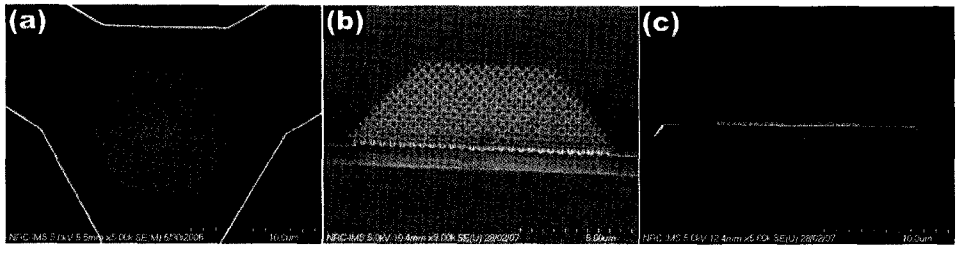

Figure 8.4: SEM images InAs/InP QDs PhC membrane microcavities.**(b)** and **(c)** show a cleaved device at 45° and 90° imaging angle to highlight the suspended membrane

8.2 InAs/InP Quantum Dots in Photonic Crystal Microcavities

In this section we will introduce our PhC microcavities. We use an hexagonal array of circular air holes. The simplest microcavity design is a single missing hole in the lattice. Symmetric modifications to the single missing hole are explored as well as asymmetric changes. The defect can be enlarged along the x-axis, stretching it all the way to a triple missing hole defect. The last section discusses modifications to the defect along the y-axis to optimize an alternative mode.

8.2.1 Single Missing Hole Defect

A single missing hole (**H1**) microcavity (Fig.8.5) supports only two "confined" modes: the x- and y-dipole-like modes. Figure 8.6 introduces their electric field intensity mode profiles obtained by FDTD as explained in section 5.6.2. In theory these two modes are degenerate for an **H1** microcavity. In practice, the degeneracy will be lifted by small imperfections in the PhC lattice or in the microcavity. The PL of an

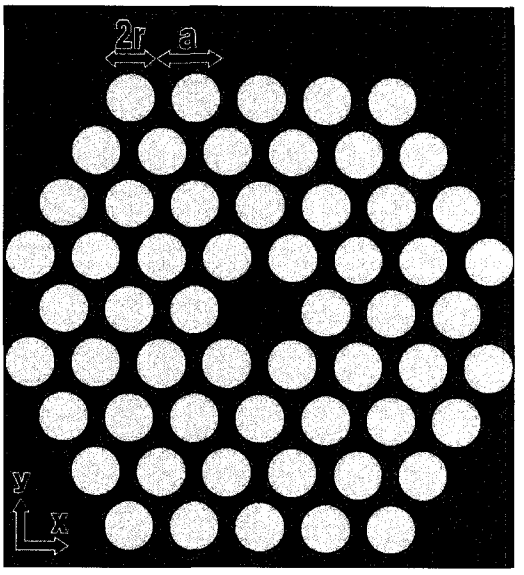

Figure 8.5: Schematics of a single missing hole defect (**H1**) in a triangular lattice of air holes.

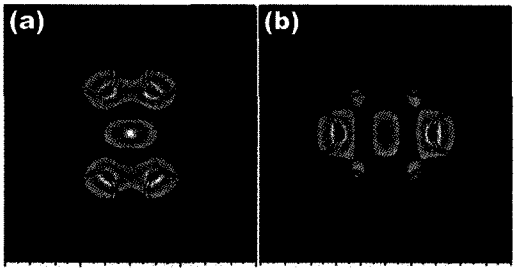

Figure 8.6: FDTD-obtained electric field intensity mode profiles of the two modes supported by a **H1** microcavity. **(a)** x-dipole-like mode and **(b)** y-dipole-like mode. From [219]

H1 microcavity with hole radius r=115 nm, pitch a=500 nm and membrane thickness d=223.5 nm is shown in Fig.8.7(**a**). The two peaks are attributed to the x- and y-dipole-like modes.

It should be noted that the literature oscillates in nomenclature when it comes to the dipole modes. The problem arises from the fact that the mode with the electric field components largely along the x-axis (Fig.8.6(**b**)) has a far-field polarization along the y-axis and vice-versa for the other mode. Some groups refer to the x-dipole-like mode as the one with the field along the x-axis while others call the x-dipole-like mode the one with the far-field polarization along the x-axis. The latter stance will be used throughout this thesis. The interested reader should be careful while consulting our publications on the topic as we ourselves switched between the two nomenclatures.

A detailed polarization dependant photoluminescence (PolPL) measurement is shown for an **H1** microcavity in Fig.8.7(**b**). The peak at lower energy can be attributed to the x-dipole-like mode while the second peak polarized along the y-axis is the y-dipole. The inset in figure 8.7(**b**) shows a polar plot of the integrated intensity for each peak as a function of the polarizer angle with respect to the x-axis. The connected filled circles are from the lower energy peak while the empty circles are from the higher energy peak.

Figure 8.8 shows the PL-extracted mode energy (**a**) and Q-factor (**b**) for both dipole-like modes of an **H1** microcavity as a function of the host lattice radii (r) for different hole pitch (a) values. The filled (empty) symbols represent the measured

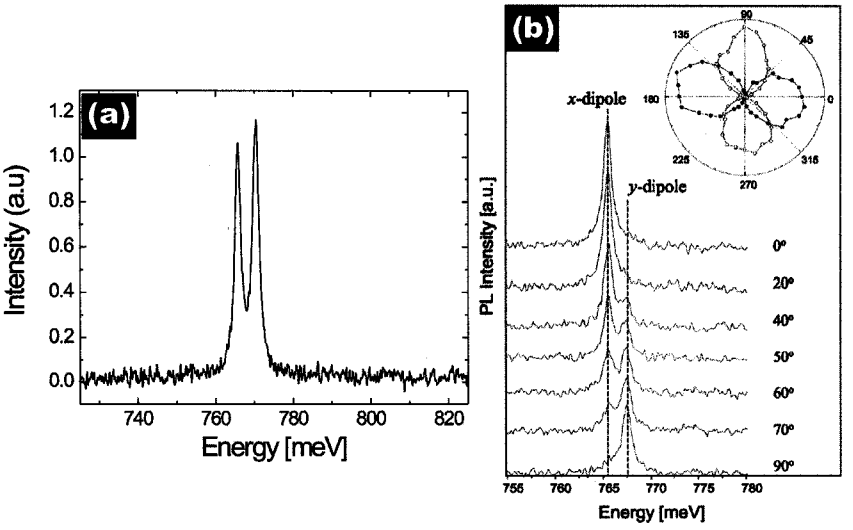

Figure 8.7: **(a)** PL and **(b)** PolPL data for a **H1** microcavity with a=500 nm, r=115 nm, and d=223.5 nm. Filled circles in the polar plot represent the x-dipole-like mode while empty circles represent the y-dipole-like mode. From [219]

y-dipole-like (x-dipole) mode and the solid lines are FDTD simulation results. Triangles refer to the **H1** microcavity with a=485 nm whilst circles and squares represent results for a=500 nm and 515 nm respectively. The highest Q-factor reached with this simple cavity type is approximately 850 for r=120 nm and a=500 nm. By varying the a and r parameters, it is clear that one can fabricate an **H1** microcavity at any desired wavelength around 1.55μm *i.e.* 800 meV.

The Q-factors for each mode, as extracted from the PL, are higher for the y-dipole than the x-dipole-like mode. A detailed SEM analysis of the cavities and FDTD simulations were performed to determine the origin of the larger Q for the y-dipole mode with respect to the x-dipole and the lifted degeneracy [216]. An asymmetry of the holes was discovered; the holes are elliptical, with the longer axis along x and an ellipticity equal to 1.05. The holes elongation is sufficient to explain both the lifted

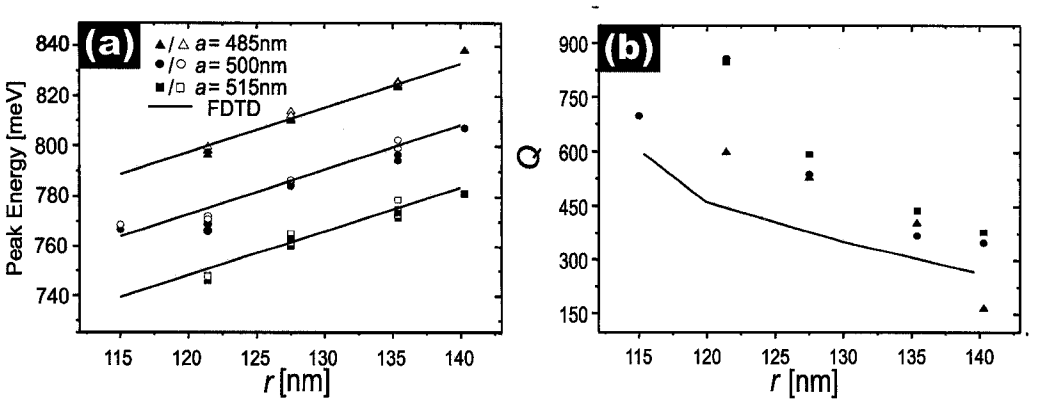

Figure 8.8: Mode peak energy **(a)** and Q **(b)** for the **H1** x- and y-dipole-like mode as a function of host lattice radii with d=223 nm (empty and filled symbols respectively) for a=485 nm (triangles), a=500 nm (circles), and a=515 nm (squares). The solid line represents the FDTD obtained numbers for the same microcavity parameters. From [219]

degeneracy and the higher Q of the y-dipole.

The **H1** Q-factors are not high and yield a potential Purcell factor of $\sim$ 130 considering a perfect spatial and spectral overlap between an eventual SQD and the microcavity. The x- and y-dipole-like mode volume are about $0.65(\lambda/n)^3$, implying that the cavity is in the weak coupling regime. Chang *et al.* have used such a microcavity to produce a SP source at 800 nm with an InAs/GaAs SQD [225]. Modifications to the PhC defect can produce higher Q microcavities. The remainder of this chapter will explore various modifications to the inner ring of holes surrounding the missing hole and study their effects on the microcavity spectral properties. In the next section the defect will be enlarged symmetrically along various crystal axes.

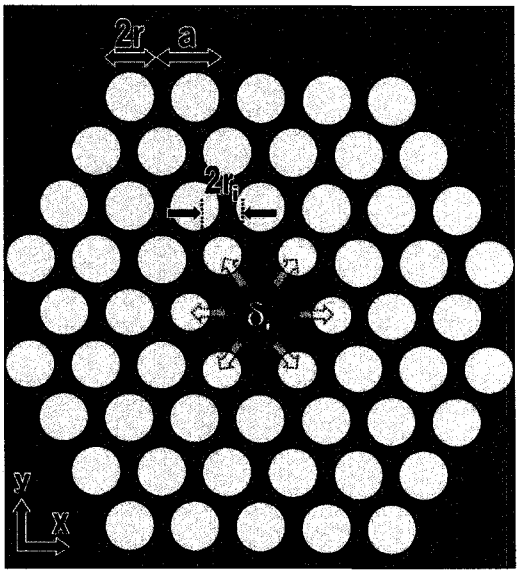

Figure 8.9: Schematic of a symmetrically modified single missing hole defect (**H1S**) in a triangular lattice of air holes.

8.2.2 Symmetric Modifications

A first obvious way to optimize the PhC defect modal properties is to modify the inner ring holes in a symmetric fashion, creating an **H1S** microcavity [221]. One can change the radii of holes (r_i), move them along the axis by δ_i or change both at the same time. A positive δ_i means a shift away from the defect. See figure 8.9 for a schematic representation of the different parameters for an **H1S** microcavity.

The enlargement of the available high refractive index central area results in a greater number of modes supported by the device. The x- and y-dipole-like modes are still present and 4 modes are added: the monopole mode, hexapole mode and 2 different symmetry quadrupole modes. Figure 8.10 presents the electric field intensity profile for the six modes of an **H1S** microcavity with r_i=156 nm, r=175 nm,

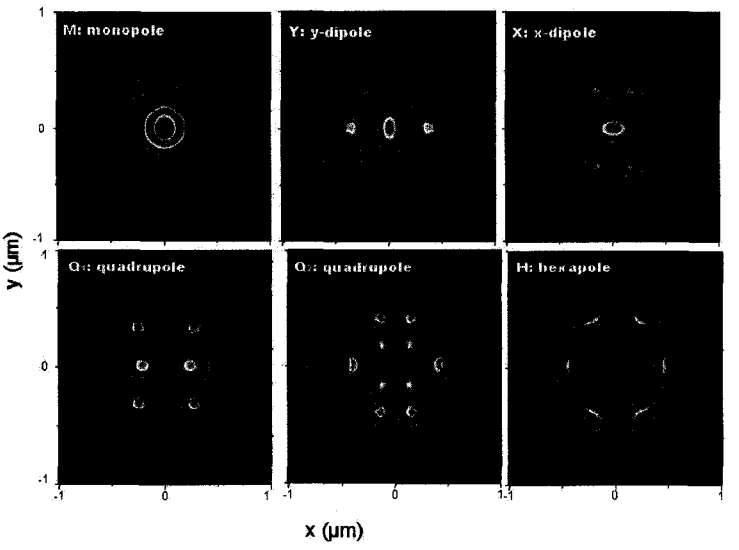

Figure 8.10: FDTD electric field intensity mode profiles of the various modes supported by a **H1S** microcavity.

δ_i=40 nm, a=500 nm, and d=231.5 nm obtained with the FDTD techniques discussed in section 5.6.2. Those modes are selected based on their energy, with respect to the photonic band gap energy and with the energy of the modes observed in photoluminescence. Typical PL of an **H1S** cavity with an embedded ensemble of QDs for r_i=176.7 nm, r=199.4 nm, δ_i=50 nm, a=500 nm, and d=223.5 nm is shown in figure 8.11(**a**). Fig.8.11(**b**) and (**c**) introduce detailed PolPL data for the same sample but plotted as a waterfall of the different PL spectra and as the peak integrated intensity as a function of the PL polarization angle with respect to the x-axis of the PhC.

The y-dipole is polarized along the y-axis just like for the **H1** microcavity while the x-dipole polarization dependance is blurred by its proximity with the photonic valence band edge. As predicted by simulation, modes $\mathbf{Q_1}$ and $\mathbf{Q_2}$, the quadrupole modes, are polarized along the y-axis. The less defined polarization of $\mathbf{Q_2}$ may be

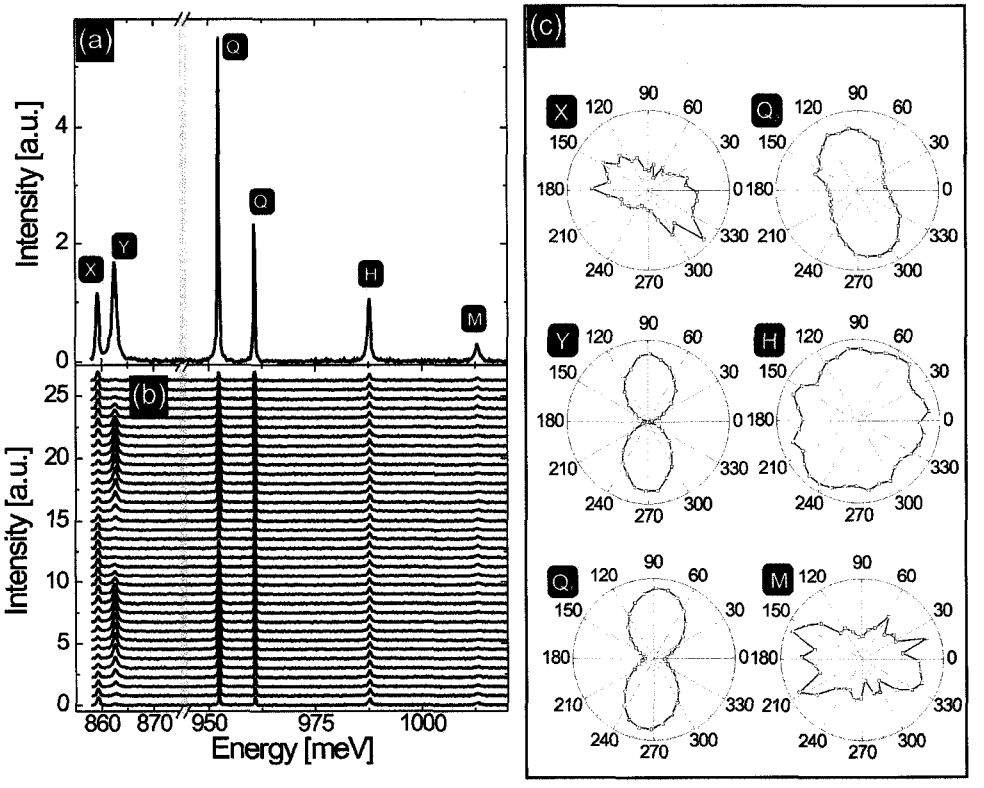

Figure 8.11: **(a)** Typical PL, **(b)** typical PolPL, and **(c)** typical PolPL data for a **H1S** microcavity where r_i=176.7 nm, r=199.4 nm, δ_i=50 nm, a=500 nm, and d=223.5 nm

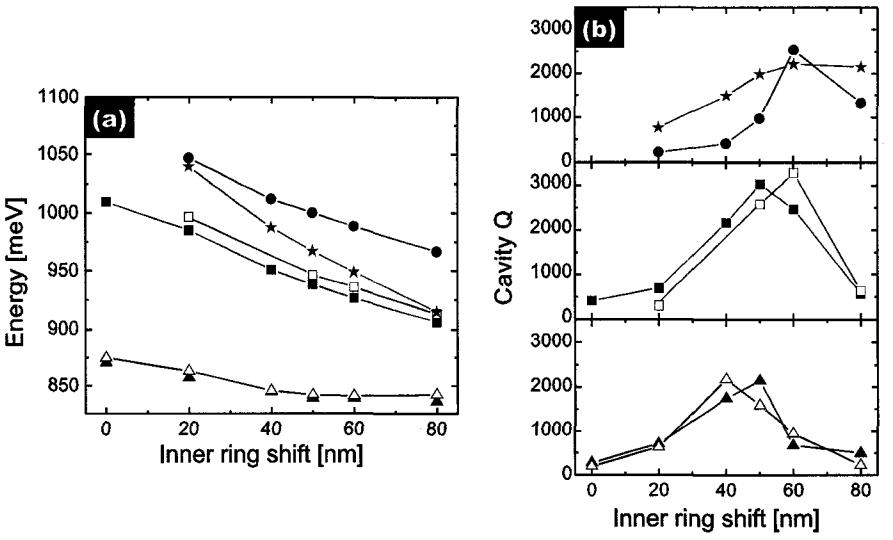

Figure 8.12: Mode peak energy **(a)** and Q -factor **(b)** as a function of the inner ring shift in (δ_i) for a **H1S** PhC microcavity with r=175 nm, r_i=156 nm a=500 nm, and d=231.5 nm. Filled (empty) triangles are the x-dipole (y-dipole), filled (empty) squares the $\mathbf{Q}_1$ ($\mathbf{Q}_2$) mode, stars are the hexapole modes and circles are the monopole mode.

attributed to defects in the hole lattice; $\mathbf{Q}_2$ being more affected because a larger portion of its electric field overlaps with the hole edges. The hexapole mode **H** and monopole mode **M** are unpolarized and may be interesting due to their potentially high Q.

By repeating the detailed PL and PolPL measurements presented in Fig.8.11 for multiple microcavities with different δ_i and r_i I can extract which **H1S** microcavity configurations yield high Q modes. The extracted mode peak energies and Q-factors as a function of the inner ring shift (δ_i) are presented in Fig.8.12 for a fixed inner ring radii (r_i) equal to 156 nm and as a function of r_i for δ_i=40 nm in Fig.8.13. In both figures the x- and y-dipole-like mode are represented by filled and empty triangles

respectively whereas Q_1 is filled squares and Q_2 empty squares. The circles and stars displays the monopole and hexapole modes, respectively.

The Q for all modes exceeds 2000, but for different **H1S** parameters; a Q-factor substantially larger than that for the **H1** design. As for the **H1** cavity, an asymmetric perturbation to the microcavity is present, producing x- and y-dipole-like mode maximum Q values at differing energies and removing the degeneracy. The highest Q (3 800) is reached by the monopole mode and, as its name suggests, it would be good at first sight to couple to a SQD because all its electric field is concentrated along a single antinode. Unfortunately, the single pole is not a single anti-node at the center of the PhC defect but is in a ring-like shape away from the center, not ideal to couple to a SQD. The $\mathbf{Q}_1$, $\mathbf{Q}_2$, and **H** are also not suitable for the same reason. Instead of further enlarging the **H1S** defect, we try to modify the **H1** defect in an asymmetric fashion to optimize the x- or y-dipole-like mode Q, as shown in the next sections.

8.2.3 Y-Dipole Optimization

Enlargement of the H1 Microcavity Along the x-Axis

Instead of changing the properties of all the holes within the first ring of air holes, we move only two holes on the x-axis synchronously by the amount δ_x in an **H1E** type microcavity. A positive value of δ_x means a shift away from the defect, towards the next lattice hole as is shown in Fig.8.14. An SEM image of an actual **H1E** device is presented in Fig.8.15(**a**) for δ_x=25 nm, r=145 nm, a=500 nm, and d=223.5 nm. Fig.8.15(**b**) and (**c**) introduce the electric field intensity mode profile for the y- and

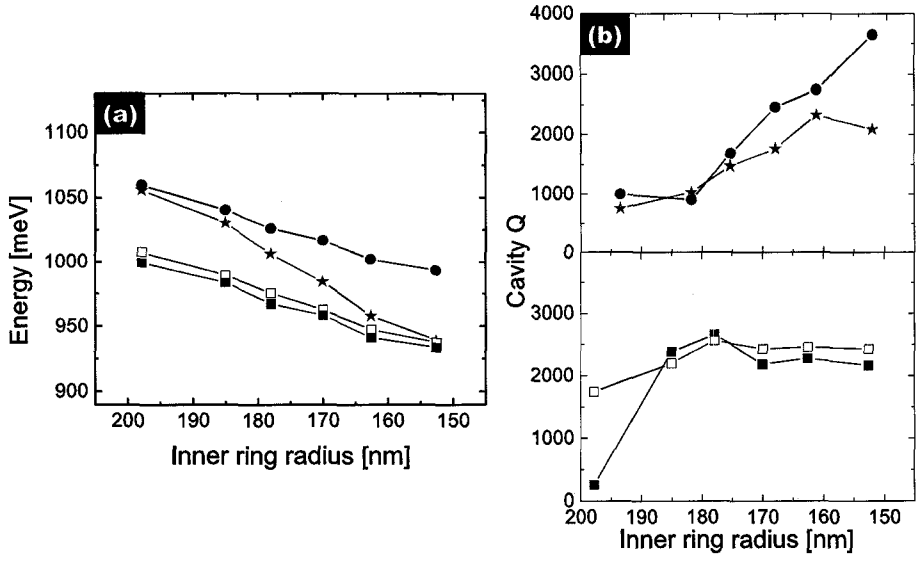

Figure 8.13: Mode peak energy **(a)** and Q-factor **(b)** as a function of the inner ring shift in (δ_i) for a **H1S** PhC microcavity with r=175 nm, δ_i=40 nm, a=500 nm, and d=231.5 nm. Filled (empty) squares are thee $\mathbf{Q}_1$ ($\mathbf{Q}_2$) mode, stars arethe hexapole modes and circles are the monopole mode.

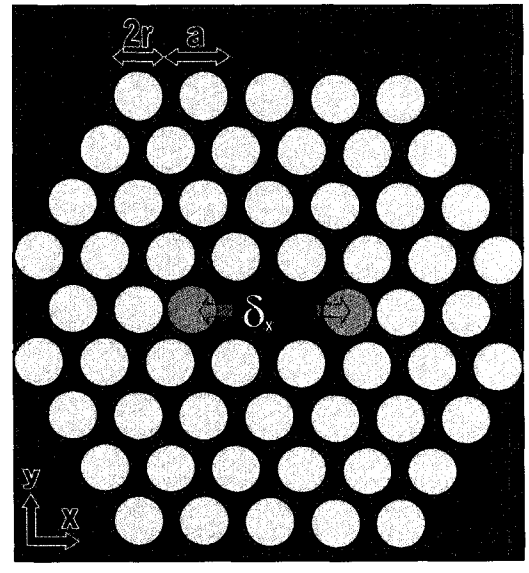

Figure 8.14: Schematic of an elongated single missing hole defect (**H1E**) in a triangular lattice of air holes.

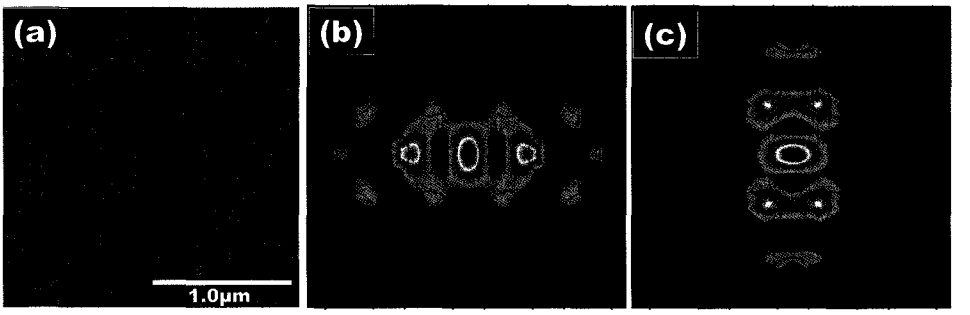

Figure 8.15: Typical **H1E** microcavity SEM **(a)**, and FDTD-obtained electric field intensity profiles for the y-dipole-like mode **(b)** and the x-dipole-like mode **(c)**

x-dipole-like modes of an **H1E** microcavity with δ_x=15 nm, r=165 nm, a=500 nm and d=223.5 nm as obtained by FDTD. While it is hard to notice any change within either of the mode profiles with respect to the ones of the **H1** microcavity, detailed analysis reveals changes for the y-dipole-like mode, and almost none for the x-dipole-like mode.

In figure 8.16Typical PL of an **H1E** microcavity with an embedded QD ensemble I measured for δ_x=75 nm, r=145 nm, a=500 nm and d=223.5 nm. The peak on the left is the y-dipole-like mode and the other one is the x-dipole. The insets show the PolPL data for each mode as a function of the polariser angle with respect to the PhC x-axis, which confirms the peak attributions.

Clearly, the Q-factor of the y-dipole mode is greater than the x-dipole Q. This can be qualitatively explained by the fact that the electric field of the y-dipole mode is stretched along the x-axis and the enlargement with δ_x provides more room for it to breathe and smooths the overlap between the mode and air-hole edges.

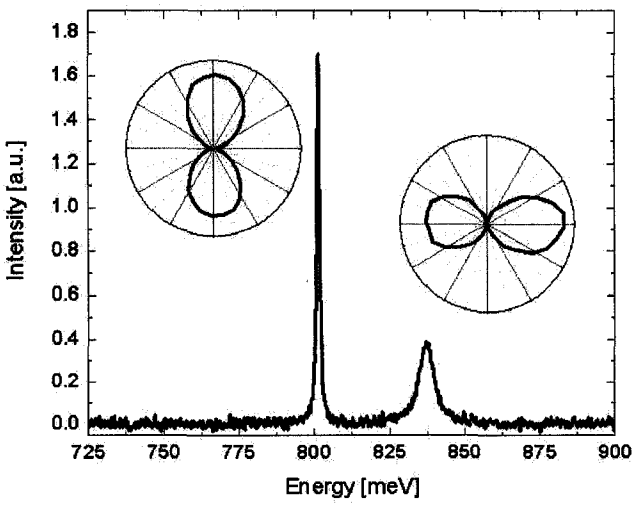

Figure 8.16: Room temperature PL from a **H1E** microcavity. The fabrication parameters for the cavity were: d=223.5 nm, r=145 nm, a=500 nm and δ_x=75 nm. Angular dependence with respect to the x-axis of the PL intensity for each mode is shown in the insets.

By repeating this experiment, including the PolPL, for different values of δ_x we can get a better understanding of the modal behavior with the defect enlargement. Figure 8.17(**a**) shows the peak energy shift as a function of δ_x. The plain triangles are experimental data points (r=145 nm, a=500 nm, and d=223.5 nm) whereas the connected empty squares represent FDTD calculations for **H1E** microcavities with varying δ_x and r=165 nm while the other parameters have the same value.

The agreement between experiment and simulation is quite good. In the Refs. [189, 226] the authors demonstrated that their Fabry-Pérot model correctly anticipates this behavior. The y-dipole-like mode shift in energy is accompanied by an increase in Q (Fig.8.17 (**b**)). The small discrepancy between the experiment and the simulation Q numbers can be attributed to slight imperfections in the hole sizes. A

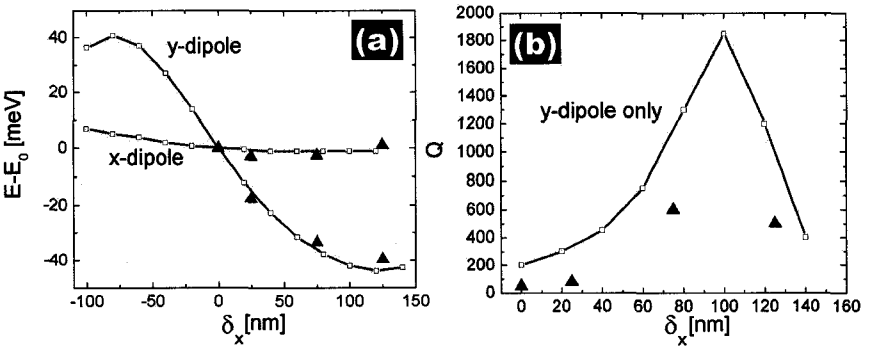

Figure 8.17: Peak shift **(a)** and Q **(b)** as a function the defect elongation (δ_x) for a **H1E** microcavity. Red lines with square symbols are the FDTD obtained numbers and the plain black triangles are experimental data points. r=145 nm for the experimental data and r=165 nm for the FDTD data while a=500 nm and d=223.5 nm for both.

H1E δ_x/a ratio around 1/4 resulted in a maximum Q value about 4000 for r=105 nm, a=441.8 nm, and d=280 nm (data not shown here). This would lead, for a perfectly matched single QD within the microcavity, to a Purcell factor of ≈600 given the calculated microcavity mode volume $V = 0.75(\lambda/n)^3$. As was explained in section 5.4, this means a microcavity still in the strong coupling regime. Again, one has to be careful while referring to such limits because they were calculated using typical InAs/InP QD parameters and assume perfect spatial and spectral overlap between the QD and the microcavity. This means a repetition rate almost 600 times higher than without a microcavity. Further degrees of freedom within the microcavity design, namely the PhC pitch (a), host lattice hole radii (r) and the membrane thickness (d), could be used to match the QD single exciton peak energy and the y-dipole peak energy if required. The important thing is to preserve the δ_x/a ratio to achieve the maximum Q. Other very interesting effects appear as δ_x is further enlarged: other modes appear and the y-dipole-like mode oscillates in peak energy and Q-factor.

Example of an Additional Mode

Cavity enlargement gives room for new modes to appear. I measured detailed PL for **H1E** with δ_x=75 nm, a=500 nm and d=223.5 nm for different r values (175 nm to 195 nm). Results are shown in figure 8.18(**a**) whereas (**b**) shows the FDTD-obtained electric field intensity profile for the same parameters as for the PL and r=185 nm.

Mode peak energy and Q as a function of δ_x for r=170 nm, a=500 nm and d=223.5 nm are presented in Fig.8.18(**c**) while (**d**) has a fixed δ_x=75 nm and the hole radii are varied with the same d and a. In Fig.8.18(**c**), the Q-factor rises to almost 3 000 and then quickly drops again. This high Q is promising but, just as for the monopole mode of the **H1S** microcavity, the mode electric field does not have an antinode at the defect center, making it an unsuitable candidate to generate a single photon source and match key parameter (*ii*).

Triple Missing Hole (H3)

A schematic representation of a triple missing hole microcavity, **H3**, is shown in Fig.8.19. This type of microcavity has been extensively studied [189, 224–229]. The QD community used it as a high Q microcavity to which SQDs are coupled and such cavities have reached the strong coupling regime [3, 144, 230, 231]. However, we were the first to produce a InAs/InP-based **H3**. Typical modifications to the **H3** microcavity to obtain higher Q are shrinking the x-axis edge holes and/or moving them

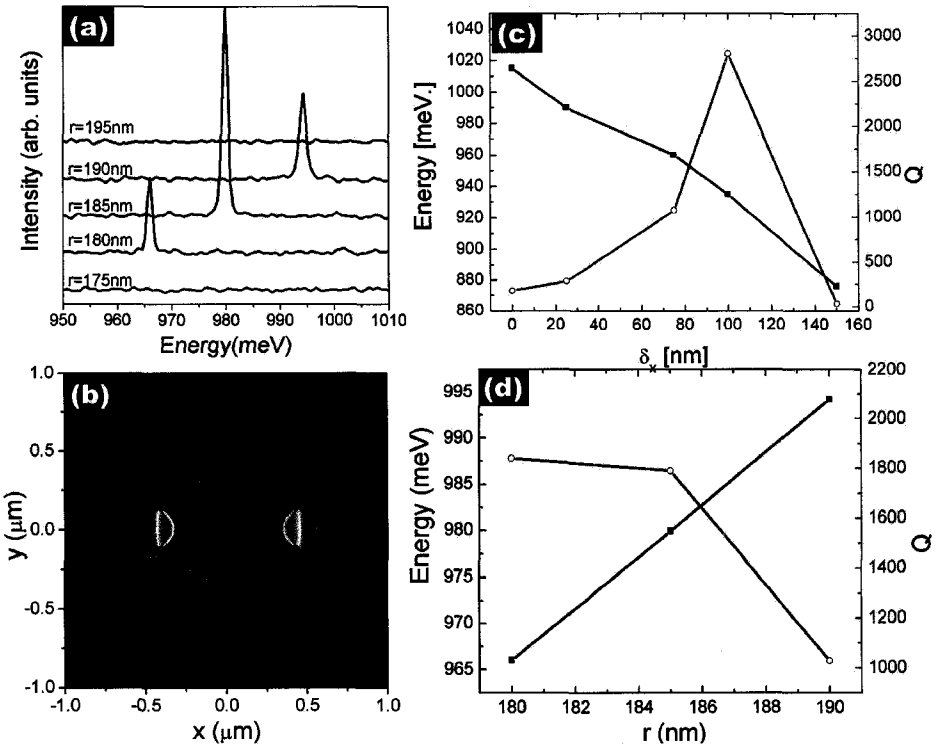

Figure 8.18: Experimental results for the additional high energy mode with fixed a=500 nm and d=223.5 nm. **(a)** PL data for different r values with δ_x=75 nm. **(b)** Electric field intensity mode profile obtained by FDTD for r=185 nm and δ_x=75 nm. Mode peak energy and Q-factor as a function of δ_x for r=170 nm **(c)** and as a function of r for a fixed δ_x=75 nm. Filled circles are experimental data points while the empty circles are FDTD-obtained. From [222]

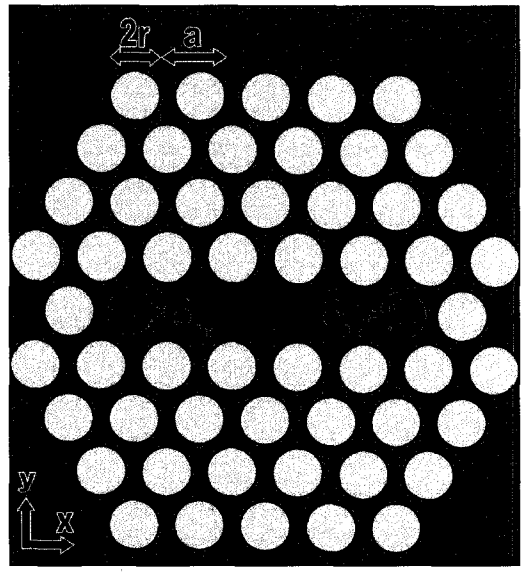

Figure 8.19: Schematic of a triple missing hole defect (**H3**)

along the axis (δ_{3x}). A positive value of δ_{3x} represents the shift of the x-axis edge holes outwards along the axis. In reference [224] we presented such a study.

In Fig.8.20 we show detailed experimental results I performed in PL and PolPL for a simple **H3** microcavity. The peaks are labeled from **A** to **E** in order of peak energy. Each can be linked to their FDTD-obtained mode profile in figure 8.21 with the same label. The symbol in the bottom right corner of each plot represents the mode polarization dependance from simulation data. Slight variations of δ_{3x} result in a Q-factor increase for the mode **A**. We achieved Q-factors of $\approx 7\,500$ for the **A** mode of the **H3** microcavity for δ_{3x}=65 nm. Considering the mode **A** mode volume is $\approx 0.75(\lambda/n)^3$, this microcavity-QD coupling is outside of the weak coupling regime. Of course, an imperfect spectral and/or spatial overlap will produce weaker coupling, so that a higher Q-factor microcavity gives a "cushion" to work with while fabricating

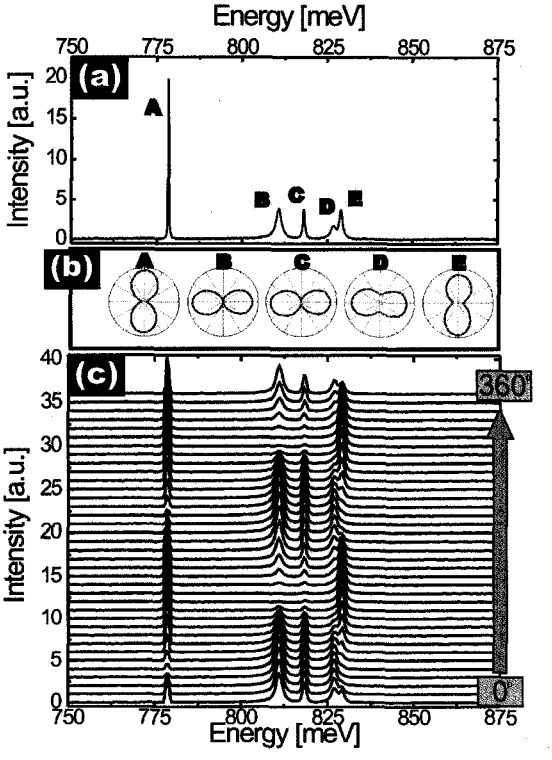

Figure 8.20: **(a)** PL, **(b)** PolPL polar plot, and **(c)** PolPL for a **H3** microcavity with r=105 nm, a=441.3 nm and d=280 nm.

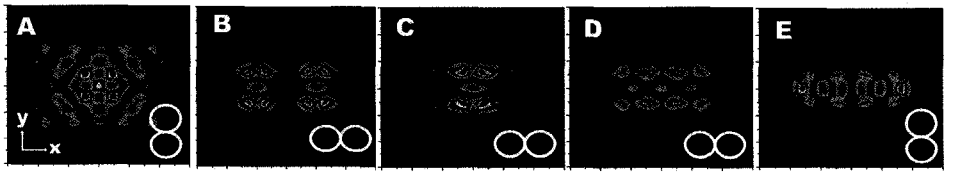

Figure 8.21: FDTD-obtained electric field intensity mode profile for a **H3** microcavity with δ_{3x}=0 nm and **(b)** δ_{3x}=65 nm

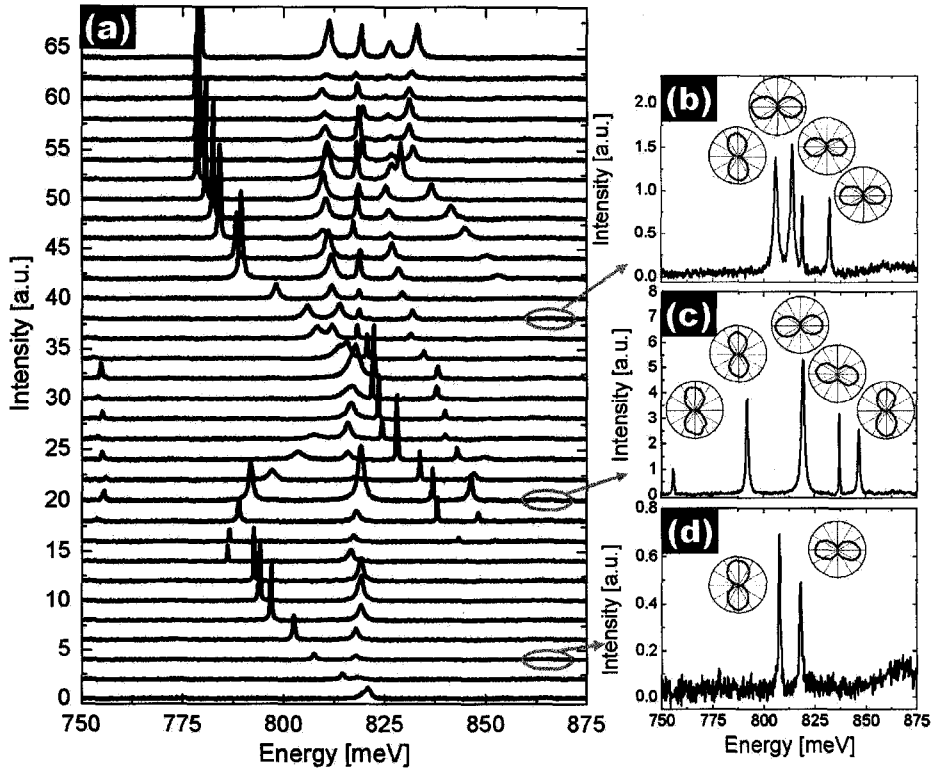

Figure 8.22: **(a)** Modified **H1** microcavities PL spectra for r=105 nm, a=441.1 nm, d=280 nm, and different δ_x values. Curves are offset for clarity. High resolution PL and PolPL for δ_x =30 nm **(b)**, δ_x =155 nm **(c)** and δ_x =300 nm **(d)**.

a SP device.

H1 to H3

To further our understanding of the mode structure of the **H3** microcavity, especially the high Q mode **A**, I increased the **H1E** δ_x from zero to more than a. This is the first report of such a study of the modal behavior going from a **H1** microcavity to a **H3**. Figure 8.22**(a)** shows PL spectra for multiple microcavities with increasing δ_x values

and fixed r=105 nm, a=441.1 nm, and d=280 nm. The defect is enlarged to the point that the shifted holes reach and pass the next host lattice hole positions, making the cavity an **H3** microcavity. In total, three modes appear from the "conduction band" (the higher energy side of the photonic band gap). Another one comes out of the valence band for a δ_x value approximately equal to the one generating a maximum y-dipole mode Q as presented earlier ($\delta_x \approx 110\,nm \approx a/4$) and goes back out on the same energy side when the y-dipole mode comes back to its original value.

As was done with previous microcavity designs, I performed high resolution PL and PolPL at different δ_x values in order to correctly attribute each peak to a specific mode and follow its behavior with defect enlargement. Examples of such measurements are presented in Fig.8.22(**b**) for δ_x =30 nm, (**c**) δ_x =155 nm and (**d**) δ_x =300 nm. The polarization is taken with respect to the PhC x-axis.

The peak energy positions as a function of δ_x are presented in figure 8.23 where the experimental data points are connected by a line to guide the eye. At each step of δ_x the nearest peak in energy with the same polarization as a previous peak is connected by a line to it. The modes are labeled using the mode labels defined in the previous section with respect to the **H3** microcavity mode.

The mode behavior is quite interesting. The initial decrease in energy for the y-dipole-like mode while the x-dipole-like mode remains unshifted was already discussed earlier in section 8.2.3. The y-dipole returns to the x-dipole energy for $\delta_x \approx 220\,nm \approx a/2$. This was also predicted by the Fabry-Pérot model and is

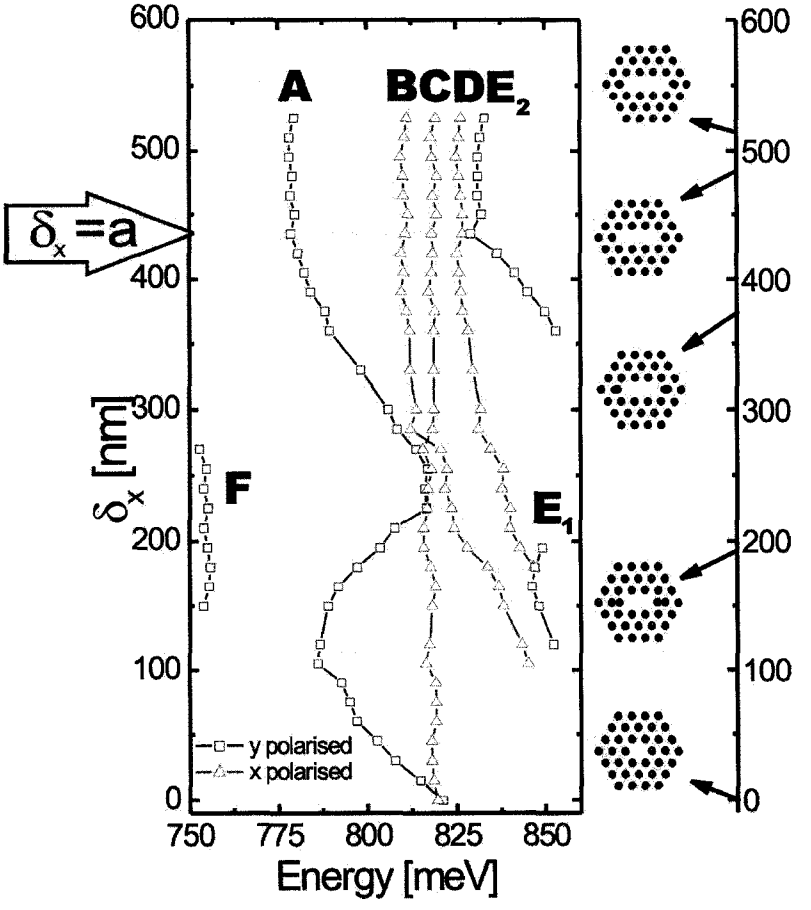

Figure 8.23: Peak energy as a function of δ_x. Black squares (red triangles) designate modes polarized along the y-axis (X-axis). Lines are guides to the eye.

confirmed by FDTD results [189]. Similar effects were also predicted by the perturbation theory in Ref. [226] with less accuracy.

Further enlargement of the microcavity leads the **H1E** microcavity towards an **H3** microcavity. As δ_x increases again the y-dipole-like mode (labeled **A** in Fig.8.23) shifts back again to lower energy. Meanwhile, two other modes labeled **B** and **D** and polarized along the x-axis, appear at higher energy from the conduction band. They both stabilize at an energy around the x-dipole-like mode, *i.e.* mode **C**.

Oscillations similar to mode **A** are seen for mode **E** (combo of $\mathbf{E}_1$ and $\mathbf{E}_2$) and **F** except they are lost in the photonic band edges for some δ_x values. Their existence can be straightforwardly explained by the Fabry-Pérot model as modes with higher and lower integer number in equation (5.74). It is also worth noting that the mode $\mathbf{E}_1$ is in fact the additional mode discussed in section 8.2.3.

The peak energies stay relatively constant as $\delta_x > a$, *i.e.* the shift is larger than the pitch. This is because the holes limiting the defect size along the x-axis are now the second ring lattice holes. As will be seen later the minimal change in peak energy does not mean that the Q-factor is not influenced by δ_x anymore. The presence of the hole greatly affects the properties of the PhC mirror.

The mode **A** can be attributed to the y-dipole-like mode because of its behavior as a function of δ_x and because of its polarization dependance. A plot of mode **A** peak energy and the Q as a function of δ_x is shown in figure 8.24. The Q clearly follows the

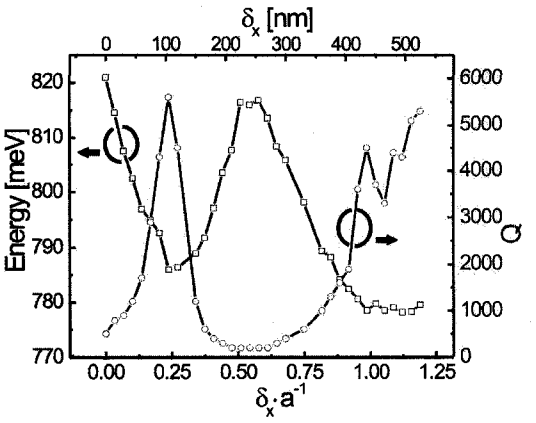

Figure 8.24: PL data extracted y-dipole-like mode peak energy and Q as a function of δ_x for r=105 nm, a=441.1 nm and d=280 nm. Empty black squares are peak energy data points while empty red circles are the experimental Q-factors

peak energy (E_{peak}) behavior with δ_x, increasing when E_{peak} decreases and decreasing when it goes up. The pitch for all measurements is fixed to 441.1 nm while the hole radii is 105 nm and the membrane thickness is 280 nm. The initial fall and rise of the mode peak energy and the opposite change for the Q-factor were already hinted at in Fig.8.17. The peak Q-factor is reached for $\delta_x \approx a/4$ while the mode returns to a low Q value for $\delta_x \approx a/2$. The Q goes as high as 5 600, much higher than the highest one shown in Fig.8.17 for the **H1E** microcavity. The larger Q occurs because of a better-suited membrane thickness and hole pitch. The mode peak energy falls again (as the Q rises) as δ_x approaches a.

Equation (5.75) of the Fabry-Pérot model enables a more intuitive interpretation of the behavior. The key parameters are the PhC mirror reflectivity $|r(\lambda_0)|$, the mode group index $n_g(\lambda_0)$ (related to the group velocity $v_g(\lambda_0) = c/n_g(\lambda_0)$) and the modal

penetration depth $\left(\frac{\partial\phi_r}{\partial\lambda}\right)_0$ (derivative of the mirror modal phase shift). The three main parameters increase with the outward shift δ_x, reach a maximum and then decrease [189].

The reflectivity rises and falls earlier than the other two, which are synchronized. This means that two different mechanisms are involved. The first one can be understood as a mode conversion in the non-periodic region of the mirror [232, 233]. The propagative PhC mode conversion into an evanescent PhC mirror mode is made easier and then harder by changing the edge hole positions. For the second mechanism, the change in $n_g(\lambda_0)$ results from the highly dispersive nature of the PhC propagation mode and the break up in the periodicity condition of the photonic crystal results in modifications in the penetration depth within the sample $\left(\frac{\partial\phi_r}{\partial\lambda}\right)_0$. This effect is linked with slow-wave effects. It is limited here because of the limited size of the microcavity. Longer microcavities provide slower light and could make for exciting experiments [189, 234].

The second rise of the Q (when **H1E** becomes a **H3** microcavity) is also predicted by the Fabry-Pérot model and the same two mechanisms can be invoked to interpret the results. The slow-wave effect will be stronger here since the microcavity is larger. The y-dipole-like mode Q-factor for $\delta_x > a$ is quite interesting. After the initial decrease, it rises again when the shifted hole detaches itself from the second ring, fixed lattice hole, while the mode peak energy steadily decreases. Since we did not calculate the Fabry-Pérot model and the group of Sauvan and Lalanne never explored such a structure, it is hard to explain this behavior directly but it is clear that the hole

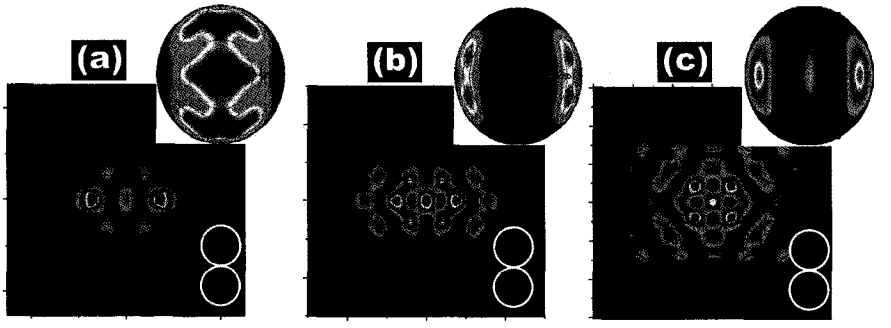

Figure 8.25: FDTD-obtained electric field intensity mode profile with the polarization dependance and far-field distribution y-dipole-like mode as insets in lower-right and upper-right corners for a **H1E** y-dipole-like mode microcavity with δ_x = **(a)** 0 nm, **(b)** $a/4$ and **(c)** a.

penetrating within the lattice will affect the PhC mirror while keeping the effective defect length equal or shorter to the **H3** case, strongly suggesting an effect due to the first mechanism.

Moving to the modes with opposite polarization, the behavior of the three x-polarized modes in Fig.8.23 is relatively simple to explain qualitatively. They are single, double and triple x-dipole-like modes: mode **C**, **B** and **D**, respectively. The x-dipole-like mode field is concentrated along the y-axis and the enlargement along the x-axis barely affects it, but as the space along the x-axis becomes larger, two x-dipole-like modes can co-exist side by side. Mode **B** (the double x-dipole) appears when the total defect length along the x-axis is about $\frac{3a}{2}$ whereas mode **D** (triple x-dipole) appears when the total length is $\sim \frac{9a}{5}$. As both of them are given more room to breath they will stabilize to an energy similar to that of the x-dipole-like mode.

To study in greater detail the behavior of the y-dipole-like mode, FDTD simulations of the electric field intensity mode profile, polarization dependance and far-field dependance were done for δ_x =0 nm, $a/4$ and a (Fig.8.25). While the mode profile changes, the polarization is still along the y-axis, perpendicular to the PhC defect elongation. The more drastic change is in the far-field distribution. The defect enlargement yields a microcavity y-dipole-like mode with almost zero radiation straight upwards. The light goes sideways, along the y-axis. This inconvenient behavior (from an application perspective) gets worse as modifications are made to the **H3** microcavity to increase its Q. For an **H3** microcavity design, the higher the Q the harder it becomes to collect the photons emitted by the microcavity and insert them into an optical communication channel.

Half-H3 Microcavity (H1Y)

Going back to the y-dipole-like mode peak energy and Q as a function of δ_x in Fig.8.24 it is clear that the Q-values reached at $\delta_x \approx a/4$ are quite similar to those at $\delta_x = a$. Instead of optimizing the sizes and positions of the holes surrounding the defect for **H3**, the optimization procedure was applied to the **H1E** with $\delta_x = a/4$. Similar results can be reached, *i.e.* a high Q microcavity but with an even smaller mode volume. This type of microcavity will be referred to as the **H1Y** microcavity and its schematic is presented in figure 8.26(**a**). The key parameters are: δ_x, δ_4 the shift of the other four holes adjacent to the defect along the crystallographic-like lines, and r_4 the radii of those four holes [227]. A positive value of δ_4 means the 4 holes are shifted away from the defect.

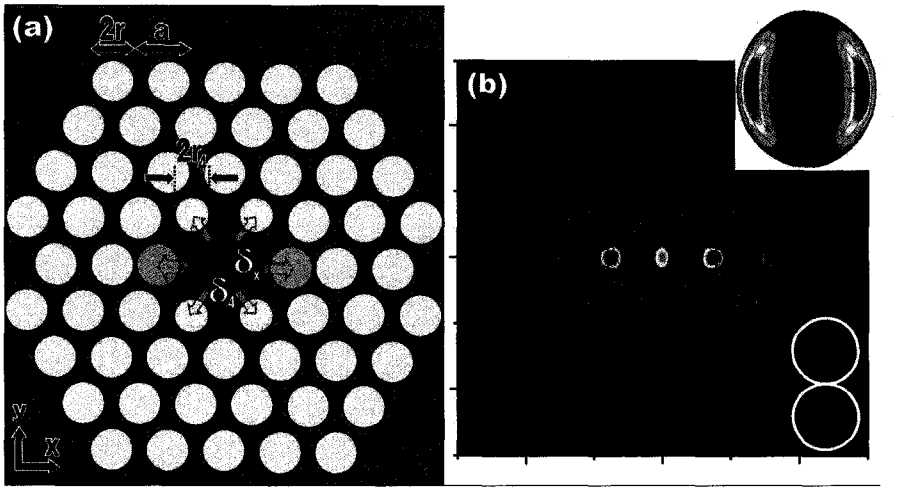

Figure 8.26: **(a)** Schematic of an modified single missing hole defect to optimize the y-dipole-like mode (**H1Y**). **(b)** FDTD-simulation-obtained electric field intensity mode profile, polarization dependance and far-field pattern for δ_x=80 nm, δ_4=17.3 nm, r_4=85 nm, r=105 nm, a=441.3 nm and d=295 nm.

Figure 8.26**(b)** shows a simulation result for a **H1Y** microcavity with δ_x=80 nm, δ_4=20 nm, r_4=85 nm, r=105 nm, a=441.3 nm and d=295 nm. The mode profile shows a y-dipole-like mode profile with an anti-node centered in the defect and the insets show a preserved polarization dependance while the mode far-field radiation has less vertical radiation. This particular design yields a $Q \approx 20\,000$ and a mode volume equal to $\approx 0.5(\lambda/n)^3$. These numbers mean a coupling regime far outside weak coupling. The emission rate improvement would no longer be related to the microcavity Purcell factor and could potentially be lower than in the weak coupling regime.

8.2.4 X-Dipole Optimization

Exploratory work was done by the Vučković group in the PhC microcavity design to optimize the x-dipole-like mode, *i.e.* a high Q-factor while preserving a field antinode

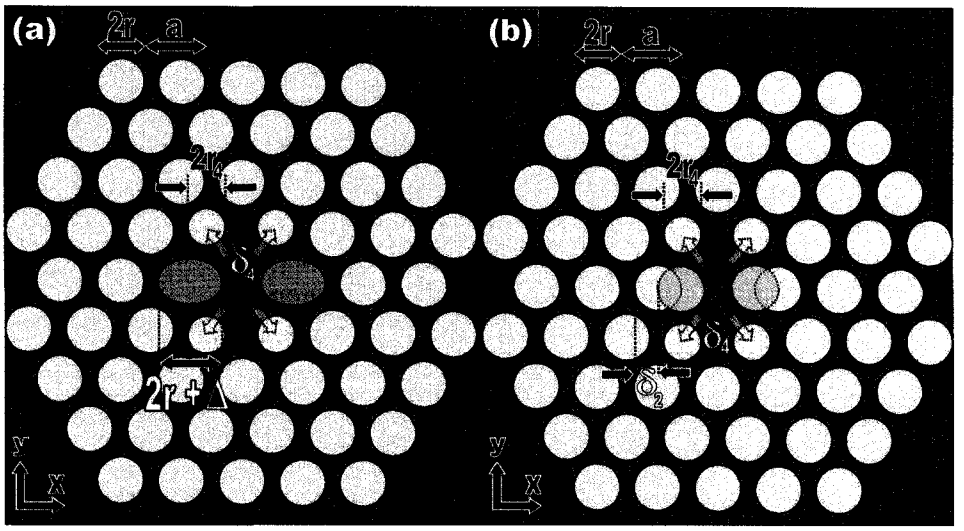

Figure 8.27: Schematics of modified single missing hole defect to optimize the x-dipole-like mode. **(a)** The original design introduced by Vučković and Yamamoto [235] and **(b)** **H1X** design

at the center of the PhC defect [3, 235–238]. Their resulting design is shown in figure 8.27**(a)** while our version of their design (**H1X**) is presented in **(b)**. Their large ellipses are replaced by two overlapping holes separated by δ_2, in order to ease the PhC fabrication: the ellipse edges along the long axis are not developed properly after electron-beam exposure because they are too narrow and do not allow easy access for chemical etchants. Since the ellipse length is crucial in this design, replacing it by two overlapping holes provides similar results. As in the previous section, the other 4 holes adjacent to the defect are moved radially outwards by δ_4 and reduced in size (radii=r_4). A positive value of δ_4 means a shift away from the defect while a positive δ_2 means the two additional holes are moved inwards along the x-axis, *i.e.* enlarge the ellipse. While our design is similar to theirs, we explored to much deeper extent the parameter space and produced microcavities of higher quality. Figure 8.28**(a)** introduces the electric field intensity mode profile of the x-dipole-like mode for an **H1X**

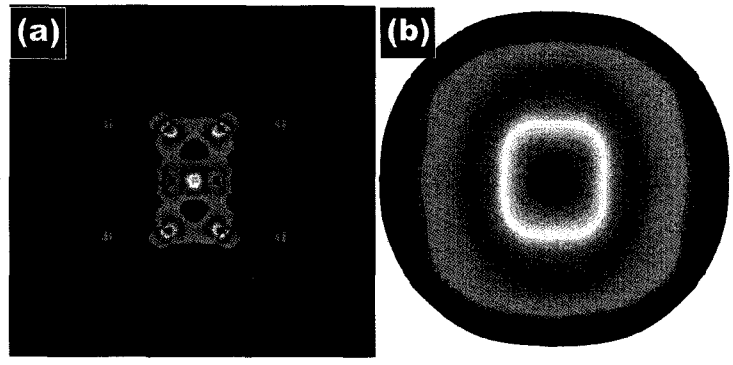

Figure 8.28: FDTD-obtained electric field intensity mode profile **(a)** and far-field pattern **(b)** for a **H1X** microcavity with δ_2=180 nm, δ_4=15 nm, r_4=105 nm, r=130 nm, a=441.3 nm and d=295 nm

cavity with δ_2=180 nm, δ_4=15 nm, r_4=105 nm, r=130 nm, a=441.3 nm and d=295 nm while **(b)** shows the corresponding far-field pattern. The microcavity modifications leave the x-dipole-like mode with an antinode at its center and a significant portion of the emission vertical. In figure 8.29**(b)** I introduce typical **H1X** PL results with δ_2=150 nm, δ_4=20 nm, r_4=95 nm, r=120 nm, a=441.3 nm and d=295 nm while subfigure **(a)** shows an SEM image for the same r, a and d but with δ_2=180 nm, δ_4=5 nm and r_4=105 nm.

The PL shows the sharp line of the **H1X** x-dipole-like mode and the other mode present at lower energy is the y-dipole-like mode as confirmed by its polarization dependance. The x-dipole Q-factor for this microcavity is already higher than 3 000.

Obviously, the parameter space with such a microcavity design is quite large. First, the influence of δ_4 is explored in figure 8.30. PL spectra are shown for different δ_4 values while the other parameters are fixed to δ_2=150 nm, r_4=105 nm, and r=120 nm while a and d are the same values as with all the other results presented

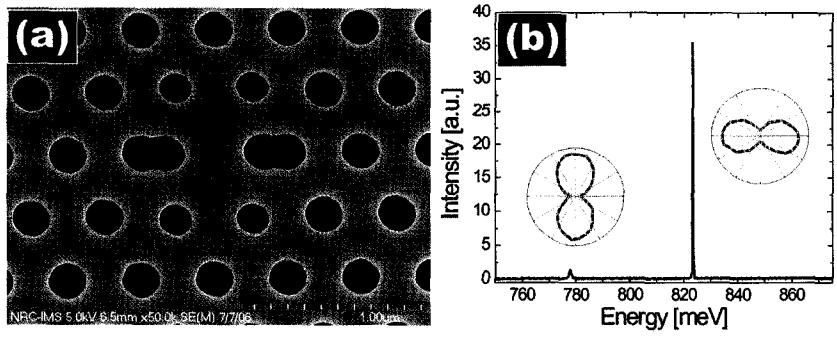

Figure 8.29: Typical **H1X** results. **(a)** SEM image for δ_2=180 nm, δ_4=5 nm, r_4=105 nm, r=120 nm, a=441.3 nm and d=295 nm. **(b)** PL and PolPL data for δ_2=150 nm, δ_4=20 nm, r_4=95 nm, r=120 nm, a=441.3 nm and d=295 nm

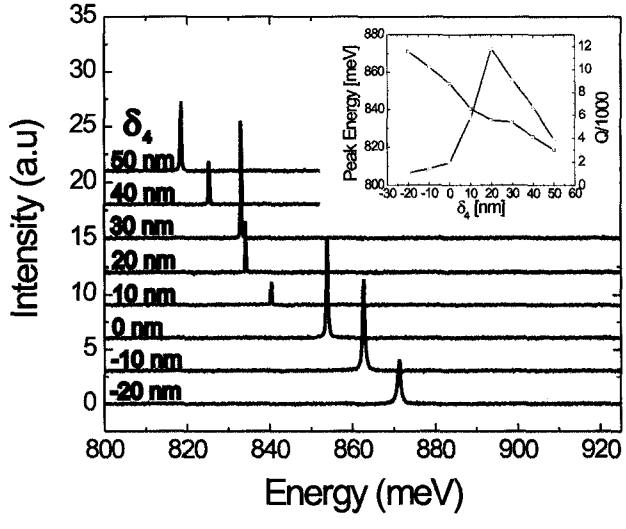

Figure 8.30: PL spectra for **H1X** with varying δ_x value and other parameters fixed: δ_4=150 nm, r_4=105 nm, r=120 nm, a=441.3 nm, and d=295 nm. Inset shows the peak energy values and Q.

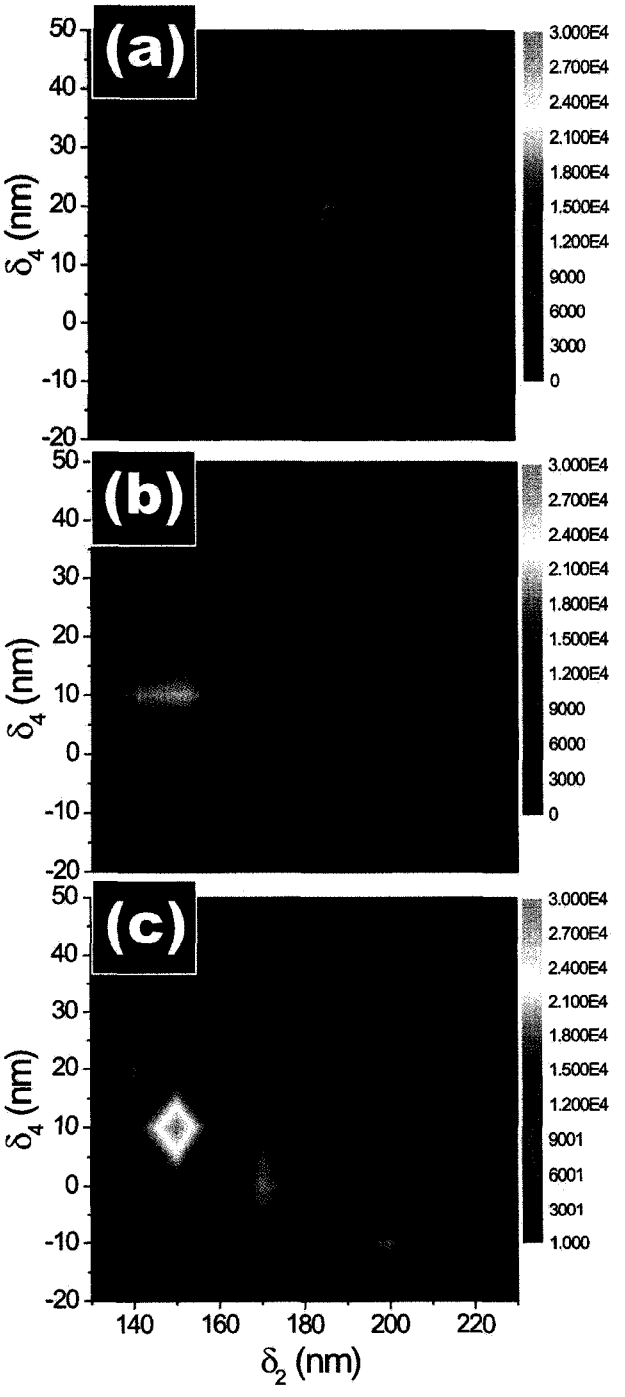

Figure 8.31: Contour plot of **H1X**-microcavity x-dipole-like mode Q as a function of δ_2 and δ_4 **(a)** r=120 nm and r_4=95 nm, **(b)** r=120 nm and r_4=85 nm, and **(c)** r=105 nm and r_4=85 nm while a and d are fixed to 441.3 nm and 295 nm. Each contour plot consists of at least 80 measurements.

thus far and will be fixed for the remainder of this section. The inset shows the extracted mode peak energy and Q-factor. The Q of the x-dipole-like mode reaches as high as 12 000. A more thorough, although not complete, exploration of the parameter space is presented as an intensity plot of the Q in Fig.8.31. Sub-figure **(a)** presents the Q as a function of δ_2 and δ_4 for r=120 nm and r_4=95 nm while **(b)** has the same r but r_4=85 nm. The third contour plot, Fig.8.31**(c)**, has r=105 nm and r_4=85 nm.

An optimal zone of the parameter space is clearly highlighted by the data. The ideal conditions yield a microcavity with a Q in excess of 28 000, the instrument measurement limit. This is our highest experimentally measured Q with any type of microcavity and much better than the best value achieved by Vučkovič *et al.* (Q ~5000). FDTD simulation of the same cavity gives a y-dipole-like mode with a centered antinode and ideal far-field pattern but a Q-factor around 70 000. In fact, such discrepancy is relatively small considering the Q can be expressed as:

$$\frac{1}{Q} = \frac{1}{Q_t} + \frac{1}{Q_i} \tag{8.1}$$

where Q_t is the theoretically predicted quality factor and Q_i is a measure of the mode coupling strength to the imperfections. A higher Q_i means a lower quantity of imperfections or at least a lower effect on the quality factor coming from them. Simple mathematics gives a Q_i=47 000 for this microcavity, a quite high value considering the fabrication requirements. By comparison, a microcavity with a predicted Q of 10 000 and a measured Q of 2 000 means a Q_i of 2 500. The **H1X** microcavity yields a high F_p (≈4100) microcavity well into the strong coupling regime. From the F_p derivation in 5.2.1 it is clear that a spatial and/or spectral mismatch will influence

the F_p to the lower side so that for an actual SQD-**H1X** microcavity system the real Purcell factor will be somewhat lower than predicted. It is worth noting, that the strong coupling regime was measured for an F_p as little as 36 for InGaAs interface fluctuation SQD in a GaAs matrix in a micropillar microcavity [239]. An F_p of 441 was the lowest for a PhC microcavity with an InAs/GaAs SQD [230].

8.3 Photonic Crystal Microcavity Results Compendium

In order to fabricate an efficient single photon source a list of 5 key parameters was introduced at the start of chapter 5. They were: (*i*) a high Purcell factor as defined by:

$$F_P = \frac{3\lambda^3}{4\pi^2}\frac{Q}{V}, \tag{8.2}$$

but not too high as to go out of the weak coupling regime, (*ii*) a good spatial overlap between the mode electric field intensity and the SQD, (*iii*) a good spectral overlap, (*iv*) a proper orientation of the SQD electric dipole moment with respect to the microcavity mode planarization, and (*v*) a far-field mode profile suitable to couple to an optical communication channel. Table 8.1 summarizes the different PhC microcavity designs explored with their different modes and how well they performed with respect to the key parameters.

The harder parameters to reach were (*i*), (*ii*) and (*v*). Our extensive study showed that the parameter (*ii*) is hardest to attain (other than the x- and y-dipole-like mode)

PhC microcavity	Mode	(i) Q_{MAX}	F_p	(ii)[1]	(iii)	(iv)[2]	(v)
H1	x-dipole	600	90	YES	YES	YES	YES
	y-dipole	850	130	YES	YES	YES	YES
H1S	x-dipole	2200	300	YES	YES	YES	YES
	y-dipole	2200	300	YES	YES	YES	YES
	$\mathbf{Q}_1$ & $\mathbf{Q}_2$	3200	300	NO	YES	YES	(?)
	H	2000	210	NO	YES	YES	(?)[4]
	M	3500	440	NO	YES	YES	(?)
H1E	x-dipole	600	90	YES	YES	YES	YES
	y-dipole	5700	810	YES	YES	YES	YES
	E	2900	360	NO	YES	YES	(?)
H3[3]	y-dipole	8000	860	YES	YES	YES	NO
H1Y	y-dipole	5700	810	YES	YES	YES	YES
	y-d. simul.	22 000	2800	YES	YES	YES	YES
H1X	x-dipole	27 500	4100	YES	YES	YES	YES

Table 8.1: Compendium of the PhC microcavities. (i) to (v) refer to the key parameters for a single photon source (see table 5.1).

[1] The spatial overlap key parameter is good for all the microcavities because modifying the a and r while keeping the ratios for the other parameters would enable mode wavelength adjustments.

[2] The QD electric dipole is always fulfilled because even if our SQD have preferred orientation (i.e. not puck-like or asymmetric stress) it would be possible to measure it prior to microcavity construction around it and compensate for it.

[3] Only the y-dipole mode of the **H3** was studied because the other modes field distribution is wider and/or had no anti-node at the microcavity centered.

[4] For some microcavity design the far-field pattern was not measured.

and when it was achieved, the effective mode volume was increased. Our attention was thus centered on optimizing the Q-factor of either the x- or y-dipole-like mode. The Q-factor of the y-dipole could be increased by enlarging the **H1** microcavity to a **H3** microcavity but such a larger microcavity resulted in an unsuitable far-field distribution. A subsequent, more complex design (**H1Y**), involving a smaller enlargement along the x-axis was proven theoretically to also produce a high Q for the y-dipole-like mode but at the expense of an unsuitable far-field. The **H1X** design, based on the work by Vučković *et al.* [3], yielded the best result; better matching the key parameters and also producing a Purcell factor of over 4 000.

8.4 Post-Fabrication Tuning

Throughout this chapter, discussions have focused on key parameters (i), (ii) and (v) *i.e.* the mode Purcell factor (quality factor and effective mode volume), spatial overlap between the SQD and the mode electric field, and the far-field radiation pattern. Parameter (iv), the spectral overlap between the SQD and the microcavity mode will now be considered. Even if the microcavity mode peak energy is designed to match the SQD perfectly, imperfections linked to the fabrication process are inevitable. The precision in microcavity energy required to achieve a good coupling is a fraction of a mili-electron volt. Therefore a means to tune the microcavity after fabrication is highly desirable.

Such a technique, called digital etching, was developed within our laboratory [220]. Although we developed this technique independently, a digital etching process was

reported a few months prior to our own publication by the group of Prof. Hu, although this was in a different material system (InAs/GaAs QDs) [240]. The digital etching technique will be described further below. We were the first one to apple it to an InP-based microcavity.

An alternative technique to tune the microcavities is the controlled formation of small oxidized regions of lower refractive index with an AFM tip [241]. The very high precision of the AFM enables very precise oxide formation. The much lower refractive index of the oxide enables the control of the mode energy. We did not explore this avenue because the lifetime of the oxidized region is unclear.

The membrane thickness can be changed by dry etching [242]. Only the thickness is affected because of the jet etch nature. This technique is quite limited because it creates edge roughness at the surface that induces losses due to photon scattering. Also, the effect of the membrane thickness on the PhC microcavity is limited. The other parameters such as the hole radii and hole pitch induce larger effects on the photonic bandgap. We did not try this technique because it is a rather ineffective way to tune the mode energy.

Another technique to tune the QD and PhC microcavity into resonance is to change the sample temperature. This results in a slight redshift of the QD emission lines (less then a nanometer) before it ceases to be atomic-like. This technique was the one used recently in the experiments showing Rabi splitting due to strong

coupling [210,211,230,231,239]. Recently, a technique to provide local heating to individual microcavities within the sample chip was published where the heat is created through resonant laser excitation of an adjacent PhC microcavity [243]. The laser absorption heats the microcavity and the heat transfers to the cavity with the SQD thus tuning the emission. The low tuning range of this technique means a complementary technique is required.

The possibility to regrow some material onto the PhC sample within the CBE growth chamber was explored with limited success. The idea was to reduce the hole size, in contrast to many other techniques that involve the removal of material. Unfortunately, the PhC membrane did not seem to be able to withstand the growth temperature necessary to add material (560°C).

Another technique to shift the mode energy by adding material has been developed [244]. It involves the controlled condensation of Xe or N_2 onto the sample at low temperature. A suitable arrangement of valves and precise control of the Xe (N_2) gas pressure flowing into the cryostat enables a repetitive and cumulative condensation process. The process produces condensation on the sample, resulting in total shifts of up to 4 meV (the precise numbers depend on the starting PhC microcavity design). This technique is very interesting, since it enables one to tune the microcavity whilst actually inside the cryostat. The process can also be performed in a repetitive fashion, since the condensate can be evaporated by warming up the sample. I believe this technique to be strong contender, but our cryostat was not equipped to perform similar experiments

Focused ion beam etching (or cutting) could be a useful tool to enlarge the holes on a hole by hole basis given that the beam can be controlled with at least a nanometer precision. No reference to such a technique being applied to PhC microcavity tuning has been published to our knowledge but our collaborators in Australia have used it to write PhC microcavities and waveguides inside chalcogenide glasses [245], so it is technically feasible.

The holes can be filled with a higher index material to tune the photonic crystal material. Even better, the holes can be filled with liquid-crystal material, and a voltage applied to tune the microcavity [246]. This technique has the drawback that these liquids would never survive at the low temperatures required for the SQD DOS to become atom-like and have a SP source. Moreover, even if a special "never-freeze" liquid-crystal material were developed, the applied field would directly affect the QD and shift its emission line at the same time.

Finally, the proximity of an optical fiber can also be used to tune the microcavity as was explained in section 6.3 and in section 8.5 our results confirm a reversible tunability. The following section describes our digital etching technique for InP in greater detail.

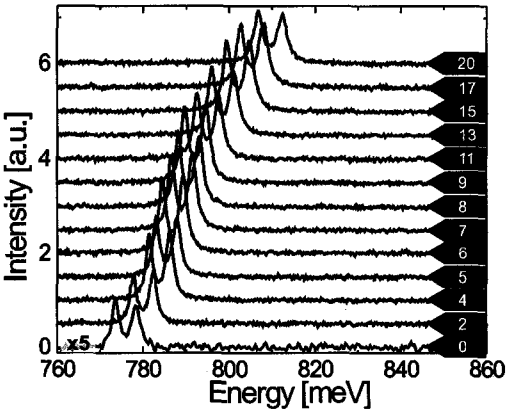

Figure 8.32: PL measurements of a **H1** microcavity as a function of the number of etch cycles. Curves are offset for clarity. From [220]

8.4.1 Digital Etching

This relatively simple technique consists of a repetitive removal of the native oxide layer at the surface of a sample. InP (or GaAs) when exposed to air will form a thin layer of oxide of finite thickness. The InP oxide composition is still under debate in the scientific community. It can be removed by an HF-based 7:1 buffered oxide etch; effectively removing material from the sample.

By this process the hole diameter will increase while the membrane thickness decreases. Because the natural oxidation process in air is relatively slow and potentially non-uniform, it is replaced with a 10 minute ultraviolet (UV)/ozone treatment. The oxidation/etching steps are repeated as required to tune the microcavity. Figure 8.32 shows the different PL spectra as a function of the number of etch cycles I measured for a simple **H1** microcavity. The mode peak energy and Q-factor extracted from

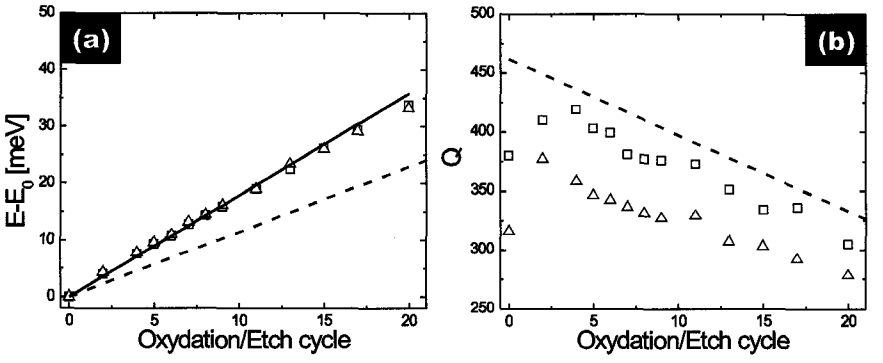

Figure 8.33: Peak energy and Q shift as a function of the number of etch cycles for the x- and y-dipole-like modes of a **H1** defect. Dotted lines are FDTD-simulation results considering a change of 0.65 nm in the hole radii per cycle and plain lines are FDTD-simulation results for the same change in hole radii plus a change in thickness of 0.75 nm.

this figure are presented in figure 8.33(**a**) and (**b**) by empty squares and triangles for the x-dipole-like mode and y-dipole-like mode respectively. To extract the change per cycle for the hole size and membrane thickness, the experimental data was compared to simulation. The dashed line is the FDTD-obtained mode peak energy and Q values if only a change of 6.5 Å per cycle in the hole radii is considered. This number was chosen to match the slope of the experimental points in Q. The plain line is also a simulation result but this time assuming an increase of 6.5 Å in hole radii and a decrease of 7.5 Å in thickness per cycle. The resulting fit will be used to tune the microcavity to the dot energy. This technique is limited mainly by four factors: 1- as the name says, it is a digital technique and one cannot reliably perform a 3 Å etch, 2- the tuning is unidirectional (if one overshoots the target energy, the sample is lost), 3- the etch is global for the whole sample (for many different microcavities on the same sample, different post-fabrication tuning would be required), and 4- the process

can not go on forever *i.e.* at one point the holes become too big, start to overlap and the membrane collapses.

8.5 Silica Nanowire Evanescent Field Coupling

In section 6.3 the silica nanowire evanescent field coupling technique was introduced. I will now discuss our experimental results, performed in collaboration with our colleagues at the University of Sydney. The silica nanowire used in this work is the result of two carefully fabricated fiber tapers on the same fiber. A fiber taper is basically an optical fiber with a slowly decreasing diameter. The fiber core is diluted and lost within its cladding during the diameter reduction. The light propagating within the silica fiber will stay inside if the fiber diameter is reduced slowly enough. For a small end-diameter (around and below 1 μm) the waveguided mode will have a significant portion propagating outside the silica. To probe the mode structure of a PhC microcavity (or other microcavity types as highlighted by previous studies [247–249]) a broadband light source is coupled into the fiber and passes through the nanowire. The transmitted light is measured as a function of the distance between the microcavity and the nanowire. Each microcavity mode to which the nanowire is coupled generates a dip in the transmission. This technique is now routinely used for advanced experiments measuring the Q of microdisc microcavities on a chip [250–252] and to measure the emission properties of a SQD in a microcavity [253].

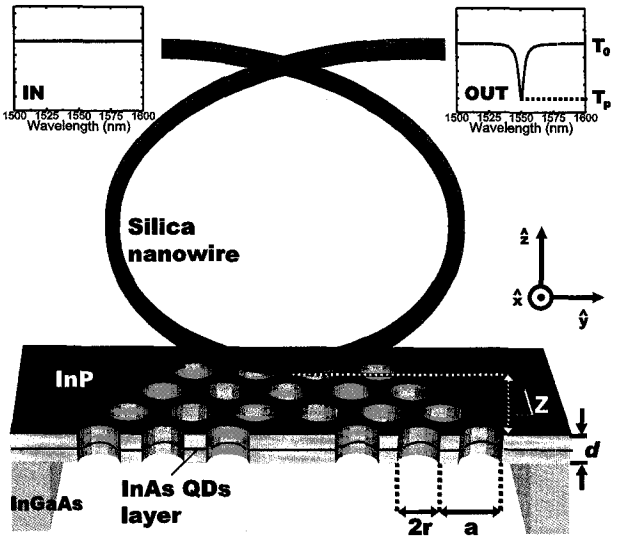

Figure 8.34: Schematics of the fiber-taper probing setup. A broadband emission source is coupled into the fiber, all the way down to the taper. The transmitted spectrum will show dips where the evanescent wave of the mode propagating in the taper couples with the microcavity modes evanescent fields.

Micro-Loop

A cartoon representation of the silica nanowire micro-loop setup is shown in figure 8.34. The silica nanowire is a tapered fibre fabricated using advanced flame brushing techniques. A more detailed description of the fabrication process can be found in references [200, 245]. The microloop is crucial in order to reach a small interaction region with the sample, *e.g.* for a microloop radius of 3 μm the interaction region would be around 600 nm and thus avoids probing multiple microcavities at the same time. The nanowire radii is about 100 nm, providing plenty of evanescent field to work with.

Typical experimental results I measured are shown in figure 8.35 where **(b)** presents

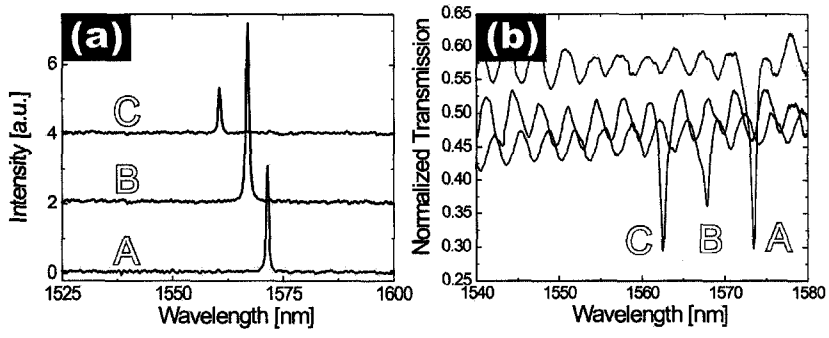

Figure 8.35: **(a)** PL spectra and **(b)** normalized transmission spectra for three nominally identical H1X microcavity.

	PL data		Transmission			
Microcavity	λ [nm]	Q	λ_T [nm]	Q_T	T	$\sqrt{T}Q_T$
A	1571	2900	1573.1	2000	0.50	2830
B	1565.7	2000	1567	1850	0.57	1900
C	1560	2400	1562.5	1650	0.75	2380

Table 8.2: Comparison between the experimental results for three nominally identical microcavities with PL and nanowire evanescent field coupling

normalized transmission spectra for three nominally identical **H1X** PhC microcavities and **(a)** shows their respective microcavity PL spectra. The agreement between measurements is quite remarkable, considering the nanowire is in contact with the sample. The oscillations in the normalized transmission are attributed to a Fabry-Pérot effect: the micro-loop creates a cavity of its own as the input and output taper are coupled and exchange light. The PL and transmission results are summarized in table 8.2. The experimental techniques yield the same numbers if the coupled mode theory is considered.

The distance between the nanowire and the microcavity center along the x-axis is

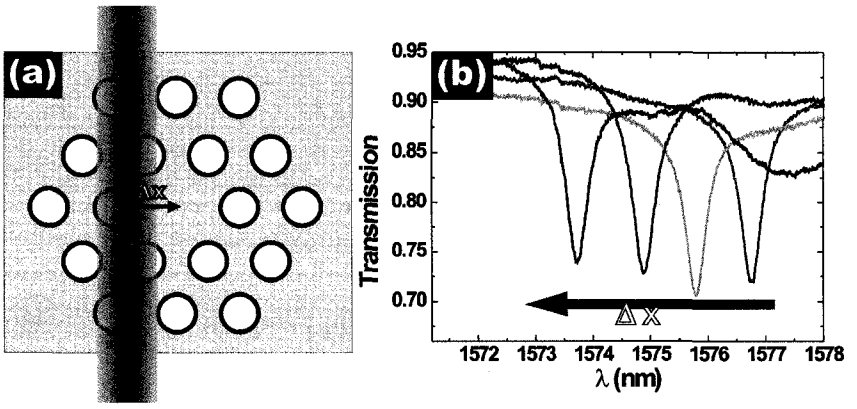

Figure 8.36: **(a)** Schematical representation of the distance Δx between the microcavity and the nanowire. **(b)** Normalized transmission spectrum for different distances Δx between the sample and the nanowire. The exact Δx value were not measurable with the current experimental setup. From [200]

given by Δx (see Fig.8.36) and Δz along the z-axis (see Fig.8.34). The parameters Δx and Δz are not measurable exactly with the current experimental setup, so it was not possible to extract data from Fig.8.36 apart from the tuning of the microcavity and the direction of the change in Δx. In the scenario where the nanowire is used to probe the microcavity mode structure it is necessary to minimize the coupling to achieve a good measurement. When the nanowire is used to tune the microcavity and extract the photons, a larger coupling is required. As was mentioned in section 6.3, the extraction efficiency (ϵ) is correlated with the quality factor (Q_T) of the microcavity-nanowire coupled system. Obviously Q_T is related to the system wavelength by $Q_T = \lambda_T/\Delta\lambda_T$ so a change in wavelength and Q_T confirms the coupling and hence the photon extraction.

In Fig.8.36 the large change in λ is accompanied by little to no change in Q. No clear explanation exists thus far, although it is clear that the coupling is varying.

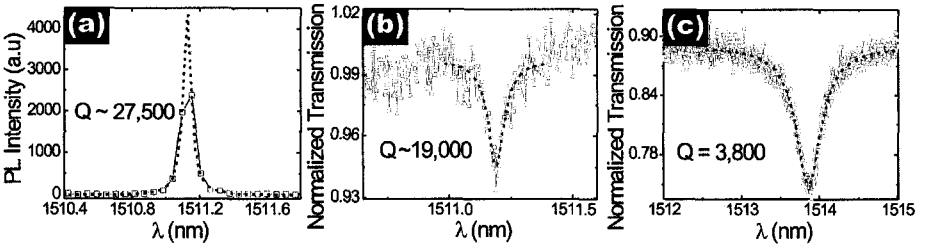

Figure 8.37: Typical results for **(a)** photoluminescence spectra, **(b)** normalized transmission spectra with nanowire out of contact, and **(c)** with the micro-loop in contact for **H1X** r_4=100 nm, δ_4=20 nm and δ_2=150 nm. Dashed lines are lorentzian fit to the data.

Other effects may play a role. For example, the nanowire refractive index is larger than air and consequently the mode effective index changes [199, 202]. Also, it has been shown that the nanowire proximity will lead to coupling to the higher order TM slab modes [201, 229, 254].

Things became harder to interpret when a I probed higher Q microcavity, as shown in Fig.8.37. Sub-figure **(a)** shows the PL of the microcavity, while **(b)** presents the same microcavity probed with a nanowire out of contact with the PhC ($\Delta z > 0$) and **(c)** $\Delta z = 0$. Neither transmission spectrum yields a result matching the PL data in wavelength or Q-factor, and the two of them are quite different from one another. The out of contact result (λ=1511.2 nm and Q=19 000) is much closer to the PL numbers: λ=1511.1 nm and Q=27 500. The microcavity perturbation by the nanowire is small, since the wavelengths agree and the transmission dip is quite shallow. Yet, the Q-factors do not match, even considering the mode coupling effect highlighted in equation (6.2). When $\Delta z = 0$ the Q drops to 3 800 and the microcavity shifts to 1513.9 nm. This large reduction in Q is even less well understood within our current

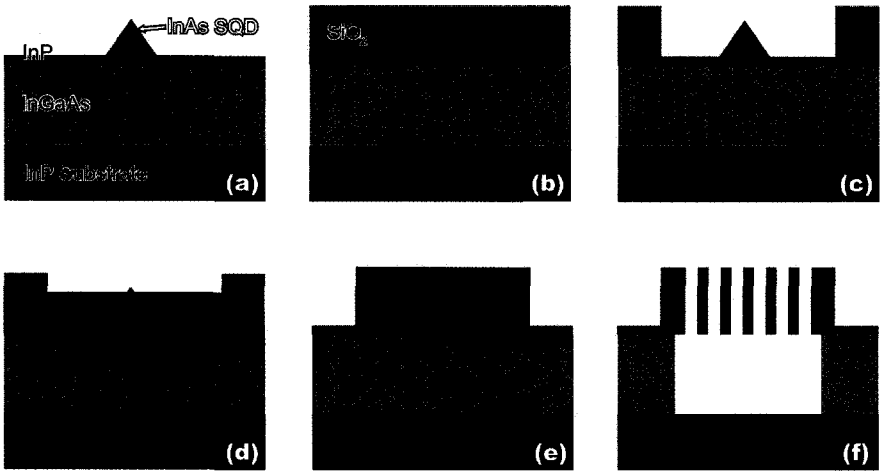

Figure 8.38: Fabrication procedure to planarize a site-selected SQD sample. Details of the process are in the text.

knowledge of the physics behind the microcavity-nanowire coupling. Further studies are currently underway by our colleagues in Australia.

8.6 InAs/InP Single Quantum Dots in PhC cavities

We performed exploratory work in regards to coupling a InAs/InP site-selected SQD. Following the growth procedure presented in Fig.8.38 a few additional steps are required to produce a dot in microcavity device as illustrated in 8.1. A second layer of SiO_2 is deposited onto the sample **(b)** with a layer of negative resist to create another opening in the SiO_2 onto the sample using the electron beam lithography techniques **(c)**. The use of alignment markers with our advanced electron beam system means a precision below 50 nm to place the microcavity mask over the pyramid containing the

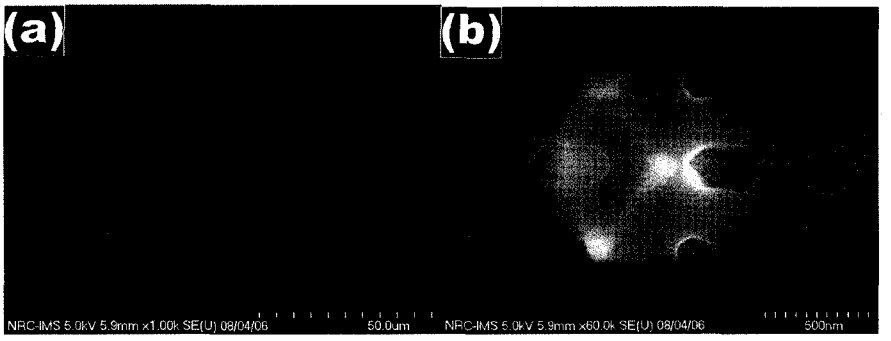

Figure 8.39: SEM images for a PhC microcavity wrapped around site-selected growth: an InP pyramid with QDs at the apex, underneath the capping layer.

SQD. The sample is put back into the growth chamber and further InP is grown on the sample. The relative uncleanliness of the exposed surface is not critical since it is not in direct contact with the QD. As explained in section 4.2 the growth proceeds primarily on the (001) surfaces, thus planarizing the sample surface **(d)**. The growth proceeds further and the final thickness is related not only with the height of the pyramid but also with the thickness of the underlying layer of InP grown onto the InGaAs because it is critical to locate the SQD at an antinode of the field within the slab. The last step of the planarization process is the removal of the remaining SiO_2. The sample is now as flat as a typical InAs/InP QD ensemble layer**(e)**. The construction of a cavity around the SQD requires precise markers and a very accurate electron beam lithography system. The steps involved in the fabrication process are exactly the same as described earlier (section 8.1).

Figure 8.39 shows two SEM images for our coupled site-selected QDs and PhC microcavities from a top view angle. Sub-figure **(a)** shows a view from far away where the nine alignment markers are shown. Three sets of three markers are used, each set

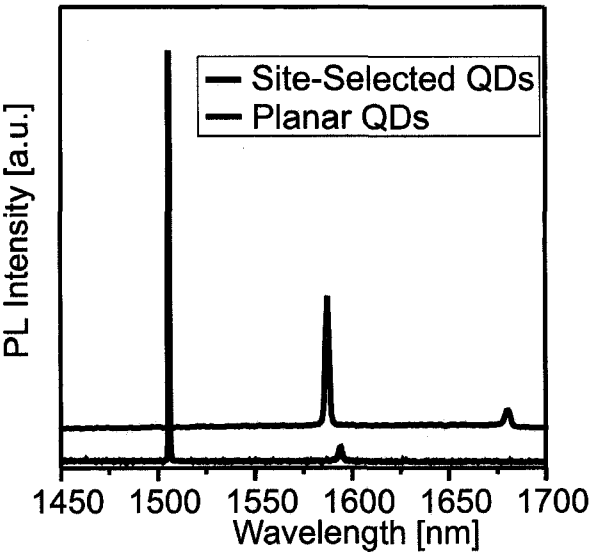

Figure 8.40: PL spectra similar PhC microcavity **H1X**. Red curve is obtained with site-selected QDs while blue curve is for planar QDs ensemble.

linked with the three different electron beam lithography steps. The elevated square is the planarized region and the PhC is at its center. Fig.8.39(**b**) shows a zoom in on the center of the PhC. The underlying pyramid is clearly visible. The pyramid is not supposed to be noticeable in a finished device but in this case the overgrowth was not done. In fact the hole etch was not even performed. We only did the electron beam exposure in order to assess our fabrication capability. The pyramid apex is very close to the defect center (to the field antinode) confirming our ability to grow a PhC microcavity precisely positioned with respect to a site-selected QD.

Before moving to the SQD scenario, we proceeded to test our ability by growing a group of site-selected QDs ($\sim$ 9) onto a large pyramid apex. At room temperature these QD ensembles provides a bright enough broadband PL source to probe the mode structure of the microcavity. The red curve in Fig.8.40 shows the result

for such a device and is to be compared with the blue curve of a nominally identical microcavity with an embedded planar QD ensemble. The two spectra are different for numerous reasons. A slight variation is expected, since the results originate from different sample runs but the major difference in wavelength is produced by the difference in membrane thickness for each sample ($\sim$200 nm for the site-selected sample with respect to the $\sim$ 450 nm for the other).

Using the post-fabrication tuning techniques presented in section 8.4 would enable, if not to recover the same Q-factor, at least the mode peak energy. As was explained in chapter 2 our experimental setup to do time-correlated single photon counting to prove the SP emission properties of a SQD was not sufficient to demonstrate anti-bunching. It is quite possible we have already achieved such a device but unfortunately were unable to prove it. The second generation of TCSPC setup I constructed will hopefully produce the required proof.

Chapter 9

Conclusion and Future Work

The work presented in this thesis demonstrates considerable progress towards the realization of a SP source based on an InAs/InP single quantum dot (SQD) in a microcavity. An experimental setup to characterize the anti-bunched nature of the QD emission was developed. A large number of microcavity designs were explored. In order to produce an efficient SP source based upon a SQD coupled to a microcavity, 5 key parameters were highlighted in chapter 5 namely: (*i*) have a high Purcell factor, (*ii*) a good spatial overlap between the SQD and microcavity mode electric field, (*iii*) a good spectral overlap between the SQD and microcavity mode, (*iv*) the QD electric-dipole match with the mode polarization and (*v*) a far-field radiation pattern suitable to funnel the SPs to a communication channel. The micropillar microcavity provided a suitable optical output to funnel the photons, but in the end optimizing its quality factor (Q) while reducing the mode volume and post-fabrication tuning the emission energy to match that of the dot provided too great a challenge. The best micropillar constructed had a Q of $\sim$1500 for a pillar radii of 1 μm, enough to produce a reasonably efficient SP source. Another advantage of the micropillar is the

easy prediction of their mode energy. The distributed Bragg reflector (DBR) mirror wavelengths are easily predicted by an effective index method and the thin film systems of the Institute for Microstructural Sciences (IMS) are very precise and versatile. Micropillar microcavities fulfil all 5 criteria but their Purcell factor was limited.

Many PhC microcavity designs were investigated, with many different modes, quality factors, mode volumes and radiation patterns. The **H1X** design is the "winner"; optimizing the x-dipole-like mode with a Q over 20 000 and mode volume equal to half a cubic wavelength. Our design now holds the record Q for an InP-based PhC microcavity; much higher than that for a micropillar, while the 5 key parameters are more easily optimized. For example, the PhC microcavity is adjustable post-fabrication through digital etching. It consists in the successive removal and growth of the native oxide layer on the InP by an HF etch. Each cycle yields an augmentation of the hole radii by 6.5Å while the membrane thickness is reduced by 7.5Å. It is important to be able to tune the microcavity post-fabrication because the construction of the PhC is a challenge and requires great precision. With a post-fabrication tuning tool in hand, the requirements on the fabrication are no longer so stringent and one can deliberately design the cavity mode energy to be too low, so that any imperfections can be compensated by finishing with an appropriate post-fabrication tuning.

A silica nanowire coupled to a microcavity will tune it to a certain extent. The mechanism behind this tuning needs to be further clarified through both experiment and theory in order to be more predictable. With a firm grip on the mechanism the tuning mechanism could be applied more effectively. Moreover, the silica nanowire

can be used to probe the mode structure of a microcavity by measuring the transmission dips in a broadband spectrum. One must be careful to couple to the microcavity only moderately however to avoid changing the mode properties while probing it, although in some cases it would be desirable to do so.

The most interesting aspect of the nanowire coupling is the ability to use it as a tool to collect emitted photons from the SQD-microcavity system. This could not be measured directly with our experimental setup but only interpreted from the experimental results. Nevertheless, it is an exciting approach certainly worth pursuing. The current nanowire experimental setup would not work with our QD samples, because the sample needs to be cooled to 4 K in a cryostat The silica nanowire microloop fabrication procedure yields a relatively fragile and stressed nanowire, and the low temperature will probably make it break to pieces. A different design is required. Initial simulations show that a cleaved fiber coming from the top would work properly and if the fiber could be replaced by a PhC fiber [255] the mode matching between the PhC microcavity and the fiber would be better. A straight-up fiber would be easier to put in a tight holder, close to the sample, and within the cryostat. In a holder, it could more easily withstand the low temperature. The insertion of a single site-selected InAs/InP QD in a microcavity might have been achieved within this work. The overlap between the site-selected pyramid and the PhC microcavity was clearly demonstrated. The only thing left is to actually perform the anti-bunching measurement. The difficulties encountered in performing a time-correlated single photon counting (TCSPC) measurement in the near infrared (NIR) meant that a clear measurement was not achieved, although significant progress was made. It should be

noted that thus far only three other groups have achieved a TCSPC experiment with QDs in the NIR [76, 108, 127].

Another interesting avenue for the future would be to explore possibilities for coupling a SQD to a waveguide. Given the refractive index of InP and the help of the waveguide, such a setup would collect at least 10 times as many photons from the QD. Even better would be for two different SQD-microcavity systems to be coupled together via a waveguide. This would be the first step towards QCpu on a chip (see [144, 243]). Adding electrostatic gates to the mix to control the electrons and holes populating the SQDs [27, 76] would result in a compact device that would be a strong candidate for QCpu.

Bibliography

[1] Marlan O. Scully and M. Suhail Zubairy. *Quantum Optics.* Cambridge University Press, United Kindom, 1997.

[2] Y. Yamamoto and A. İmamoğlu. *Mesoscopic Quantum Optics.* John-Wiley & Sons, New York, 1999.

[3] J. Vučkovič, D. Englund, D. Fattal, E. Waks, and Y. Yamamoto. Generation and Manipulation of Nonclassical Light using Photonic Crystal. *Physica E*, 32:466, 2006.

[4] N. Gisin, G. Ribordy, W. Tittel, and H. Zbiden. Quantum Cryptography. *Rev. Mod. Phys.*, 74:145, 2002.

[5] N. Gisin and R. Thew. Quantum Communication. *Nature Physics*, 1:165, 2007.

[6] C.H. Bennett and G. Brassard. Quantum cryptography: Public key distribution and coin tossing. In IEEE, editor, *Proceedings of the IEEE International Conference on Computers, Systems and Signal Processing*, page 175, 1984.

[7] M. Bloch, S.W. McLaughlin, J.-M. Marolla, and F. Patois. Frequency-coded Quantum Key Distribution. *Opt. Lett.*, 32:301, 2007.

[8] N.J. Cerf and P. Grangier. From Quantum Cloning to Quantum Key Distribution with Continuous Variables: a Review. *J. Opt. Soc. Am. B*, 24:324, 2007.

[9] C.-W. Chou, J. Laurat, H. Deng, K.S. Choi, and H. de Riedmatten. Functional Quantum Nodes for Entanglement Distribution over Scalable Quantum Networks. *Science*, 316:1316, 2007.

[10] R. Ursin, F. Tiefenbacher, T. Schmitt-Manderbach, H. Weier, T. Scheidl, M. Lindenthal, B. Blauensteiner, T. Jennewein, J. Perdigues, P. Trojek, B. Ömer, M. Fürst, M. Meyenburg, J. Rarity, Z. Sodnik, C. Barbieri, H. Weinfurter, and A. Zeilinger. Entanglement-based Quantum Communication over 144 km. *Nature Physics*, 3:481, 2007.

[11] MagiQ Technologies. http://magiqtech.com.

[12] id Quantique Inc. http://idquantique.com/.

[13] SmartQuantum. http://www.smartquantum.com/SmartQuantum.html.

[14] R.P. Feynman. Quantum Mechanical Computers. *Opt. News*, 11:11, 1985.

[15] D. Deutsch. Quantum Theory, the Church-Turing Principle and the Universal Quantum Computer. *Proc. R. Soc. Long. A*, 400:97, 1985.

[16] D.P. DiVincenzo. Quantum Computation. *Science*, 270:255, 1995.

[17] P.W. Shor. Polynomial-Time Algorithms for Prime Factorization and Discrete Logarithms on a Quantum Computer. In IEEE Computer Society Press, editor, *Proceedings of the 35th ASFCS*, page 124, Santa Fe, NM, 1994.

[18] L.K. Grover. Quantum Mechanics Helps in Searching for a Needle in a Haystack. *Phys. Rev. Lett.*, 79:325, 1997.

[19] G.J. Milburn. Quantum Optical Fredkin Gate. *Phys. Rev. Lett.*, 62:2124, 1989.

[20] E. Knill, R. Laflamme, and G.J. Milburn. A Scheme for Efficient Quantum Computation with Linear Optics. *Nature*, 409:46, 2001.

[21] H. Paul. Photon Antibunching. *Rev. Mod. Phys.*, 54(4):1061, 1982.

[22] P. Kok, W.J. Munro, K. Nemoto, T.C. Ralph, J.P. Sowling, and G.J. Milburn. Linear Optical Quantum Computing with Photonic Qubits. *Rev. Mod. Phys.*, 79:135, 2007.

[23] A. Kiraz, M. Atatüre, and A. Imamoğlu. Quantum-Dot Single Photon Sources: Prospects for Applications in Linear Optics Quantum-Information Processing. *Phys. Rev. A*, 69:032305, 2004.

[24] H. Mauchi and A.C. Doherti. Cavity Quantum Electrodynamics: Coherence in Context. *Science*, 298:1372, 2002.

[25] M. Hijkema, B. Weber, H.P. Specht, S.C. Webster, A. Kuhn, and G. Rempe. A Single-Photon Server with Just One Atom. *Nature*, 3:253, 2007.

[26] E.M. Purcell. Spontaneous Emission Probabilities at Radio Frequencies. *Phys. Rev.*, 69:681, 1946.

[27] M. Kroutvar, Y. Ducommun, D. Heiss, M. Bichler, S. Schuh, G. Abstreiter, and J.J. Finley. Optically Programmable Electron Spin Memory using Semiconductor Quantum Dots. *Nature*, 432:81, 2004.

[28] J.I. Cirac, P. Zoller, H.J. Kimble, and H. Mabuchi. Quantum State Transfer and Entanglement Distribution among Distant Nodes in a Quantum Networks. *Phys. Rev. Lett.*, 78:3221, 1997.

[29] A. Imamoğlu, D.D. Awschalom, G. Burkard, D.P. DiVincenzo, D. Loss, M. Sherwin, and A. Small. Quantum Information Processing Using Quantum Dot Spins and Cavity QED. *Phys. Rev. Lett.*, 83:4204, 1999.

[30] L. Ye and G.-C. Guo. Scheme for Implementing Quantum Dense Coding in Cavity QED. *Phys. Rev. A*, 71:034304, 2005.

[31] D. Bouwmester, J.-W. Pan, K. Mattle, M. Eibi, H. Weinfurter, and A. Zeilinger. Experimental Quantum Teleportation. *Nature*, 390:575, 1997.

[32] Y.H. Shih and C.O. Alley. New Type of Einstein-Podolsky-Rosen-Bohm Experiment Using Pairs of Light Quanta Produced by Optical Parametric Down Conversion. *Phys. Rev. Lett.*, 61:2921, 1988.

[33] T.E. Kiess, Y.H. Shih, A.V. Sergienko, and C.O. Alley. Einstein-Podolsky-Rosen-Bohm Experiment Using Pairs of Light Quanta Produced by Type-II Parametric Down-Conversion. *Phys. Rev. Lett.*, 71:3893, 1993.

[34] T.B. Pittman, B.C. Jacobs, and J.D. Franson. Heralding Single Photons from Pulse Parametric Down-Conversion. *Opt. Comm.*, 246:545, 2005.

[35] T.-G. Noh, H. Kim, T. Zyung, and J. Kim. Efficient Source of High Purity Polarization-Entagnled Photon Pairs in the 1550 nm Telecommunication Band. *Appl. Phys. Lett.*, 90:011116, 2007.

[36] J.F. Hodelin, G. Khoury, and D. Bouwmesster. Optimal Generation of Pulsed Entangled Photon Pairs. *Phys. Rev. A*, 74:013802, 2006.

[37] A. Yoshizawa and H. Tsuchida. Generation of Polarization-Entangled Photon Pairs in 1550 nm band by a Fiber-Optic Two-Photon Interferometer. *Appl. Phys. Lett.*, 85:2457, 2004.

[38] H. Takesue, K. Inoue, O. Tadanaga, Y. Nishida, and M. Asobe. Generation of Pulsed Polarization-Entangled Photon Pairs in a 1.55-μm Band with a Periodically Poled Lithium Niobate Waveguide and an Orthogonal Polarization Delay Circuit. *Opt. Lett.*, 30:293, 2005.

[39] A.B. U'Ren, C. Silberhorn, K. Banasek, and I.A. Walmsley. Efficient Conditional Preparation of High-Fidelity Single Photon States for Fiber-Optic Quantum Networks. *Phys. Rev. Lett.*, 93:093601, 2004.

[40] A.B. U'ren, C. Silberhorne, J.L. Ball, K. Banaszek, and I.A. Walmsley. Characterization of the Nonclassical Nature of Conditionally Prepared Single Photons. *Phys. Rev. A*, 72:021802(R), 2005.

[41] C.E. Kuklewicz, F.N.C. Wong, and J.H. Shapiro. Time-Bin-Modulated Biphotons from Cavity-Enhanced Down-Conversion. *Phys. Rev. Lett.*, 97:223601, 2006.

[42] J. Chen, K.F. Lee, C. Liang, and P. Kumar. Fiber-Based Telecom-Band Degenerate-Frequency Source of Entangled Photon Pairs. *Opt. Lett.*, 31:2798, 2006.

[43] Q. Lin, F. Yaman, and G.P. Agrawal. Photon-Pair Generation by Four-Wave Mixing in Optical Fibers. *Opt. Lett.*, 31:1286, 2006.

[44] N.H. Lindner, J. Avron, N. Akopian, and D. Gershoni. A comment on: A Semiconductor Source of Triggered Entangled Photon Pairs. *arXiv:quant-ph*, page 0601200, 2006.

[45] M.A. Foster, A.C. Turner, J.E. Sharping, B.S. Schmidt, M. Lipson, and A.L. Gaeta. Broadband Optical Parametric Gain on a Silicon Photonic Chip. *Nature*, 441:960, 2006.

[46] C.K. Law and H.J. Kimble. Deterministic Generation of a Bit-Stream of Single-Photon Pulses. *J. Mod. Optics*, 44:2067, 1997.

[47] K. Bergmann, T. Theuer, and B.W. Shore. Coherent Population Transfer amoung Quantum States of Atoms and Molecules. *Rev. Mod. Phys.*, 70:1003, 1998.

[48] M. Keller, B. Lange, K. Hayasaka, W. Lange, and H. Walther. Continuous Generation of Single Photons with Controlled Waveform in an Ion-trop Cavity System. *Nature*, 431:1075, 2004.

[49] C. Kurtsiefer, S. Mayer, P. Zarda, and H. Weinfurther. Stable Solid-State Source of Single Photons. *Phys. Rev. Lett.*, 85:290, 2000.

[50] A. Beveratos R. Bouri, T. Gacoin, A. Villing, J.P. Poizat, and P. Grangier. Single Photon Quantum Cryptography. *Phys. Rev. Lett.*, 89:187901, 2002.

[51] S. Tomljenovic-Hanic, M.J. Steel, C. M. de Sterke, and J. Salzman. Diamond-Based Photonic Crystal Microcavities. *Opt. Expree*, 14:3556, 2006.

[52] L. Childress, M.V. Gurudev Dutt, J.M. Taylor, A.S. Zibrov, F. Jelezko, J. Wrachtrup, P.R. Hemmer, and M.D. Lukin. Coherent Dynamics of Coupled Electron and Nuclear Spin Qubits in Diamond. *Science*, 314:281, 2006.

[53] R. Hanson, F.M. Mendoza, R.J. Epstein, and D.D. Awschalom. Polarization and Readout of Coupled Single Spins in Diamond. *Phys. Rev. Lett.*, 97:087601, 2006.

[54] R. Hanson, O. Gywat, and D.D. Awschalom. Room-Temperature Manipulation and Decoherence of a Single Spin in Diamond. *Phys. Rev. B*, 74:161203(R), 2006.

[55] T. Gaebel, M. Domhan, I. Popa, C. Wittmann, P. Neumann, F. Jelezko, J.R. Rabeau, N. Stavrias, A.D. Greentree, S. Prawer, J. Meijer, J. Twamley, P.R. Hemmer, and J. Wrachtrup. Room-Temperature Coherent Coupling of Single Spins in Diamond. *Nature Physics*, 2:408, 2006.

[56] C. Santori, D. Fattal, S.M. Spillane, M. Fiorentino, R.G. Beausoleil, A.D. Greentree, P. Olivero, M. Draganski, J.R. Rabeau, P. Reichart adn B.C. gibson, S. Rubanov, D.N. Jamieson, and S. Prawer. Coherent Population Trapping in Diamond N-V Centers at zero Magnetic Field. *Opt. Express*, 14:7986, 2006.

[57] E. Waks, K. Inoue, C. Santori, D. Fattal, J. Vuckovic, G.S. Solomon, and Y. Yamamoto. Quantum Cryptography with a Photon Turnstile. *Nature*, 420:762, 2002.

[58] D. Fattal, E. Diamanti, K. Inoue, and Y. Yamamoto. Quantum Teleportation with a Quantum Dot Single Photon Source. *Phys. Rev. Lett.*, 92:037904, 2004.

[59] D. Fattal, K. Inoue, J. Vučković, C. Santori, G.A. Solomon, and Y. Yamamoto. Entanglement Formation and Violation of Bell's Inequality with a Semiconductor Single Photon Source. *Phys. Rev. Lett.*, 92:037903, 2004.

[60] M. Scholz, T. Aichele, S. Ramelow, and O. Benson. Deutsch-Joza Algorithm Using Triggered Single Photons from a Single Quantum Dot. *Phys. Rev. Lett.*, 96:180501, 2006.

[61] C. Santori, D. Fattal, J. Vučkivič, G. S. Solomon, and Y. Yamamoto. Indistinguishable Photons from a Single-Photon Device. *Nature*, 419:594, 2002.

[62] S. Laurent, S. Varoutsis, L. Le Gratiet, A. Lemaître, I. Sagnes, F. Raineri, A. Levenson, I. Robert-Phillip, and I. Abram. Indistinguishable Single Photons from a Single-Quantum Dot in a Two-Dimensional Photonic Crystal Cavity. *Appl. Phys. Lett.*, 87:163107, 2005.

[63] O. Benson, C. Santori, M. Pelton, and Y. Yamamoto. Regulated and Entangled Photons form a Single Quantum Dot. *Phys. Rev. Lett.*, 84(11):2513, 2000.

[64] E. Moreau, I. Robert, L. Manin, V. Thierry-Mieg, J.M. Gérard, and I. Abram. Quantum Cascade of Photons in Semiconductor Quantum Dots. *Phys. Rev. Lett.*, 87(18):183601, 2001.

[65] D.V. Regelman, U. Mizrahi, D. Gershoni, E. Ehrenfreund adn W.V. Shoenfeld, and P.M. Petroff. Semiconductor Quantum Dot: A Quantum Light Source of Multicolor Photons with Tunable Statistics. *Phys. Rev. Lett.*, 87:257401, 2001.

[66] C. Santori, D. Fattal, M. Pelton, G.S. Solomon, and Y. Yamamoto. Polarization-Correlated Photon Pairs from a Single Quantum Dot. *Phys. Rev. B*, 66:045308, 2002.

[67] R.M. Stevenson, R.J. Young, P. Atkinson, K. Cooper, D.A. Ritchie, and A.J. Shields. A Semiconductor Source of Triggered Entangled Photon Pairs. *Nature*, 439:179, 2006.

[68] N. Akopian, N.H. Lindner, E. Poem, Y. Berlatzky, J. Avron, D. Gershoni, B.D. Gerardot, and P.M. Petroff. Entangled Photon Pairs from Semiconductor Quantum Dots. *Phys. Rev. Lett.*, 69:130501, 2006.

[69] A. Gilchrist, K.J. Resch, and A.G. White. Reply: Source of Triggered Entangled Photon Pairs. *Nature*, 445:E4, 2007.

[70] P.M. Stevenson, R.J. Young, P. Atkinson, and K. Cooper. Reply: Source of Triggered Entangled Photon Pairs. *Nature*, 445:E5, 2007.

[71] R.M. Stevenson, A.J. Hudson, R.J. Young, P. Atkinson, K. Cooper, D.A. Ritchie, and A.J. Schields. Biphoton Interference with a Quantum Dot Entangled Light Source. *Opt. Express*, 15:6507, 2007.

[72] H. Benistry, J.-M. Gérard, R. Houdré, J. Rarity, and C. Weisbuch. *Confined Photon Systems: Fundamentals and Applications.* Lecture Notes on Physics. Springer, Milan, 1999.

[73] Ulf Leonhardt. *Measuring the Quantum State of Light.* Cambridge Studies in Modern Optics. Cambridge University Press, Cambridge, UK, 1997. 194 pages.

[74] R. Hanbury Brown and R.Q. Twiss. Correlation Between Photons in Coherent Light Rays. *Nature*, 177:27, 1956.

[75] V. Zwiller, H. Blom, P. Jonsson, N. Panev, S. Jeppesen, T. Tsegaye, E. Goobar, M.-E. Pistol an dL. Samuelson, and G. Bj̈ork. Single Quantum Dots emit Single Photons at a time: Antibunching Experiments. *Appl. Phys. Lett.*, 78(17):2476, 2001.

[76] M.B. Ward, T. Farrow, P. See, Z.L. Yuan, O.Z. Karimov, A.J. Bennett, A.J. Shields, P. Atkinson, K. Cooper, and D.A. Ritchie. Electrically Driven Telecommunication Wavelength Single-Photon Source. *Appl. Phys. Lett.*, 90:063512, 2007.

[77] A.J. Miller, S.W. Nam, J.M. Martinis, and A.V. Sergienko. Demonstration of a Low-Noise Near-Infrared Photon Counter with Multiphoton Discrimination. *Appl. Phys. Lett.*, 83(4):791, 2003.

[78] D. Rosenberg, A.E. Lita, A.J. Miller, and S.W. Nam. Noise-Free High-Efficiency Photon-Number-Resolving Detectors. *Phys. Rev. A*, 71:061803(R), 2005.

[79] C. Delacour, J. Claudon, J.-Ph. Poizat, B. Pannetier, V. Bouchiat, R.Espiau de Lamaestre, J.-C. Villegier, M. Tarkhov, A. Korneev, B. Voronov, and G. Gol'tsman. Superconducting Single Photon Detectors made by Local Oxidation with an Atomic Force Microscope. *Appl. Phys. Lett.*, 90:191116, 2007.

[80] R.H. Hadfield, M.J. Stevens, R.P. Mirin, and S.W. Nam. Single-Photon Source Characterization with Twin Infrared-Sensitive Superconducting Single-Photon Detectors. *J. Appl. Phys.*, 101:103104, 2007.

[81] P.A. Hiskett, G.S. Buller, A.Y. Loudon, J.M. Smith, I. Gontijo, A.C. Walker, P.D. Townsend, and M.J. Robertson. Performance and Design of InGaAs/InP Photodiodes for Single-Photon Counting at 1.55μm. *Appl. Opt.*, 39(36):6818, 2000.

[82] E.F. Schubert. *Light-Emitting Diodes.* Cambridge University Pres, 2006.

[83] Danny Kim. *Deterministic Control of the Quantum Properties of Single InAs Artificial Atoms with InP Nanoscale Architectures.* PhD thesis, University of Toronto, 2007.

[84] H. Marchand, P. Desjardins, S. Guillon, J.-E. Paultre, Z. Bougrioua, R.Y.-F. Yip, and R.A. Masut. Metalorganic Vapor Phase Epitaxy of Coherent Self-Assembled InAs Nanometer-Sized Islands in InP(001). *Appl. Phys. Lett.*, 71:527, 1997.

[85] S. Yoon, Y. Moon, T.-W. Lee, E. Yoona, and Y.D. Kim. Effects of As/P Exchange Reaction on the Formation of InAs/InP Quantum Dots. *Appl. Phys. Lett.*, 74:2029, 1999.

[86] J.M. Benoit, L. Le Gratiet, G. Beaudoin, A. Michon, G. Saint-Girons, R. Kuszelewicz, and I. Sagnes. Nanoepitaxy of InAs/InP Quantum Dots by Metalorganic Vapor Phase Epitaxy for 1.55 μm Emitters. *Appl. Phys. Lett.*, 88:041113, 2006.

[87] T. Ujihara, Y. Yoshida, W.S. Lee, and Y. Takeda. Size Uniformity of InAs Dots on Mesa-Structure Templates on (001)InP Substrates Grown by Droplet Metal-Organic Vapor Phase Epitaxy Method. *Appl. Phys. Lett.*, 89:083110, 2006.

[88] B. Bansal, M.R. Gokhale, A. Bhattacharya, and B.M. Arora. InAs/InP Quantum Dots with Bimodal Size Distribution: Two Evolution Pathways. *J. Appl. Phys.*, 101:094303, 2007.

[89] A. Ponchet, A. Le Corre, H. L'Haridon, B. Lambert, and S. Salaün. Relationship between Self-Organization and Size of InAs Islands on InP(001) Grown by Gas-Source Molecular Beam Epitaxy. *Appl. Phys. Lett.*, 67:1850, 1995.

[90] S. Zhongzhe, L. Fengqi, D. Ding, X. Bo, and W. Zhanguo. Self-assembled InAs and $In_{0.9}Al_{0.1}As$ Quantum Dots on (001)InP Substrates Grown by Molecular Beam Epitaxy (MBE). *J. Cryst. Growth*, 204:24, 1999.

[91] N. Chauvin, B. Salem, G. Bremond, G.Guillot, C. Bru-Chevalier, and M. Gendry. Size and Shape Effects on Excitons and Biexcitons in Single InAs/InP Quantum Dots. *J. Appl. Phys.*, 100:073702, 2006.

[92] E. Dupuy, P. Regreny, Y. Robach, M. Gendry, N. Chauvin, E. Tranvouez, C. Bru-Chevalier, and G. Patriarche. Low Density of Self-Assembled InAs Quantum Dots Grown by Solid-Source Molecular Beam Epitaxy on InP(001). *Appl. Phys. Lett.*, 89:123112, 2006.

[93] P.J. Poole, J. McCaffrey, R.L. Williams, J. Lefebvre, and D. Chithrani. Chemical Beam Epitaxy Growth of Self-Assembled InAs/InP Quantum Dots. *J. Vac. Sci. Technol. B*, 19(4):1467, 2001.

[94] B. Alén, D. Fuster, Y. González, L. González, and J. Martinez-Pastor. InAs/InP Single Quantum Wire Formation and Emission at 1.5 μm. *Appl. Phys. Lett.*, 89:233126, 2006.

[95] D. Fuster, J. Martinez-Pastor, L. González, and Y. González. Exciton Recombination Dynamics in InAs/InP Self-Assembled Quantum Wires. *Phys. Rev. B*, 71:205329, 2005.

[96] D. Fuster, L. González, Y. González, M.J. González, and J.M. Martinez-Pastor. Size and Emission Wavelength Control of InAs/InP Quantum Wires. *J. Appl. Phys.*, 98:033502, 2005.

[97] F. Suárez, D. Fuster, L. González, Y. González, J.M. Garcia, and M.L. Dotor. Self-Assembled InAs Quantum Wire Lasers on (001)InP at 1.6 μm. *Appl. Phys. Lett.*, 89:091123, 2006.

[98] D. Zhou, R. Nötzel, Q. Gong, P. Offermans, P.M. Koenraad, P.J. van Veldhoven, F.W.M. van Otten, T.J. Eijkemans, and J.H. Wolter. (In,Ga)As Sidewall Quantum Wires on Shallow-Patterned InP(311)A. *J. Appl. Phys.*, 97:063510, 2005.

[99] N. Chauvin, B. Salem, C. Bru-Chevalier, T. Benyattou, G. Guillot, G. Bremond, C. Monat, P. Rojo-Romeo, and M. Gendry. Micro-Photoluminescence Study of Single Self-Organized InAs/InP Quantum Sticks. *Material Sci. Eng. C*, 25:650, 2005.

[100] B. Salem, V. Aimez, D. Morris, A. Turala, P. Regreny, and M. Gendry. Band Gap Tuning of InAs/InP Quantum Sticks using Low-Energy Ion-Implantation-Induced Intermixing. *Appl. Phys. Lett.*, 87:241115, 2005.

[101] M. van der Poel, J. Mørk, A. Somers, A. Forchel, J.P. Reithmaier, and G. Eisenstein. Ultrafast Gain and Index Dynamics of Quantum Dash Structures Emitting at 1.5 μm. *Appl. Phys. Lett.*, 89:081102, 2006.

[102] D. Hadass, V. Mikhelashvili, G. Eisenstein, A. Somers, S. Deubert, W. Kaiser, J.P. Reithmaier, A. Forchel, D. Finzi, and Y Maimon. Time-Resolved Chirp in an InAs/InP Quantum-Dash Optical Amplifier Operating with 10Gbit/s Data. *Appl. Phys. Lett.*, 87:021104, 2005.

[103] P. Podemski, R. Kudrawiec, J. Misiewicz, A. Somers, R. Schertberger, J.P. Reithmaier, and A. Forchel. Thermal Quenching of Photoluminescence for InAs/$In_{0.53}Ga_{0.23}Al_{0.24}As$/InP Quantum Dashes with Different Sizes. *Appl. Phys. Lett.*, 89:151902, 2006.

[104] J. Sormunen, J. Riikonen, M. Mattila nd J. Tiilikainen, M. Sopanen, and H. Lipsanen. Transformation of Self-Assembled InAs/InP Quantum Dots into Quantum Rings without Capping. *Nanoletters*, 5:1541, 2005.

[105] A. Sauerwald, T. Kümmell, G. Bacher, A. Somers, R. Schwertberger, J.P. Reithmaier, and A. Forchel. Size Control of InAs Quantum Dashes. *Appl. Phys. Lett.*, 86:253112, 2005.

[106] B. Alloing, C. Zioni, V Zwiller, L.H. Li, M. Gobet, G. Buchs, A. Fiore, E. Pelucchi, and E. Kapon. Growth and Characterization of Single Quantum Dots Emitting at 1300nm. *Appl. Phys. Lett.*, 86:101908, 2005.

[107] C. Monat, B. Alloing, C. Zinoni, L.H. Li, and A. Fiore. Nanostructured Current-Confined Single Quantum Dot Light-Emitting Diode at 1300 μm. *Nanoletters*, 6:1464, 2006.

[108] C. Zioni, B. Alloing, C. Monat, V. Zwiller, L.H. Li, S. Flore, L. Lunghi, A. Geradino, H. de Riedmatten, H. Zbinden, and N. Gisin. Time-Resolved and Antibunching Experiments on Single Quantum Dots at 1300 nm. *Appl. Phys. Lett.*, 88:131102, 2006.

[109] C. Zinoni, B. Alloing, L.H. Li, F. Marsili, A. Fiore, L. Lunghi, A. Gerardino, Y.B. Vakhtomin, K.V. Smirnov, and G.N. Gol'tsman. Single-Photon Experiments at Telecommunication Wavelengths using Nanowire Superconducting Detectors. *Appl. Phys. Lett.*, 91:031106, 2007.

[110] K. Akahane, N. Yamamoto, S.-I. gozu, A. Ueta, and N. Ohtani. 1.5 μm Emission for InAs Quantum Dots with InGaAsSb Strain Reducing Layer Grown on GaAs Substrates. *Physica E*, 32:81, 2006.

[111] L. Seravalli, P. Frigeri, M. Minelli, P. Allegri, V. Avanzini, and S. Franchi. Quantum Dot Strain Engineering for Light Emission at 1.3, 1.4 and 1.5 μm. *Appl. Phys. Lett.*, 87:063101, 2005.

[112] K. Park, E. Ahn, Y.J. Jeon, H.M. Cheong, J.S. Kim, E.K. Kim, J. Lee, Y.J. Park, G.-D. Lee, and E. Yoon. The Emission Wavelength Tuning of InAs/InP

Quantum Dots with Thin GaAs, InGaAs, InP Capping Layers by MOCVD. *Physica E*, 26:169, 2005.

[113] K. Park, P. Moon, E. Ahn, E. Yoon, J.W. Yoon, H. Cheong, and J.-P. Leburton. Effects of Thin GaAs Insertion Layer on InAs/(InGaAs)/InP(001) Quantum Dots Grown by Metalorganic Chemical Vapor Deposition . *Appl. Phys. Lett.*, 86:223110, 2005.

[114] N.I. Cade, H. Gotoh, H. Kamada, H. Nakano, S. Ananntathanasarn, and R. Nötzel. Optical Characteristics of Single InAs/InGaAsP/InP(100) Quantum Dots Emitting at 1.55 μm. *Appl. Phys. Lett.*, 89:181113, 2006.

[115] H.D. Kim, W.G. Jeong, J.H. Lee, J.S. Yim, D. Lee, R. Stevenson, P.D. Dapkus, J.W. Jang, and S.H. Pyun. Continuous-Wave Operation of 1.5 μm InGaAs/InGaAsP/InP Quantum Dot Lasers ar Room Temperature. *Appl. Phys. Lett.*, 87:083110, 2005.

[116] Y.D. Jang, E.G. Lee, J.S. Yim, D. Lee, W.G. Jeong, S.H. Pyun, and J.W. Jang. Unambiguous Observation of Electronic Couplings between InGaAs/InGaAsP Quantum Dots at 1.5 μm. *Appl. Phys. Lett.*, 88:091920, 2006.

[117] D. Zhou, S. Anantathannasarn, P.J. van Veldhoven, F.W.M. van Otten, T.J. Eijkemans, T. de Vries, E. Smalbrudgge, and R. Nötzel. Lateral Wavelength Control of InAs/InGaAs/InP(001) Quantum Dots in the 1.55 μm Region by Selective Area Metal Organic Vapor Phase Epitaxy. *J. Appl. Phys*, 100:113512, 2006.

[118] X.B. Zhang, J.H. Ryou, and R.D. Dupuis. Growth of InAlAs Self-Assembled Quantum Dots on InAlGaAs/InP for 1.55 μm Laser Applications by Metalorganic Chemical vapor deposition. *Appl. Phys. Lett.*, 89:191104, 2006.

[119] S. Barik, H.H. Tan, and C. Jagadish. High Temperature Rapid Thermal Annealing of Phosphorous Ion Implanted InAs/InP Quantum Dots. *Appl. Phys. Lett.*, 90:093106, 2007.

[120] C. Cornet, C. Labbé, H. Folliot, P. Caroff, C. Levallois, O. Levallois, O. Dehaese, J. Even, A. Le Corre, and S. Loualiche. Time-Resolved Pump Probe of 1.55 *mu*m InAs/InP Quantum Dots under High Resonant Excitation. *Appl. Phys. Lett.*, 88:171502, 2006.

[121] P. Miska, C. Paranthoen, J. Even, O. Dehaese, H. Folliot, N. Bertu, S. Loualiche, M. Senes, and X. Marie. Optical Spectroscopy and Modeling of Double-Cap Grown InAs/InP Quantum Dots with Long Wavelength Emission. *Semicond. Sci Technol.*, 17:L63, 2002.

[122] P. Miska, J. Even, C. Paranthoen, O. Dehaese, H. Folliot, S. Loualiche, M. Senes, and X. Marie. Optical Properties and Carrier Dynamics of InAs/InP(113)B Quantum Dots Emitting between 1.3 and 1.55μm for Laser Applications. *Physica E*, 17:56, 2003.

[123] P. Miska, J. Even, C. Paranthoen, O. Dehaese, A. Jbeli, M. Senès, and X. Marie. Vertical Electronic Coupling between InAs/InP Quantum-Dot Layers Emitting in the Near-Infrared Range. *Appl. Phys. Lett.*, 86:111905, 2005.

[124] K. Takemoto, Y. Sakuma, S. Hirose, T. Usuki, and N. Yokoyama. Observation of Exciton Transition in 1.3-1.55μm Band from Single InAs/InP Quantum Dots in Mesa Structure. *Jap. J. Appl. Phys*, 43(3A):L349, 2004.

[125] K. Takemoto, Y. Sakuma, S. Hirose, T. Usuki, N. Yokoyama, T. Miyazawa, M. Takatsu, and Y. Arakawa. Single InAs/InP Quantum Dot Spectroscopy in 1.3-1.55μm Telecommunication Band. *Physica E*, 26:185, 2005.

[126] H.Z. Song, T. Usuki, S. Hirose, K. Takemoto, Y. Nakata, N. Ykoyama, and Y. Sakuma. Site-Controlled Photoluminescence at Telecommunication Wavelength from InAs/InP Quantum Dots. *Appl. Phys. Lett.*, 86:113118, 2005.

[127] T. Miyazawa, K. Takemoto, Y. Sakuma, S. Hirose, T. Usuki, N. Yokoyama, M. Takatsu, and Y. Arakawa. Single-Photon Generation in the 1.55-μm Optical-Fiber Band from and InAs/InP Quantum Dot. *Jpn. J. Appl. Phys.*, 44(20):L620, 2005.

[128] Y. Sakuma, K. Takemoto, S. Hirose, T. Usuki, and N. Yokoyama. Controlling Emission Wavelength from InAs Self-Assembled Quantum Dots on InP(001)during MOCVD. *Physica E*, 26:81, 2005.

[129] Y. Akanuma, I. Yamakawa, Y. Sakum, T.Usuki, and A. Nakamura. Scanning Tunneling Microscopy Study of Interfacial Structure of InAs Quantum Dots on InP(001) Grown by Double-Cap Method. *Appl. Phys. Lett.*, 90:093112, 2007.

[130] G. Saint-Girons, N. Chauvin, A. Michlon, G. Patriarche, G. Beaudoin, G. Brémond, C. Bru-Chevalier, and I. Sagnes. Microphotoluminescence of exciton and biexciton around 1.5 μm from a single InAs/InP Quantum Dot. *Appl. Phys. Lett.*, 88:133101, 2006.

[131] K. Smaali, M. Troyon, A. El Hdiy, M. Molinari, G. Saint-Girons, and G. Patriarche. Imaging the Electric Properties of InAs/InP(001) Quantum Dots capped with a Thin InP Layer by Conductive Atomic Force Microscopy: Evidence of Memory Effect. *Appl. Phys. Lett.*, 89:112115, 2006.

[132] J.H. Teng, J.R. Dong, L.F. Chong, S.J. Chua, Y.J. Wang, and A. Chen. One-dimensional Aligned InAs/InP Quantum Dots Chain Growth by Metalorganic Vapor Phase Epitaxy for 1.55 μmm Applications. *J. Cryst. Growth*, 305:45, 2007.

[133] O. Bierwagen and W.T. Masselink. Self-Organized Growth of InAs Quantum Wires and Dots on InP(001): The Role of Vicinal Substrates. *Appl. Phys. Lett.*, 86:113110, 2005.

[134] 0. Kayser. Selective growth of InP/GaInAs in LP-MOVPE and MOMBE/CBE. *J. Cryst. Growth*, 107:989, 1991.

[135] P. Finnie, M. Buchanan, C. Lacelle, and A.P. Roth. Growth of Quantum Wire Structures by Selective Area Chemical Beam Epitaxy. *J. Cryst. Growth*, 160:220, 1996.

[136] D. Bimberg and M. Grundmann and N.N. Ledentsov. *Quantum Dot Heterostructures.* Wiley and Sons, New York, 1999.

[137] P. Hawrylak. Excitonic artificial atoms: Engineering optical properties of quantum dots. *Phys. Rev. Lett.*, 60:5597, 1999.

[138] L. Jacak, P. Hawrylak, and A. Wòjs. *Quantum Dots.* Springer, Berlin, 1998.

[139] J.J. Sakurai. *Quantum Mechanics.* Addison-Wesley, 1994.

[140] K. Brunner and U. Bockelmann and G. Abstreiter and M. Walther and G. Böhm and G. Tränkle and G. Weimann. Photoluminescence from a Single GaAs/AlGaAs Quantum Dot. *Phys. Rev. Lett.*, 69(22):3216, 1992.

[141] J.-Y. Marzin, J.-M. Gérard, A. Izraël, D. Barrier, and G. Bastard. Photoluminescence of Single InAs Quantum Dots by Self Organized Growth on GaAs. *Phys. Rev. Lett.*, 73(5):716, 1994.

[142] P.M. Petroff, P. Hawrylak, M. Korkusiński, M. Bayer, G. Macher, H. Scweizer, M. Jetter, F. Scholz, P. Borri, W. Langbein, J.-M. Gérard, and P. Michler. *Single Quantum Dots.* Topics in Applied Physics. Springer, New York, 2003.

[143] A. Badolato, K. Henessy, M. Atatüre J. Dreiser, E. Hu, P.M. Petroff, and A. Imamoğlu. Deterministic Coupling of Single Quantum Dots to Single Nanocavity Modes. *Science*, 308:1158, 2005.

[144] K. Henessy, A. Badolato, M. Winger, D. Gerace, M. Atatüre, S. Gulde, S. Fält, E.L. Hu, and A. Imamoğlu. Quantum Nature of a Strongly Coupled Single Quantum Dot-Cavity System. *Nature*, 445:896, 2007.

[145] X. Xu, I. Toft, R.T. Philips, J. Mar, K. Hammamura, and D.A. Williams. "Plug and Pay" Single Photon Sources. *Appl. Phys. Lett.*, 90:061103, 2007.

[146] D. Chitrani, R.L. Williams, J. Lefebvre, P.J. Poole, and G.C. Aers. Optical Spectroscopy of Single , Site-Selected, InAs/InP Self-Assembled Quantum Dots. *Appl. Phys. Lett.*, 84(6):978, 2004.

[147] D. Chitriani, M. Korkusinski, S.-J. Cheng, P Hawrylak, R.L. Williams, J. Lefebvre, P.J. Poole, and G.C. Aers. Electronic Structure of the P-Shell in Single, Site-Selected InAs/InP Quantum Dots. *Physica E*, 26:322, 2005.

[148] D. Kim, J. Lefebvre, J. McKee, S. Studenikin, R.L. Williams, A. Sachrajda, P. Zawadski, P. Hawrylak, W. Sheng, G.C. Aers, and P.J. Poole. Photoluminescence of Single, Site-Selected, InAs/InP Quantum Dots in High Magnetic Fields. *Appl. Phys. Lett.*, 87:212105, 2005.

[149] Gert Schedelbeck, Werner Wegscheider, Max Bichler, and Gerhard Abstreiter. Coupled Quantum Dots Fabricated by Cleaved Edge Overgrowth: From Artificial Atoms to Molecules. *Science*, 278:1792.

[150] C.X. Cui, Y.H. Chen, C. Zhao, P. Jin, G.X. Shi, Y.L. Wang, B. Xu, and Z.G. Wang. Cleaved-Edge Overgrowth of Aligned InAs Islands on GaAs. *Nanotech.*, 16:2661, 2005.

[151] D. Schuh, J. Bauer, E. Uccelli, R. Schulz, A. Kress, F. Hofbauer, J.J. Finley, and G. Abstreiter. Controlled positioning of self-assembled InAs quantum dots on (110) GaAs. *Physica E*, 26:72, 2005.

[152] V. Zwiller, T. Aichele, F. Hatami, W.T. Masselink, and O. Benson. Growth of Single Quantum Dots of Preprocessed Structures: Single Photon Emitters on a Tip. *Appl. Phys. Lett.*, 86:091911, 2005.

[153] T.-P. Hsieh, J.-I. Chyi, H.-S. Chang, W.-Y. Chen, T.M. Hsu, and W.-H. Chang. Single Photon Emission from an InGaAs Quantum Dot Precisely Positioned an a Nanoplane. *Appl. Phys. Lett.*, 90:0703105, 2007.

[154] P.S. Wong, G. Balakrishnan, N. Nuntawong, J. Tatebayashi, and D.L. Huffaker. Controlled InAs Quantum Dot Nucleation on Faceted Nanopatterned Pyramids. *Appl. Phys. Lett.*, 90:183103, 2007.

[155] J.M. Gérard and B. Gayral. Strong Purcell Effect for InAs Quantum Boxes in Three-Dimensional Solid-State Microcavities. *J. Light. Techno.*, 17(11):2089, 1999.

[156] P. Grangier, G. Reymond, and N. Schlosser. Implementations of Quantum Computing Using Cavity Quantum Electrodynamics Schemes. *Fortschr. Phys.*, 48(9-11):859, 2000.

[157] S. Haroche. *Fundamentals Systems in Quantum Optics*, volume Session LII of *Les Houches*, chapter 13:Cavity Quantum Electrodynamics, pages 767–940. Elsevier, 1990.

[158] L.C. Andreani and G. Panzarini. Strong-Coupling Regime for Quantum Boxes in Pillar Microcavities: Theory. *Phys. Rev. B*, 60(19):13276, 1999.

[159] H.J. Carmichael, R.J. Brecha, M.G. Raizen, H.J. Kimble, and P.R. Rice. Subnatural Linewidth Averaging for Coupled Atomic and Cavity-Mode Oscillators. *Phys. Rev. A*, 30(10):5516, 1989.

[160] M. Potemski and R.L. Williams. Single exciton dipole moment calculations for InAs/InP quantum dots. Private Communications.

[161] A. Thränhardt, C. Ell, G. Khitrova, and H.M. Gibbs. Relation between dipole moment and radiative lifetime in interface fluctuation quantum dots. *Phys. Rev. B*, 65:035327, 2002.

[162] D. Dalacu, R.L. Williams, D. Poitras, J. Lefebvre, P.J. Poole, and G.C. Aers. InAs/InP Quantum Dot Microcavities Employing Dielectric Bragg Mirrors. In *11th ICMSS*, 2003.

[163] D. Dalacu, D. Poitras, J. Lefebvre, P.J. Poole, G.C. Aers, and R.L. Williams. InAs/InP Quantum Dots in SiO_2/Ta_2O_5-based Microcavities. *Appl. Phys. Lett.*, 82(26):4803, 2003.

[164] D. Dalacu, D. Poitras, J. Lefebvre, P.J. Poole, G.C. Aers, and R.L. Williams. InAs/InP Quantum-Dot Pillar Microcavities using SiO_2/Ta_2O_5 Bragg Reflectors with Emission Around 1.55μm. *Appl. Phys. Lett.*, 84(17):3235, 2004.

[165] A. Yariv and P.i Yeh. *Photonics: Optical Electronics in Modern Communications* . Oxford University Press,, 2006.

[166] E. Yablonovitch. Inhibited Spontaneous Emission in Solid State Physics and Electronics. *Phys. Rev. Lett.*, 58(20):2059, 1987.

[167] S. John. Strong Localization of Photons in Certain Disordered Superlattices. *Phys. Rev. Lett.*, 58:2486, 1987.

[168] J.S. Foresi, P.R. Villeneuve, J. Ferrera, E.R. Thoen, G. Stienmeyer, S. Fan, J.D. Jannopoulos, L.C. Kimerling, H.I. Smith, and E.P. Ippen. Photonic-bandgap Microcavities in Optical Waveguides. *Nature*, 390:143, 1997.

[169] M. Okano, A. Chutinan, and S. Noda. Analysis and Design of Single-Defect Cavities in a Three-Dimensional Photonic Crystal. *Phys. Rev. B*, 66:165211, 2002.

[170] A. Balestrini, L.C. Andreani, and M. Agio. Optical Properties and Diffraction Effects in Opal Photonic Crystals. *Phys. Rev. E*, 74:036603, 2006.

[171] X. Checoury, S. Enoch, C. L'opez, and A. Blanco. Stacking Pattern in Self-Assembly Opal Photonic Crystals. *Appl. Phys. Lett.*, 90:161131, 2007.

[172] S.G. Johnson and J.D. Joannopoulos. *Photonic Crystals: The Road from Theory to Practice.* Spinger, 2002.

[173] J.D. Joannopoulos, R. D. Meade, and J.N. Winn. *Photonic Crystals: Modeling the Flow of Light.* Princeton University Press, 1995.

[174] A.R. Cowan, P. Paddon, V. Pacradouni, and J.F. Young. Resonant Scattering and Mode Coupling in Two-Dimensional Textured Planar Waveguides. *J. Opt. Soc. Am. A*, 18:1160, 2001.

[175] D.M. Whittaker and I.S. Culshaw. Scattering-Matrix Treatment of Patterned Multilayer Photonic Structures. *Phys. Rev. B*, 60(4):2610, 1999.

[176] MIT Photonic Bands code. *http : //ab − initio.mit.edu/wiki/index.php/MIT_Photonic_Bands*, 2007.

[177] K.S. Yee. Numerical Solution of Initial Boundary Value Problems Involving Maxwell's Equations in Isotropic Media. *Antennas and Propagation, IEEE Transactions on*, 14:302, 1966.

[178] A. Taflove. Application of the Finite-Difference Time-Domain Method to Sinusoidal Steady State Electromagnetic Penetration Problems. *Electromagnetic Compatibility, IEEE Transactions on*, 22:191, 1980.

[179] LumericalSolutionsInc. Vancouver, B.C. Canada. www.lumerical.com, 2005.

[180] A. Kress, F. Hofbauer, N. Reinelt, H.J. Krenner, R. Meyer, G. Böhm, and J.J. Finley. Manipulation of the Spontaneous Emission Dynamics of Quantum Dots in Two-Dimensional Photonic Crystals. *Phys. Rev. B*, 71:241304(R), 2005.

[181] E. Yablonovitch, T. Gmitter, R. Meade, A. Rappe, K. Brommer, and J. Joannopoulos. Donor and Acceptor Modes in Photonic Band Structures. *Phys. Rev. Lett.*, 67(24):3380, 1991.

[182] K. Nozaki and T. Baba. Laser Characteristics with Ultimate-Small Modal Volume in Photonic Crystal Slab Point-Shift NanoLasers. *Appl. Phys. Lett.*, 88:211101, 2006.

[183] S. Hughes and H. Kamada. Single-Quantum Dot Strong Coupling in a Semiconductor Photonic Crystal Nanocavity Side Coupled to a Waveguide. *Phys. Rev. B*, 70:195313, 2004.

[184] S. Hughes. Enhanced Single-Photon Emission from Quantum Dots in Photonic Crystal Waveguides and Nanocavities. *Opt. Lett.*, 29:2659, 2004.

[185] S. Hughes. Quantum Emission Dynamics from a Single Quantum Dot in a Planar Photonic Crystal Nanocavity. *Opt. Lett.*, 30:1393, 2005.

[186] V.S.C. Manga Rao and S. Hughes. Single Quantum-Dot Purcell Factor and β Factor in a Photonic Crystal Waveguide. *Phys. Rev. B*, 75:205437, 2007.

[187] S. Hughes. Coupled-Cavity QED Using Planar Photonic Crystals. *Phys. Rev. Lett.*, 98:083603, 2007.

[188] D. Englund, I. Fushman, and J. Vučkovic. General Recipe for Designing Photonic Crystal Cavities. *Opt. Express*, 13(16):5961, 2005.

[189] C. Sauvan, P. Lalanne, and J.P. Hugonin. Slow-Wave Effect and Mode-Profile Matching in Photonic Crystal Microcavities. *Phys. Rev. B*, 71:165118, 2005.

[190] N. Louvion, D. Gérard, J. Mouette, F. De Fornel, C. Seassal, X. Letartre, A. Rahmani, and S. Callard. Local Observation and Spectroscopy of Optical Modes in an Active Photonic-Crystal Microcavity. *Phys. Rev. Lett.*, 94:113907, 2005.

[191] N. Louvion, A. Rahmani, C. Seassal, S. Callard, D. Gérard, and F. de Fornel. Near-Field Observation of Subwavelength Confinement of Photoluminescence by a Photonic Crystal Microcavity. *Opt. Lett.*, 31:2160, 2006.

[192] J.M. Gérard, D. Barrier, J.Y. Marzin, R. Kuszelewicz, L. Manin, E. Costard, and T. Riviera. Quantum Boxes as Active Probes for Photonic Microstructures: The Pillar Microcavity Case. *Appl. Phys. Lett.*, 69(4):449, 1996.

[193] M.W. McCutcheon, G.W. Rieger, I.W. Cheung J.F. Young, D. Dalacu, S. Frédérick, A. Bodganov, P.J. Poole, G.C. Aers, and R.L. Williams. Resonant Scattering and Second Harmonic Generation Spectroscopy of a Photonic Crystal Microcavity. *Appl. Phys. Lett.*, 87:221110, 2005.

[194] M.W. McCutcheon, J.F. Young, G.W. Rieger, D. Dalacu, S. Frédérick, P.J. Poole, G.C. Aers, and R.L. Williams. Second-Order Nonlinear Mixing of Two mOdes in a Planar Photonic Crystal Microcavity. In A. Abidi, Shown-Yu Lin, and A. Sherer, editors, *Photonic Crystal Materials and Devices IV*, volume 6128 of *Proc. of SPIE*, page 612812, 2006.

[195] K.Srinivasan, P.E. Barclay, M. Borselli, and O. Painter. Optical-Fiber-Based Measurement of an Ultrasmall Volume High-Q Photonic Crystal Microcavity. *Phys. Rev. B*, 70:081306(R), 2004.

[196] K. Srinivasan, P.E. Barclay, M. Borselli, and O.J Painter. An Optical-Fiber-Based Probe for Photonic Crystal Microcavities. *IEEE J. Select. Areas in Comm.*, 23:1321, 2006.

[197] K. Srinivasan and O. Painter. Mode coupling and cavity-quantum-dot interactions in a fiber-coupled microdisk cavity. *Phys. Rev. A*, 75:023814, 2007.

[198] J.C Knight, G. Cheung, F. Jacques, and T.A. Birks. Phase-Matched Excitation of Whispering-Gallery-Mode Resonances by a Fiber Taper. *Opt. Lett.*, 22:1129, 1997.

[199] Y. Akahane, T. Asano, B.-S. Song, and S. Noda. Fine-Tuned High-Q Photonic-Crystal Nanocavity. *Opt. Express*, 13:1202, 2005.

[200] C. Grillet, C. Smith, D. Moss, B. Eggleton, S. Frédérick, D. Dalacu, P.J. Poole, J. Lapointe, G.C. Aers, and R.L. Williams. Coupling via Tapered Nanowire Micro-Loops to Photonic Crystal Nanocavities for Single-Photon Source Applications. *Opt. Express*, 15:1267, 2007.

[201] I.-K. Hwang, G.-H. Kim, and Y.-H Lee. Optimization of Coupling Between Photonic Crystal Resonator and Curved Microfiber. *IEEE J. Quant. Elect.*, 42:131, 2006.

[202] C. Manolatou, M.J. Khan, S. Fan, P.R. Villeneuve, H.A. Haus, and J.D. Joannopoulos. Coupling of Modes Analysis of resonant Channel Add-Drop Filters. *J. Quantum Electronics (IEEE)*, 35:9, 1999.

[203] K. Srinivasan, A. Stintiz, S. Krishna, and O Painter. Photoluminescence Measurements of Quantum-Dot-Containing Semiconductor Microdisk Resonators using Fiber Taper Waveguides. *Phys. Rev. B*, 72:205318, 2005.

[204] M.W. McCutcheon. *Unknown Title.* PhD thesis, University of British Columbia, 2007.

[205] M. Asada, Y. Miyamoto, and Y. Suematsu. Gain and the Threshold of Three-Dimensional Quantum-Box Lasers. *IEEE. Jour. Quant. Elect.*, 22(9):1915, 1986.

[206] Y. Arakawa and H. Sakaki. Multidimensional Quantum Well Laser and Temperature Dependence of its Threshold Current. *Appl. Phys. Lett.*, 40(11):939, 1982.

[207] N.N. Ledentsov. Quantum Dot Lasers: the Birth and Future Trends. *Semiconductors*, 33:9, 1999.

[208] G.S. Solomon, M. Pelton, and Y. Yamamoto. Single-Mode Spontaneous Emission from a Single Quantum Dot in a Three-Dimensional Microcavity. *Phys. Rev. Lett.*, 86(17):3903, 2001.

[209] E. Moreau, I. Robert, J.M. Gérard, I. Abram, L. Manin, and V. Thierry-Mieg. Single-Mode Solid-State Single Photon Source Based on Isolated Quantum Dots in Pillar Microcavities. *Appl. Phys. Lett.*, 79(18):2865, 2001.

[210] J.P. Reithmaier, G. Sęk, A. Loöffler, C. Hofmand, S. Kuhn, S. Reitsenstein, L.V. Keldysh, V.D. Kulakovskii, T.L. Reinecke, and S. Forchel. Strong Coupling in a Single Quantum Dot-Semiconductor Microcavity System. *Nature*, 432:197, 2004.

[211] D. Press, S. Gözinger, S. Reitzenstein, C. Hofman, A. Löffler, M. Kamp, A. Forchel, and Y. Yamamoto. Photon Antibunching form a Single Quantum-Dot-Microcavity System in the Strong Coupling Regime. *Phys. Rev. Lett.*, 98:117402, 2007.

[212] A. Muller, C.K. Shih, J. Ahn, D. Lu, D. Gazula, and D.G. Deppe. High Q (33 000) All-Epitaxial Microcavity for Quantum Dot Vertical-Cavity Surface-Emitting Lasers and Quantum Light Sources. *Appl. Phys. Lett.*, 88:031107, 2006.

[213] A.J. Bennett, D.J.P. Ellis, A.J. Shields, P. Atkinson, I. Farrer, and D.A. Ritchie. Observation of the Purcell Effect in High-Index-Contrast Micropillars. *Appl. Phys. Lett.*, 90:191911, 2007.

[214] D.M. Whittaker, P.S.S. Guiramaes, D. Sanvitto, H. Vinck, S. Lam, A. Daraei, Y.-L.D. Ho, J.g. Rarity, M. Hopkinson, and A. Tahraoui. High Q Modes in Elliptical Microcavity Pillars. *Appl. Phys. Lett.*, 90:161105, 2007.

[215] S. Reitzenstein, C. Hofmann, A. Gorbunov, M. Strauß, S.H. Kwon, C. Schneider, A. Löffler, S. Höfling, M. Kamp, and A. Forchel. AlAs/GaAs Micropillar cavities with Quality Factors Exceeding 150 000. *Appl. Phys. Lett.*, 90:251109, 2007.

[216] S. Frédérick, D. Dalacu, D. Poitras, G.C Aers, P.J. Poole, J. Lefbvre, D. Chitriani, and R.L. Williams. Near-infrared Single Photon Sources Employing Site-Selected InAs/InP Quantum Dots Microcavities. *Microelect. Jour.*, 36:197, 2005.

[217] H. Lohmeyer, J. Kalden, K. Sebald, C. Kruse adn D. Hommel, and J. Gutowski. Fine Tuning of Quantum-Dot Pillar Microcavities by Focused Ion Beam Miling. *Appl. Phys. Lett.*, 92:011116, 2008.

[218] C.J.M. Smith, H. Benistry, D. LAbillov, U. Oesterle, R. Houdré, T.F. Krauss, R.M. DeLaRue, and C. Weisbuch. Near-Infrared Microcavities Confined by Two-Dimensional Photonic Bandgap Crystal. *Elect. Lett.*, 35(3):228, 1999.

[219] D. Dalacu, S. Frédérick, A. Bodganov, P.J. Poole, G.C. Aers, R.L. Williams, M.W. McCutcheon, and J.F. Young. Fabrication and Optical Characterization of Hexagonal Photonic Crystal Microcavities in InAs/InP Quantum Dot Membranes. *J. Applied Phys.*, 98:023101, 2005.

[220] D. Dalacu, S. Frédérick, P.J. Poole, G.C. Aers, and R.L. Williams. Post-Fabrication Fine-Tuning of Photonic Crystal Microcavities in InAs/InP Quantum Dot Membranes. *Appl. Phys. Lett.*, 87:151107, 2005.

[221] D. Dalacu, S. Frederick, J. Lapointe, P.J. Poole, G.C. Aers, and R.L. Williams. Modified Single Missing Air-Hole Defects in InAs/InP Quantum Dot Membrane Photonic Crystal Microcavities. *J. Vac. Scie. and Technol. A*, 24(3):791, 2006.

[222] S. Frédérick, D. Dalacu, G.C. Aers, P.J. Poole, J. Lapointe, and R.L. Williams. Optical Characterisation of InAs/InP Quantum Dot Photonic Cavity Membranes. *Physica E*, 32:504, 2006.

[223] S. Frédérick, D. Dalacu, J. Lapointe, P.J. Poole, G.C. Aers, and R.L. Williams. Experimental Demonstration of High Quality Factor, x-Dipole Modes in InAs/InP Quantum Dot Photonic Crystal Microcavity Membranes. *Appl. Phys. Lett.*, 89:091115, 2006.

[224] S. Frédérick, D. Dalacu, P.J. Poole, J. Lapointe, G.C. Aers, and R.L. Williams. InAs/InP Quantum Dot Photonic Crystal Microcavities. *Phys. Stat. Solidi c*, 3:3685, 2006.

[225] W.-H. Chang, W.-Y. Chen, H.-S. Chang, T.-P. Hsieh, J.-I. Chyi, and T.M. Hsu. Efficient Single-Photon Based on Low-Density Quantum Dots in Photonic-Crystal Nanocavities. *Phys. Rev. Lett.*, 96:117401, 2006.

[226] P. Andrew and W.L. Barnes. Energy Transfer Across a Metal Film Mediated by Surface Plasmon Polaritions. *Science*, 306:1002, 2004.

[227] Z. Zhang and M. Qiu. Small-Volume waveguide-Section High Q Microcavities in 2D Photonic Crystal Slabs. *Opt. Express*, 12(17):3988, 2004.

[228] Y. Akahane, T. Asano, B.-S. Song, and S. Noda. High-Q Photonic Nanocavity in a Two-Dimensional Photonic Crystal. *Nature*, 425:944, 2003.

[229] M. Notomi, H. Taniyama, S. Mitsugi, and W. Kuramochi. Optomechanical Wavelength and Energy Conversion in High-Q Double-Layer Cavities of Photonic Crystal Slabs. *Phys. Rev. Lett.*, 97:023903, 2006.

[230] T. Yoshie, A. Scherer, J. Hendrickson, G. Khitrova, H.M. Gibbs, G. Rupper, C. Ell, O.B. Shchekin, and D.G. Deppe. Vacuum Rabi Splitting with a Single Quantum Dot in a Photonic Crystal Nanocavity. *Nature*, 432:200, 2004.

[231] A. Khalili, H. Bae, and J.S. Harris Jr. An Evanescent-Coupling Approach to Making Stable Fiber-Coupled Semiconductor Lasers. *Appl. Phys. Lett.*, 89:041105, 2006.

[232] P. Lalanne and J.-P. Hugonin. Bloch-Wave Engineering for High-Q, Small-V Microcavities. *J. Quantum Elect.*, 39:1430, 2003.

[233] P. Lalanne, S. Mias, and J.P. Hugonin. Two Physical Mechanisms for Boosting the Quality Factor to Cavity Volume Ratio of Photonic Crystal Microcavities. *Opt. Express*, 12:458, 2004.

[234] C. Sauvan, P. Lalanne, and J.-P. Hugoin. Tuning Holes in Photonic-Crystal Nanocavities. *Nature*, 429:only online, 2004.

[235] J. Vučkovič and Y. Yamamoto. Photonic Crystal Microcavities for Cavity Quantum Electrodynamics. *Appl. Phys. Lett.*, 82(15):2374, 2003.

[236] O. Painter, R.K. Lee, A. Sherer, A. Yariv, J.D. O'Brien, P.D. Dapkus, and I. Kim. Two-Dimensional Photonic Band-Gap Defect Mode Laser. *Science*, 284:1819, 1999.

[237] M. Lončar, M. Hochberg, A. Scherer, and Y. Qiu. High Quality Factors and Room-Temperature Lasing in a Modified Single-Defect Photonic Crystal Cavity. *Opt. Lett.*, 29(7):721, 2004.

[238] D. Englund, D. Fattal, E. Waks, G. Solomon, B. Zhang, T. Nakaoka, Y. Arakawa, Y. Yamamoto, and J. Vučković. Controlling the Spontaneous Emission Rate of Single Quantum Dots in a Two-Dimensional Photonic Crystal. *Phys. Rev. Lett.*, 95:013904, 2005.

[239] E. Peter, P. Senellart, D. Martou, A. Lemaître, J. Hours, J.M. Gérard, and J. Bloch. Exciton-Photon Strong-Coupling Regime for a Single Quantum Dot Embedded in a Microcavity. *Phys. Rev. Lett.*, 95:067401, 2005.

[240] K. Hennessy, A. Badlato, A. Tamboli, P.M. Petroff, and E. Hu. Tuning Photonic Crystal Nanocavity Modes by Wet Chemical Digital Etching. *Appl. Phys. Lett.*, 87:021108, 2005.

[241] K. Hennessy, C. Högerle, E. Hu, A. Badolato, and A. Imamoğlu. Tuning Photonic Nanocavities by Atomic Force Microscope Nano-Oxydation. *Appl. Phys. Lett.*, 89:041118, 2006.

[242] A.R. Alija, L.J. Martinez, A. Garcia-Martin, M.L. Dotor, D. Golmayo, and P.A. Postigo. Tuning of Spontaneous Emission of Two-Dimensional Photonic

Crystal Microcavities by Accurate Control of Slab Thickness. *Appl. Phys. Lett.*, 86:141101, 2005.

[243] A. Faraon, D. Englund, I. Fushman, J. Vučković, N. Stoltz, and P. Petroff. Local Quantum Dot Tuning on Photonic Crystal Chip. *Appl. Phys. Lett.*, 90:213110, 2007.

[244] S. Mosor, J. Hendrickson, B.C. Richards, J. Sweet, G. Khitrova, H.M. Gibbs, T. Yoshie, A. Scherer, and O.B. Shchekin D.G. Deppe. Scanning a Photonic Crystal Slab Nanocavity by Condensation of Xenon. *Appl. Phys. Lett.*, 87:141105, 2005.

[245] C. Grillet, C. Smith, D. Freeman, S. Madden, B. Luther-Davis, E.C. Magi, D.J. Moss, and B.J. Eggleton. Efficient Coupling to Chalcogenide Glass Photonic Crystal Waveguides via Silica Optical Fiber Nanowires. *Opt. Express*, 14:1070, 2006.

[246] B. Maune, M. Lončar, J. witzens, M. Hochberg, T. Baehr-Jones, D. Psaltiss, A. Scherer, and Y. Qiu. Liquid-crystal Electric Tuning of a Photonic Crystal Laser. *Appl. Phys. Lett.*, 85:3, 2004.

[247] K. Srinivasan, M. Borselli, T.J. Johnson, P.E. Barclay, O. Painter, A. Stintz, and S. Krishna. Optical Loss and Lasing Characteristics of High-Quality-Factor AlGaAs Microdisk Resonator with Embedded Quantum Dots. *Appl. Phys. Lett.*, 86:151106, 2005.

[248] K. Srinivasan, M. Borselli, O Painter, A. Stintiz, and S. Krishna. Cavity Q, Mode Volume, and Lasing Threshold in Small Diameter AlGaAs Microsdisks with Embedded Quantum Dots. *Opt. Express*, 14:1094, 2006.

[249] M. Cai, O. Painter, and K.J. Vahala. Observation of Critical Coupling in a Fiber Taper to a Silica-Microsphere Whispering-Gallery Mode System. *Phys. Rev. Lett.*, 85:74, 2000.

[250] P.E. Barlcay, K. Srinivasan, O. Painter, B. Lev, and H. Mabuchi. Integration of Fiber-Coupled High-Q SiN_x Microdisks with Atom Chips. *Appl. Phys. Lett.*, 89:131108, 2006.

[251] C.P. Michael, M. Borselli, T. J. Johnson, C. Chrystal, and O. Painter. An Optical Fiber-Taper Probe for Wafer-Scale Microphotonic Device Characterization. *Opt. Express*, 15:4745, 2007.

[252] T. Aoki, B. Dayan, E. Wilcut, W.P. Bowen, A.S. Parkins, T.J. Kippenberg, K.J. Vahala, and H.J. Kimble. Observation of Strong-Coupling between one Atom and a Monolithic Microresonator. *Nature*, 443:671, 2006.

[253] K. Srinivasan, O. Painter, A. Stintz, and S. Krishna. Single Quantum Dot Spectroscopy using a Fiber Taper Waveguide Near-Field Optic. *http://www.arxiv.org/abs/0706.1831*, submitted, 2007.

[254] I. Märki, M. Salt, and H.-P. Herzig. Tuning the Resonance of a Photonic Crystal Microcavity with an AFM Probe. *Opt. Express*, 14:2969, 2006.

[255] J.C. Knight. Photonic Crystal Fibers. *Nature*, 424:847, 2003.